Istros 2015

1.–6. May

Isospin, Structure, Reactions and Energy of Symmetry 2015

2nd International Conference

Proceedings

of the ISTROS 2015 International Conference

SAV

SLOVENSKÁ AKADÉMIA VIED ACCADEMIA SCIENTIARUM SLOVACA

Proceedings

of the ISTROS 2015 International Conference

Častá-Papiernička, Slovakia
1–6 May 2015

Editors

M. Veselský and M. Venhart
Institute of Physics, Slovak Academy of Sciences

Sponsors

Slovak Research
and Development Agency

Slovak Physics Society

ISBN 978-80-971975-1-3
Bratislava 2017

LIST OF PARTICIPANTS

Matúš Balogh (Institute of Physics of SAS Bratislava)	matus.balogh@savba.sk
Mark Bissell (University of Manchester & CERN Geneva)	mark.bissell@cern.ch
David Boilley (GANIL Caen)	boilley@ganil.fr
Lie-Wen Chen (Jiao Tong University Shanghai)	lwchen@sjtu.edu.cn
Benjamin P. Crider (Michigan State University)	crider@nscl.msu.edu
Antonio Di Nitto (GSI Darmstadt)	a.dinitto@gsi.de
Zhaoqing Feng (IMP Lanzhou)	fengzhq@impcas.ac.cn
Liam Gaffney (UWS Paisley)	liam.gaffney@uws.ac.uk
Paul Garrett (University of Guelph)	pgarrett@physics.uoguelph.ca
Tuomas Grahn (JYFL Jyväskylä)	tuomas.grahn@jyu.fi
Rolf-Dietmar Herzberg (University of Liverpool)	R.Herzberg@Liverpool.ac.uk
Fritz Peter Heßberger (GSI Darmstadt)	f.p.hessberger@gsi.de
Igor Izosimov (JINR Dubna)	izosimov@jinr.ru
David Joss (University of Liverpool)	David.Joss@liverpool.ac.uk
Jozef Klimo (Institute of Physics of SAS Bratislava)	jozef.klimo@savba.sk
Magda Kowalska (CERN Geneva)	kowalska@cern.ch
Kara Lynch (CERN Geneva)	kara.marie.lynch@cern.ch
Yu-Gang Ma (SINAP Shanghai)	ygma@sinap.ac.cn
Miguel Madurga (CERN Geneva)	miguel.madurga@cern.ch
Vladislav Matoušek (Institute of Physics of SAS Bratislava)	Vladislav.Matousek@savba.sk
Katsuhisa Nishio (ASRC JAEA Tokai)	nishio.katsuhisa@jaea.go.jp
Emanuele V. Pagano (Università di Catania & INFN-LNS)	epagano@lns.infn.it
Janne Pakarinen (JYFL Jyväskylä)	janne.pakarinen@jyu.fi
Paul Papka (University of Stellenbosch)	papka@sun.ac.za
Erin E. Peters (University of Kentucky, Lexington)	fe.peters@uky.edu
Kristian Petrík (Institute of Physics of SAS Bratislava)	kristian.petrik@savba.sk
Paresh Prajapati (Institute of Physics of SAS Bratislava)	paresh.prajapati@savba.sk
Riccardo Raabe (KU Leuven)	raabe@kuleuven.be
Zhongzhou Ren (Nanjing University)	zren@nju.edu.cn
Anton Repko (Charles University Prague)	anton@a-repko.sk
Paolo Russotto (INFN-LNS Catania)	russotto@lns.infn.it
George A. Souliotis (University of Athens)	soulioti@chem.uoa.gr
Livius Trache (IFIN-HH Bucharest)	livius.trache@nipne.ro
Róbert Urban (Institute of Physics of SAS Bratislava)	robert.urban@savba.sk
Martin Venhart (Institute of Physics of SAS Bratislava)	mvenhart@cern.ch
Martin Veselský (Institute of Physics of SAS Bratislava)	martin.veselsky@savba.sk
Michał Warda (UMCS Lublin)	warda@kft.umcs.lublin.pl
John L. Wood (Georgia Tech, Atlanta)	jw20@prism.gatech.edu
Katarzyna Wrzosek-Lipska (University of Warsaw)	wrzosek@slcj.uw.edu.pl
Jun Xu (SINAP Shanghai)	xujun@sinap.ac.cn
Steven W. Yates (University of Kentucky)	yates@uky.edu
Feng-Shou Zhang (BNU Beijing)	fszhang@bnu.edu.cn
Magda Zielińska (CEA Saclay)	magda.zielinska@cea.fr

Contents

1 PREFACE

Dear participants,

in this electronic mini-proceedings we bring to you and also to wider public a summary of the 2nd edition of the ISTROS (Isospin, STructure, Reactions and energy Of Symmetry) conference, which took place in the period between May 1 – May 6 2015 in Častá-Papiernička. We respect the decision of a large part of you to not contribute to conference proceedings, and to avoid publishing the transparencies from your talks. Nevertheless, we still believe that some form of summary of the meeting needs to be published for historical record, and thus we bring these mini-proceedings in the present form.

In the proceedings of 1st edition of Istros conference we brought to you a "Brief summary of History of Natural Sciences and Technology in Slovakia". For these interested, it can be still found at the conference webpage. This time we bring to your attention just one curious information, related to the ever growing social impact of information technologies, which we noticed in the local and international press recently.

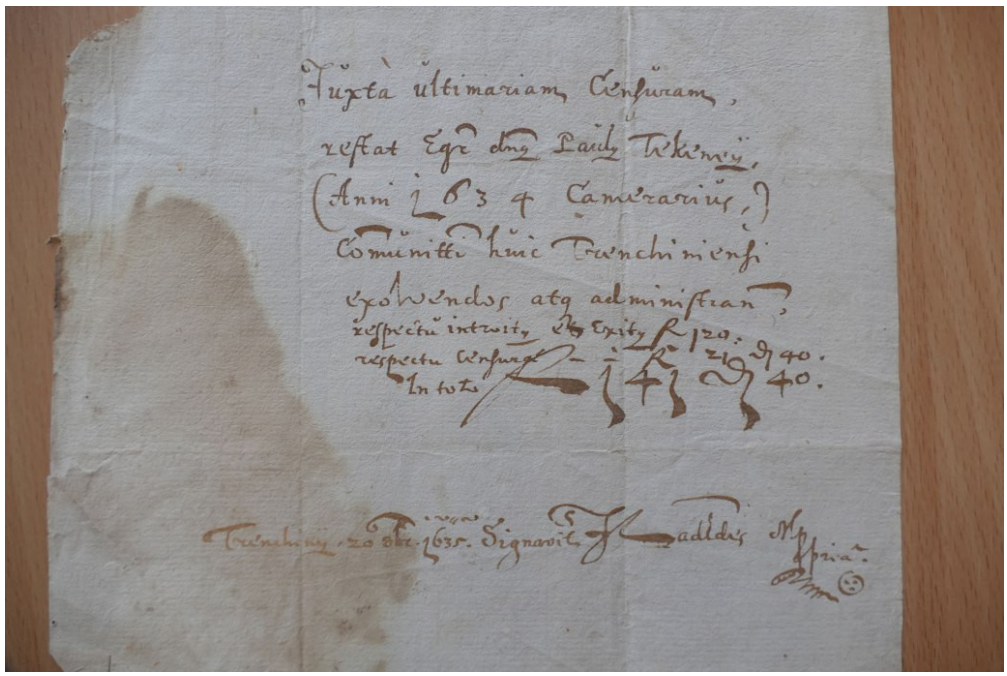

As documented in the above figure, it appears that the popular "smiley" emoji was used for the first time in the legal document from the year 1634, found in the records of the Trenčín region in western Slovakia. We hope that your memories from our conference are also associated with smiling faces and that many of you will sooner or later return for more smiles to our conference in Slovakia, a home of "smiley". We are looking forward to welcome you again and keep many smiles in store for that occasion !

Martin Veselský and Martin Venhart

Co-chairs of the Organizing Committee

2 ARTICLES

Studies of A = 76 Nuclei: States in ^{76}Se below 3 MeV

B.P. Crider[1,*], A. Chakraborty[1,2], A. Kumar[1,2], E.E. Peters[2], F.M. Prados-Estévez[1,2], T.J. Ross [1,2], M.T. McEllistrem[1], and S.W. Yates[1,2]

[1]Department of Physics and Astronomy, University of Kentucky, Lexington, KY 40506-0055, USA
[2]Department of Chemistry, University of Kentucky, Lexington, KY 40506-0055, USA

Abstract

The nuclear structure of ^{76}Se is of interest as it is a daughter of the neutrinoless double-beta decay candidate ^{76}Ge, as well as its existence in a transitional region of the nuclear chart. Excited states of ^{76}Se have been populated via inelastic neutron scattering at the University of Kentucky Accelerator Laboratory. As a result, new level information has been determined. In particular, a new excited 0^+ state is proposed below 2.0 MeV.

INTRODUCTION

Recently, ^{76}Ge and ^{76}Se have been the focus of much experimental effort. Such attention is the result of the capability of ^{76}Ge to undergo double-beta decay to ^{76}Se. In particular, the possibility of the occurrence of neutrinoless double-beta decay ($0\nu\beta\beta$) has prompted many studies with the aim of investigating the underlying structure of both of these nuclei to provide information useful for calculating the $0\nu\beta\beta$ matrix elements.

While $0\nu\beta\beta$ remains a major focus, the nuclear structure of these nuclei has received renewed attention [1, 2]. Such interest stems from the fact that these nuclei exist in a transitional region of the nuclear chart. Within a transitional region, nuclei typically have shapes somewhere between the idealized spherical ($\beta, \gamma = 0$) and quadrupole deformed ($\beta \neq 0, \gamma = 0$) configurations where axial symmetry is broken ($\gamma \neq 0$), at which point an appropriate description is in terms of a triaxial mean field. The key to the existence of a transitional region lies in the fact that both the $\beta = 0$ and $\beta \neq 0$ configurations are energetically available without a strong preference for one over the other. The differences in the features of the energy spectrum then arise based on the possible values of β. While the expectation value of β may be relatively large or small, the range of β values does much to determine whether the energy spectrum more closely resembles that of a vibrator or rotor. Exploring such transitional regions and how the shape changes across neighboring nuclei yields information about the evolution of both the magnitude and the range of the deformation.

The nature of triaxiality of the nucleus, which is commonly referred to in relation to the extremes of a completely rigid γ deformation [3] and γ-soft deformation [4], is another topic of interest. Refs. [1] and [2] support an argument that ^{76}Ge is both a rare case of rigid triaxiality and also the only nucleus with a rigid triaxial shape in this region. A road map of the evolution of triaxiality from γ soft to rigid-γ at ^{76}Ge could prove useful for testing theoretical models, however, such a map can only be useful if there is sufficient knowledge of all low-energy levels.

This work focuses on ^{76}Se, which lies within the same transitional region as ^{76}Ge. Early studies of ^{76}Se showed its collective nature when Coulomb excitation measurements of the B(E2:$2_1^+ \rightarrow 0_1^+$) exposed an enhancement of approximately 50 times the single-particle values [5, 6]. Today, this number is accepted as 44 W.u. [7]. Further inelastic deuteron scattering studies suggested apparent vibrational character [8] due to strong excitation of the 1-phonon and 2-phonon states as well as the octupole phonon.

Early ideas of structure beyond a spherical vibrator were introduced theoretically in the form of predictions of a quasirotational band [9, 10] and experimentally through $(\alpha, 2n\gamma)$ and $(\alpha, 4n\gamma)$ reactions [6], where such a quasirotational band was built based upon energies and relative intensities of the observed yrast states up to $J^\pi = 10^+$. If ^{76}Se is vibrational, the spherical vibrator model needed modification. One such effort to extend the vibrational model was to employ configuration mixing of the different phonon states [11]. Firm establishment of rotational bands occurred in the early 1980s [12, 13] and by the late 80s a triaxial rotor description of the low-lying 2^+ and 0^+ levels emerged [14]. In general, these studies attempted to classify this nucleus within the context of a single nuclear model. The emergence of shape coexistence [15] as a feature whose presence is felt in many places across the nuclear landscape, including the region near A = 76, may suggest that this nucleus can best be explained as a coexistence of multiple structures. Supplying further experimental information for such comparisons with models, as well as addressing issues with the level scheme, is a major goal of this work.

*E-mail: crider@nscl.msu.edu

EXPERIMENTAL DETAILS

The ^{76}Se(n,n$'\gamma$) experiments were performed at the University of Kentucky Accelerator Laboratory (UKAL) using the 7-MV Van de Graaff accelerator. An angular distribution measurement was performed with 3.0-MeV incident neutrons produced with the ^{3}H(p,n) reaction at 11 angles, ranging from 40° to 150°. In addition, an excitation function measurement was performed with incident neutron energies ranging from 2.0 MeV to 3.0 MeV in 100-keV steps at a detection angle of 90°. The scattering sample was 11.96 g of elemental ^{76}Se powder enriched to 96.95%, with dimensions of radius = 0.7 cm and height = 2.6 cm, placed a distance of 5.7 cm from the center of the tritium gas cell where the neutrons were produced. Each experiment was performed using approximately 120 hours of beam time. For the angular distribution measurement, a ^{24}Na source was placed near the HPGe detector such that, after β^- decay to ^{24}Mg, the 1368.626(5)-keV and 2754.007(11)-keV γ rays could be used for energy calibration. An example of the spectra obtained in this work is shown in Fig. 1.

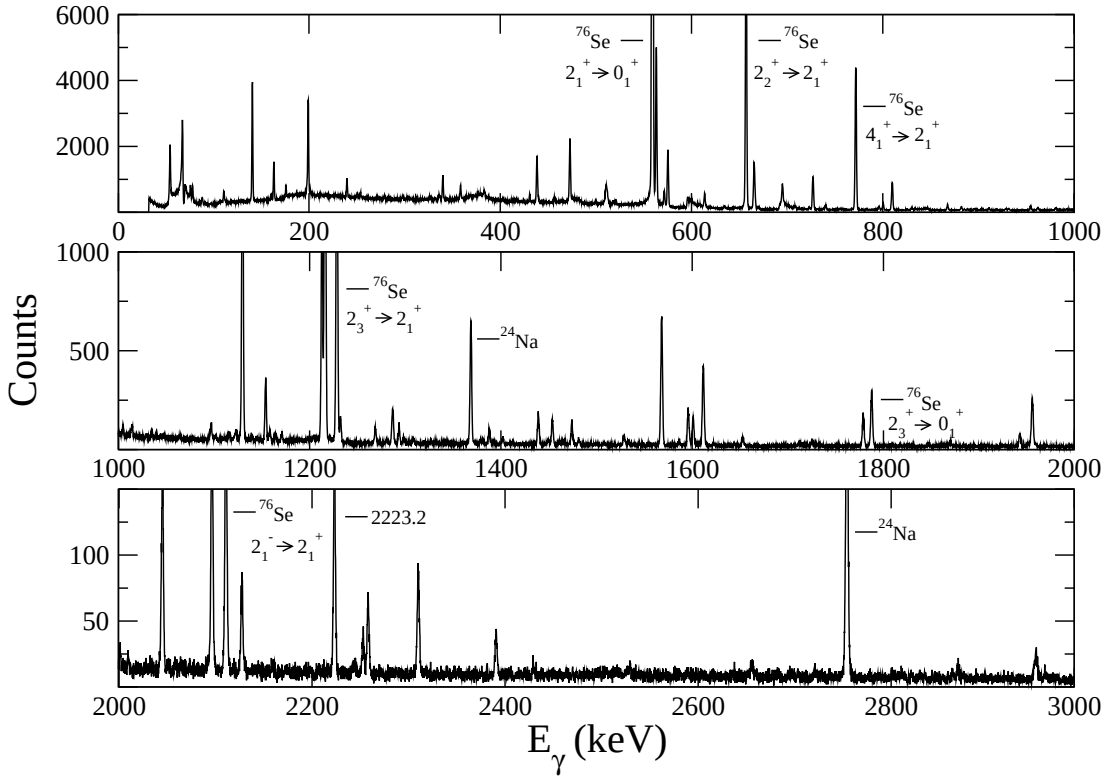

Fig. 1: γ-ray spectrum from the ^{76}Se(n,n$'\gamma$) reaction with E$_n$ = 3.0 MeV and $\theta = 90°$.

LIFETIME ANALYSIS

A level lifetime analysis of the angular distribution data was performed using the Doppler-shift attenuation method [16]. The experimental attenuation factor, $F(\tau)$, describes the slowing down of the recoiling nucleus within the target material and is obtained from:

$$E_\gamma(\theta) = E_0 \left[1 + F(\tau)\frac{v_{c.m.}}{c} cos\ \theta\right] \quad (1)$$

where $E_\gamma(\theta)$ is the γ-ray energy as a function of the angle of detection with respect to the direction of the incident neutrons, E_0 is the energy of the γ ray emitted by the nucleus at rest, $v_{c.m.}$ is the recoil velocity of the center of mass, and c is the speed of light. The method thus depends on the centroid of the γ-ray peak, allowing for relatively small uncertainties even for low statistics peaks. Figure 2 shows this change in centroid visually at three different detection angles for the 2310-keV γ ray from the 2869-keV level.

The Winterbon formalism, which describes the electronic and nuclear stopping process [17] was employed to extract the lifetime, τ, from F(τ). Figure 3 shows how τ can be extracted from the experimental F(τ)

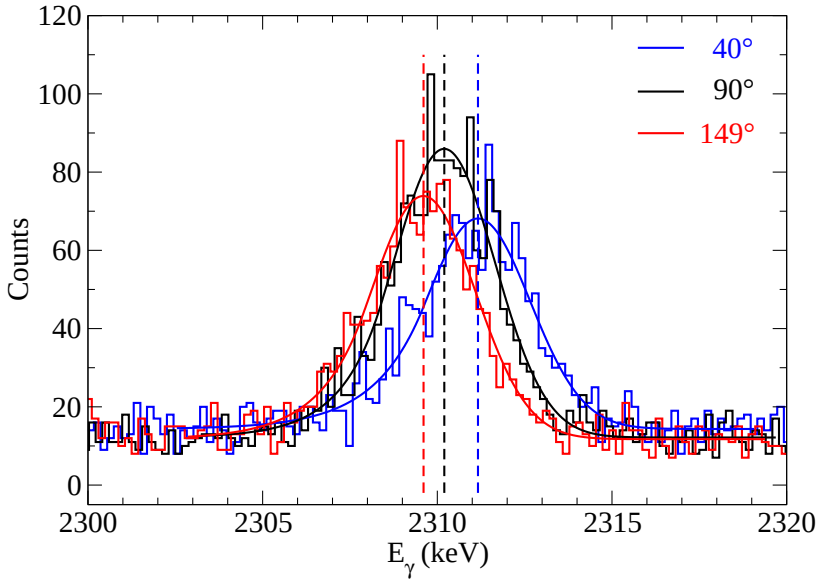

Fig. 2: Spectra exhibiting the Doppler shift in γ-ray energy.

value (top panel) and the calculated curve (bottom panel).

ANGULAR DISTRIBUTION ANALYSIS

The angular distributions of the γ rays provide information about the multipolarities of transitions. A full analysis of the angular distribution data involves fitting the normalized, experimental γ-ray yields to an expansion of even-order Legendre polynomials,

$$W(\theta) = 1 + A_2 P_2(cos\theta) + A_4 P_4(cos\theta) \quad (2)$$

where P_n are the Legendre polynomials and A_n are the coefficients of the fit. This fit can be compared to statistical model calculations, using the code CINDY, of the angular distribution coefficients for γ-ray decays to and from various spin-parity combinations. Such a comparison allows for the extraction of the multipole mixing ratio, δ, through the use of a χ^2 minimization. Examples of a fit to Eqn. 2 and the subsequent comparison to the theoretical calculations are shown in Figs. 4 and 5, respectively. Figure 5 shows that a spin assignment of J = 2 is favored, but the proximity of another minimum for a J = 3 assignment indicates that the J = 2 assignment should be regarded as tentative.

EXCITATION FUNCTION ANALYSIS

An excitation function analysis can provide information about the J^π of a level and is essentially the level population cross section as a function of the incident neutron energy. The idea is to determine the normalized γ-ray intensity (cross section) as a function of incident neutron energy. These data are then compared to calculations for each of the possible J^π options. An example of an excitation function with relative cross sections is shown in Fig. 6 for the 2171-keV level. The good agreement with the calculation for a $J^\pi = 0^+$ level led to a new spin-parity assignment of $(0)^+$ when these data are coupled with angular distribution information.

RESULTS AND CONCLUSIONS

A short discussion of a new $(0)^+$ assignment at 1791.5 MeV is useful, as a new 0^+ state below 2 MeV is of interest in almost any nucleus. In the Nuclear Data Sheets compilation [7], the existence of the level at 1791.5 keV is questionable; this work lends support for its existence. In Ref. [7], the 575.1-keV γ ray from this level to the 2_2^+ level shares a very similar energy to the 575.3-keV γ ray assigned as belonging to the

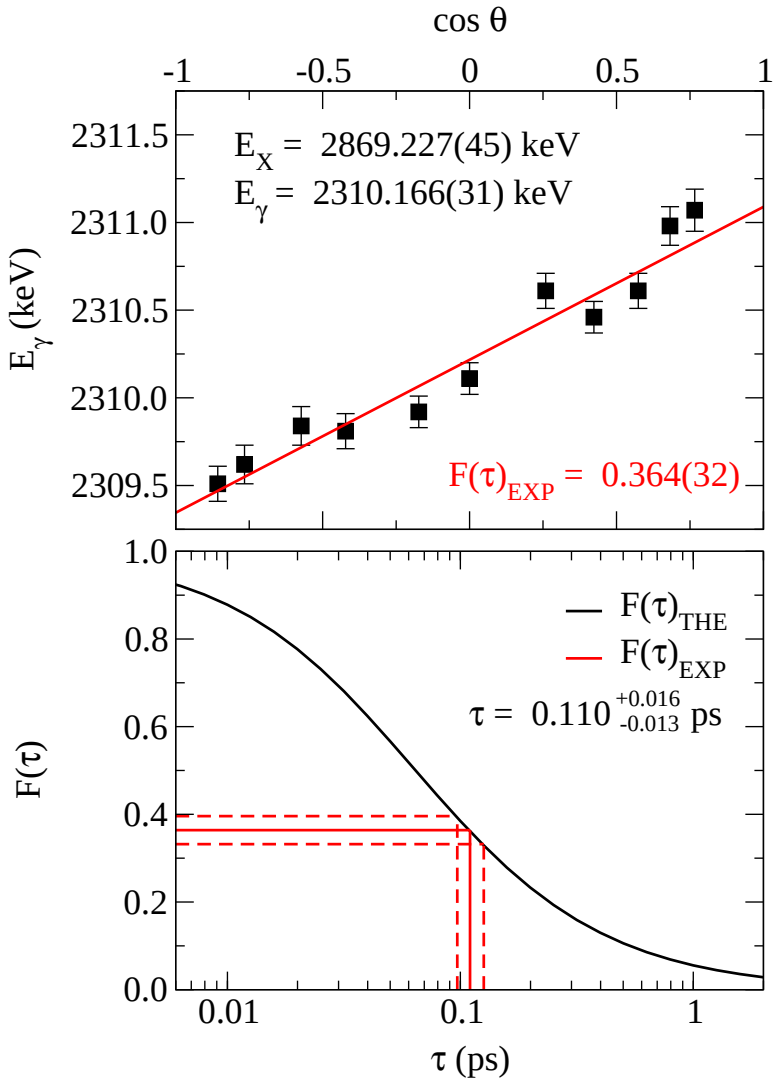

Fig. 3: Top: Determination of F(τ) from a fit of the 2310-keV γ-ray energy as a function of the cosine of the detection angle based on Eqn. 1. Bottom: Extraction of the τ value from comparison to a theoretically calculated attenuation curve based upon Ref. [17].

2363.0-keV level. Excitation function spectra clearly show a relatively intense γ ray at the initial incident neutron energy of $E_n = 2.0$ MeV and no indication of any increase in intensity at or above $E_n = 2.4$ MeV. In fact, none of the reported γ rays originating from the 2363.0-keV level were observed. For the case of the 575.3-keV γ ray, relocation of the γ ray to the 1791.5-keV level is suggested. Further support of the existence of the 1791.5-keV level was observed in the form of a newly observed γ ray with an energy of 1232.3 keV. The peak in the spectrum had a normalized area of a few hundred counts at $E_n = 2.0$ MeV, which indicates that the only state it can possibly decay to is the 559.1-keV 2_1^+ state. A tentative spin-parity assignment of $(0)^+$ was made based upon a comparison of the excitation function to statistical model calculations (`CINDY`), as well as the nearly isotropic angular distributions of both the 575.3- and 1232.3-keV γ rays.

Much new information has been added in the form of lifetimes and subsequently determined transition probabilities that will be compiled in a later publication. The new $(0)^+$ state assignment below 2 MeV could have interesting theoretical interpretations in the future, but the lack of supporting information on the transition probabilities, due to not observing a measurable lifetime in this work, makes it difficult to draw firm conclusions on its nature. Overall, the suggested modifications to the level scheme and the additional information supplied from this work should give a more comprehensive picture to theorists wishing to better understand the nature of the levels in this transitional nucleus.

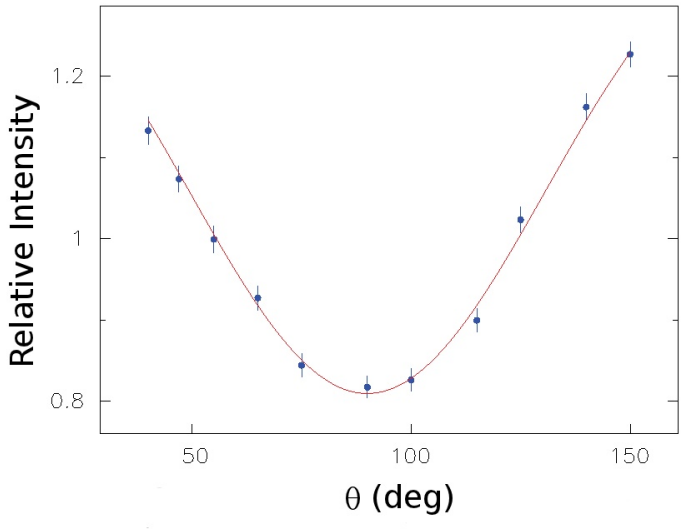

Fig. 4: Angular distribution of the 727-keV γ ray from the 2515-keV (2^+) level. The fitted coefficients are $A_2 = 0.367(16)$ and $A_4 = -0.019(21)$.

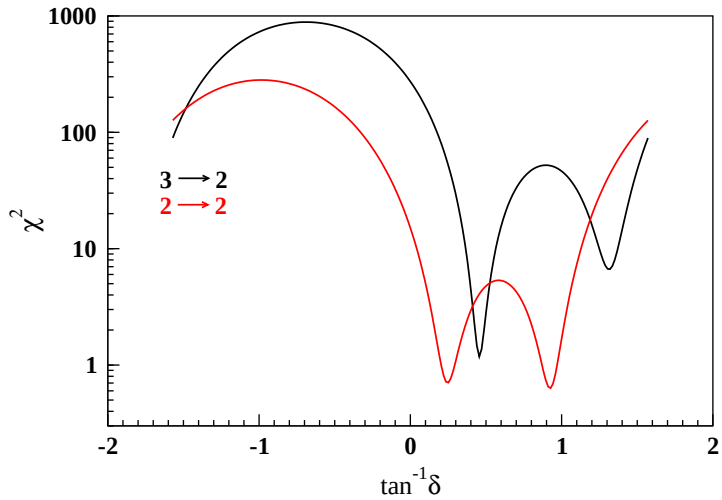

Fig. 5: A χ^2 minimization comparing the experimental angular distribution to combinations of the calculated `CINDY` curves is used to find the multipole mixing ratio, δ. The minima correspond to the best values for δ.

ACKNOWLEDGMENT:
The authors gratefully acknowledge the assistance of H.E. Baber in maintaining the University of Kentucky Accelerator. This material is based upon work supported by the U.S. National Science Foundation under Grant No. PHY-1305801.

REFERENCES

[1] Y. Toh, C.J. Chiara, E.A. McCutchan, W.B. Walters, R.V.F. Janssens, M.P. Carpenter, S. Zhu, R. Broda, B. Fornal, B.P. Kay, F.G. Kondev, W. Królas, T. Lauritsen, C.J. Lister, T. Pawłat, D. Seweryniak, I. Stefanescu, N.J. Stone, J. Wrzesiński, K. Higashiyama, and N. Yoshinaga, Phys. Rev. C **87**, 041304 (2013).
[2] G.H. Bhat, W.A. Dar, and J.A. Sheikh, Phys. Rev. C **89**, 014328 (2014).
[3] A.S. Davydov and G.F. Filippov, Nucl. Phys. **8**, 237 (1958).

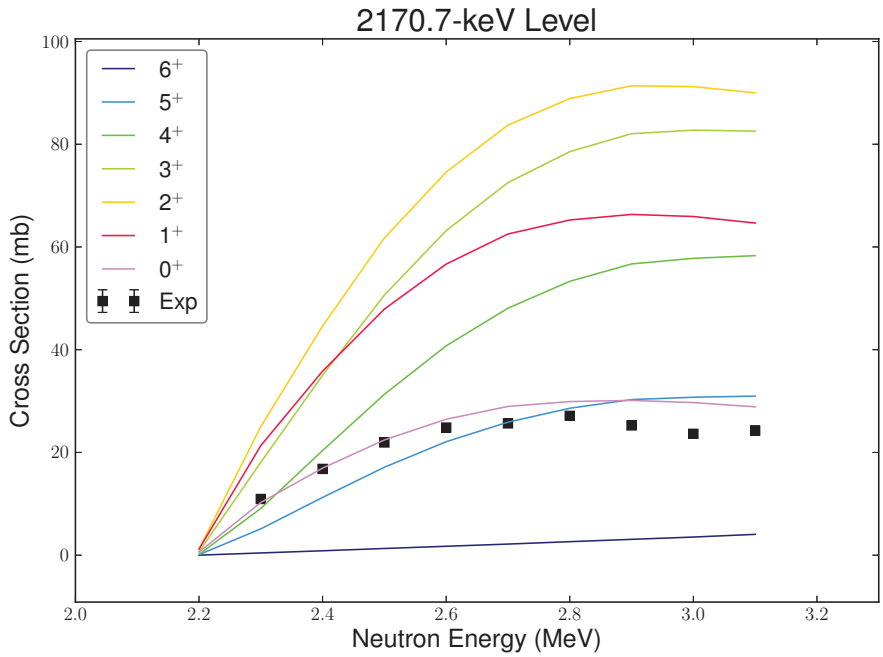

Fig. 6: Excitation function of the 2171-keV level and comparisons to theoretical calculations. This information, in addition to the angular distribution measurement, led to a new spin-parity assignment of $(0)^+$.

[4] L. Wilets and M. Jean, Phys. Rev. **102**, 788 (1956).
[5] P.H. Stelson and F.K. McGowan, Nuclear Physics **32**, 652 (1962).
[6] R.M. Lieder and J.E. Draper, Phys. Rev. C **2**, 531 (1970).
[7] B. Singh, Nuclear Data Sheets **74**, 63 (1995).
[8] E.K. Lin, Nucl. Phys. **73**, 613 (1965).
[9] R.M. Diamond, F.S. Stephens, and W.J. Swiatecki, Physics Letters **11** 315 (1964).
[10] M.A.J. Mariscotti, G. Scharff-Goldhaber, and B. Buck, Phys. Rev. **178** 1864 (1969).
[11] R. Singh, G.K. Mehta, and Y.R. Waghmare, Physics Letters B **45** 199 (1973).
[12] J.C. Wells, R.L. Robinson, H.J. Kim, R.O. Sayer, R.B. Piercey, A.V. Ramayya, J.H. Hamilton, C.F. Maguire, Phys. Rev. C **22**, 1126 (1980).
[13] T. Matsuzaki and H. Taketani, Nucl. Phys. A **390**, 413 (1982)
[14] F. Ballester, E. Casal, J.B.A. England, and F. Moriano, J. Phys. G: Nucl. Phys. **14**, 1103 (1988).
[15] K. Heyde and J.L. Wood, Rev. Mod. Phys. **83** 1467 (2011).
[16] T. Belgya, G. Molnár, and S.W. Yates, Nucl. Phys. **A607**, 43 (1996).
[17] K.B. Winterbon, Nucl. Phys. **A246**, 293 (1975).

Experiments on Production and Nuclear Structure Investigation of Superheavy Elements at GSI

Fritz Peter Heßberger[1,2*]

[1]GSI - Helmholtzzentrum für Schwerionenforschung GmbH, Planckstraße 1, 64291 Darmstadt, Germany
[2] Helmholtzinstitut Mainz, Johann-Joachim-Becherweg 45, 55128 Mainz, Germany

Abstract

An extensive program on synthesis of superheavy elements (SHE) and investigation of their nuclear structure and chemical properties has been performed at the UNILAC accelerator at GSI Helmholtzzentrum für Schwerionenforschung GmbH, Darmstadt, during the past three and a half decades. In recent years the program was focussed on attempts to synthesize the so far unknown elements 119 and 120 using the reactions ^{249}Bk(^{50}Ti,xn)$^{299-x}$119, ^{249}Cf(^{50}Ti,xn)$^{299-x}$120, and ^{248}Cm(^{54}Cr,xn)$^{302-x}$120. No decay chains that could be attributed to isotopes of these elements were observed; only upper production cross section limits were estimated.
Nuclear structure investigation concentrated on systematics of single particle levels in odd-mass nuclei, studies of two- and four-quasi-particle states forming K-isomers and attempts to unambiguously determine the atomic number of isotopes of SHE by measuring coincidences between α - particles and K X-rays. In recent experiments at the velocity filter SHIP α decay -, electron capture (EC) - and spontaneous fission (SF) properties of ^{258}Db and ^{255,256,257,258}Rf were investigated. Preliminary new results for α decay of ^{257}Rf and EC decay of ^{258}Db are reported.

INTRODUCTION

Extension of the nuclear shell model [1, 2] into regions far beyond the heaviest doubly magic nucleus, ^{208}Pb (Z = 82, N = 126) lead to the prediction of spherical proton and neutron shells at Z = 114 and N = 184 [3, 4]. This finding initiated tremendous efforts from experimental side to produce those 'Superheavy Nuclei' (SHN) and to investigate their properties, which meanwhile span a period of five decades. Similar efforts were undertaken from theory to predict the strength of these shells, ground state and decay properties etc. From experimental side strong evidence for the synthesis of elements up to Z = 118 was obtained (see e.g. [5]), indicating the existence of a region of shell stabilized nuclei in the transactinide region towards N = 184, although the 'center' has not yet been reached and information on the strength of the possible shells is still scarce. From theoretical side the situation is somewhat more complicated: while macroscopic-microscopic approaches based on the nuclear drop model [6] and the Strutinsky shell correction method [7] agree in Z = 114 and N = 184 as proton and neutron shell closures (see e.g. [8, 9]), calculations using self-consistent models like Skyrme-Hartree-Fock-Bogoliubov (SHFB) calculations or relativistic mean-field models (RMF) using NL3, NL-Z2 or NL-Z parametrisations [10, 11] disagree in locating the proton and neutron shells. Some predict Z = 120 as proton shell closure, some Z = 114 or Z = 126; concerning the neutron shell closure the Skyrme force based calculations agree in N = 184, while the RMF calculations favour N = 172. Evidently, however, all these parametrizations result in a wide area of high shell effects. On the other side, it has been already discussed extensively by Bender et al. [12] that proton (Z) and neutron (N) numbers where the shells occur are strongly dependent on details in the description of the underlying forces, especially from the values for the effective masses m* and the strength of the spin - orbit interaction. Under this aspect prediction of different shell closures in different models may be - somewhat simplified - regarded rather as a feature of 'fine tuning' of the models than as a principle disagreement. More detailed knowledge of properties and structure of heaviest nuclei is thus certainly decisive for improvements of theoretical models. Therefore such investigations will become in future even more important than synthesis of new elements.
At GSI SHE - research as an essential part of the scientific program meanwhile has a tradition of nearly forty years. Experimental techniques and sensitivity were developed and improved continuously and presently allow for the synthesis and identification of superheavy nuclei with production cross sections limits in the order of 50 fb which can be reached within reasonable irradiation times of about 150 days.
For many years the velocity filter SHIP [13] as well as chemical separation methods (see e.g. [14]) were the working horses. Recently the experimental possibilities were significantly extended by installation of the gas-filled separator TASCA [15] and the double Penningtrap spectrometer SHIPTRAP [16].

*E-mail: f.p.hessberger@gsi.de

Highlights of this research program were the identification of the new elements with atomic numbers Z = 107-112 [17], detailed nuclear structure investigations [18, 19, 20] and discovery of new K isomers [21, 22, 23] in the transfermium region, first nuclear spectroscopy measurements in an experiment leading to Z = 115 as compound nucleus [24], confirmation of elements 116, 117 [25, 26], first chemical characterization of element 108 (hassium) [27], first direct mass measurements of $^{252-255}$No [28, 29, 30], ^{255,256}Lr [30] and identification of the deformed doubly magic nucleus ^{270}Hs [31].

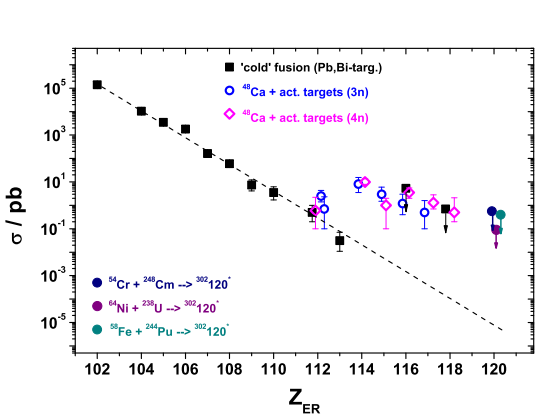

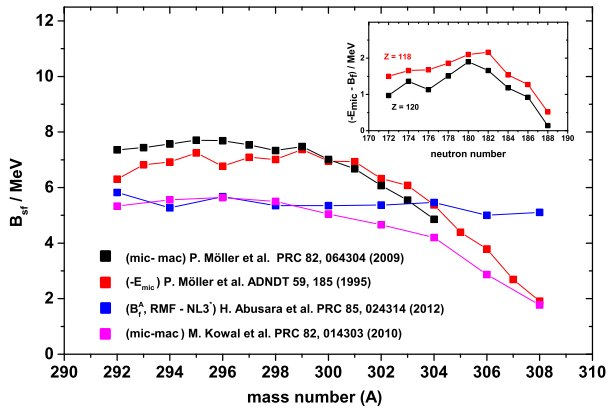

Fig. 1: (left side) Systematics of maximum production cross-sections in 'cold' fusion reactions and reactions using actinide targets. Data for element 120 are taken from [32] (^{54}Cr + ^{248}Cm), [33] (^{64}Ni + ^{238}U), and [34] (^{58}Fe + ^{244}Pu.)

Fig. 2: (right side) Comparison of calculated fission barriers for element 120 isotopes; black squares: [35], red squares:[9], blue squares: [36], violet squares: [37]; the insert shows the difference of fission barriers for element 118 and 120 isotopes between the calculations [9] and [37].

SYNTHESIS OF SUPERHEAVY ELEMENTS

Most crucial for successful experiments on the synthesis of superheavy elements (SHE) is the proper choice of the reaction and the bombarding energies. Especially the latter is essential since maximum production cross-sections (σ) are restricted to a region of typically (see e.g. [5]) $\Delta E \approx \pm 4$ MeV. For production of transactinide isotopes (Z $\geq$104) so far two classes of reactions were applied; the first uses lead isotopes (^{204,206,207,208}Pb) or ^{209}Bi as target material and 'medium heavy' ions (e.g. ^{54}Cr, ^{58}Fe,^{64}Ni) as projectiles. The use of target isotopes around the doubly magic ^{208}Pb allows for the production of low excited ($E^* <$ 20 MeV) compound nuclei (CN) at the fusion barrier, which deexcite by emission of 1-2 neutrons. These kind of reactions are therefore often denoted as 'cold fusion'. Although those reactions were successful for the synthesis of the new elements Bh(Z=107) to Cn(Z=112) it was found that the cross-sections decrease steeply at increasing proton number of the CN as seen in fig. 1. This behavior is understood as due to an increasing fusion hindrance at the fusion barrier, which is related to an increasing Coulomb repulsion between projectile and target nuclei, approximately scaling with $Z_p \times Z_t$ (where 'p' denotes the projectile, 't' the target).

The other type of reaction uses isotopes of actinide elements ranging from uranium (Z=92) to californium (Z=98) as target material and ^{48}Ca (for synthesis of elements Z$\geq$112) as projectile. These reactions are connected with some higher excitation energies ($E^* \approx$ 30-40 MeV) at the fusion barrier, leading to evaporation of 3-4 neutrons, and thus are often denoted as 'hot fusion'. As seen in fig. 1, the cross-sections for these reactions are quite stable (within a factor of $\approx$20) in the range Z = 112 to Z = 118, with an indicated maximum at Z = 114. The latter has been seen as an indication for a shell closure at this proton number [5]. As presently no target material heavier than californium (Z = 98) is available, synthesis of elements Z $\geq$ 119 requires heavier projectiles than ^{48}Ca. This results in an increase of the Coulomb repulsion by 11% for the most asymmetric possible reaction leading to element 120, ^{50}Ti + ^{249}Cf, compared to ^{48}Ca + ^{249}Cf, while the increase is only $\approx$2% going from synthesis of element 116 by ^{48}Ca + ^{248}Cm to element 118 by ^{48}Ca + ^{249}Cf. This fact introduces severe uncertainties in the scaling of the fusion hindrance at the barrier, which may be expressed by the ratio $p_{fusion}/p_{capture}$, where $p_{capture}$ stands for the probability that a di-nuclear system is formed and p_{fusion} for the probability that the di-nuclear systems evolves into a compound nu-

cleus. Nevertheless, despite of large differences in the cross-section values most of the calculations agree in predicting higher cross-sections for the more asymmetric reactions [38, 39, 40, 41, 42, 43, 44, 45].
As an example for issues related to the prediction of cross-sections some different calculations for the production of the isotopes ^{298,299}120 in the reaction ^{54}Cr + ^{248}Cm shall be discussed. Besides fusion probabilities, fission barriers, which play a decisive role for the survival probability of the compound nucleus, are critical ingredients for the calculations. Fig. 2 shows results from different model calculations for element 120 isotopes. The results of [35] (black squares) and [37] (violet squares) are obtained using the macroscopic - microscopic model, while the values of [36] are obtained from RMF calculations using the NL3 functional. The values from [9] are simply the negative shell correction energies. Evidently the results differ not only by up to 2.5 MeV, but also the trends are different. The differences between two models strongly dependent on the mass number and also from the atomic number as seen in the insert in fig. 2 where the results from [9] and [37] are compared. As a consequence calculated cross-section ratios for the different deexcitation channels (for the same CN) as well as for the same deexcitation channel for CN of different mass numbers, differ significantly depending on the underlying fission barriers and mass tables as shown in [40].
In table 1 the results from different calculations are compared; evidently not only the predicted cross section values for individual deexcitation channels vary considerably, by a factor of 5000 for the 3n-channels, by a factor of 500 for the 4n-channels, but also highest cross-sections are predicted in some calculations for the 3n-channel, in some for the 4n - channels. In addition, discrepancies of up to 13 MeV (by far larger than the widths of the excitation function) in the center-of-mass energy (E_{CM}) corresponding to the cross-section maximum for the specific deexcitation channel are evident.
These feature make it quite difficult to set up the optimum conditions (target - projectile combination, bombarding energy) for an attempt to synthesize elements Z = 119 or Z = 120.

Tab. 1: Cross-section predictions for element 120 isotopes for the reaction ^{54}Cr + ^{248}Cm

			3n(max)		4n(max)	
	fiss. barr. ref.	mass table ref.	E_{CM}/MeV	σ/fb	E_{CM}/MeV	σ/fb
Nasirov 2009 [44]			237	8000	246	800
Nasirov 2011 [40]	[46]	[46]	237	500	240	80
Nasirov 2011 [40]	[37]	[47]	237	1.5	245	1.5
Siwek-Wilczynska 2010 [42]	[47]	[47]	241	150	252	10
Siwek-Wilczynska 2012 [45]	[37]	[48]	241	7	249	5
Zagrebaev 2008 [38]	[9]	[9]	241	150	252	10

Despite these difficulties after successful penetration into the region Z > 112 by synthesizing element 114 isotopes at TASCA in the reaction ^{48}Ca + ^{244}Pu [49, 50] and one year later element 116 isotopes in the reaction ^{48}Ca + ^{248}Cm at SHIP [25] an ambitious program to synthesize the new elements 119 and 120 was started at GSI.The experimental campaign was performed in the years 2011/2012.
A second attempt to synthesise element 120 at SHIP (after applying the reaction ^{64}Ni + ^{238}U in 2007 / 2008 [33]) was the irradiation of ^{248}Cm with ^{54}Cr. The experiment was carried out in the period april to may 2011. No events that could be attributed to decays starting from an element 120 isotope were observed. A beam dose of 7×10^{18} was collected, resulting in an upper cross-section limit of 0.56 pb [32].
At TASCA the reaction ^{50}Ti + ^{249}Cf $\rightarrow$ ^{299}120 was used. The irradiation was carried out at E_{lab} = 306 MeV in the period august to october 2011; a beam dose of 1.1×10^{19} at target was collected (preliminary value) [51]. Data are still under evaluation, but so far no events that could be attributed to decays starting from an element 120 isotope were reported.
Production cross-sections for the reaction ^{50}Ti + ^{249}Cf are typically by a factor of roughly two higher than those for ^{54}Cr + ^{248}Cm. With respect to the uncertainties of mass and fission barrier predictions and treatment of the fusion probability in the vicinity of the fusion barrier this difference cannot be regarded as striking. Furthermore, the ^{248}Cm based reaction leads to a CN with N = 182 compared to N = 179 as reached with ^{50}Ti + ^{249}Cf resulting in the production of different evaporation residues. As exploration of decay properties in a mass range as wide as possible is required for each element to get detailed information about structure and stability of SHE investigation of both reactions is meaningful. It is, however, necessary to perform irradiations long enough to reach the region of predicted cross-sections (e.g. 20-50 fb predicted in [38]). Such times (>100 days) have not been available so far.
To synthesize element 119 at TASCA the reaction ^{50}Ti + ^{249}Bk $\rightarrow$ ^{299}119 was applied. The irradiation was carried out at E_{lab} = 306 MeV in two experimental runs in the period april to september 2012; a beam dose

of 4.2×10^{19} at target was collected (preliminary value) [51]. Data are still under evaluation, but so far no events that could be attributed to decays starting from an element 119 isotope were reported.

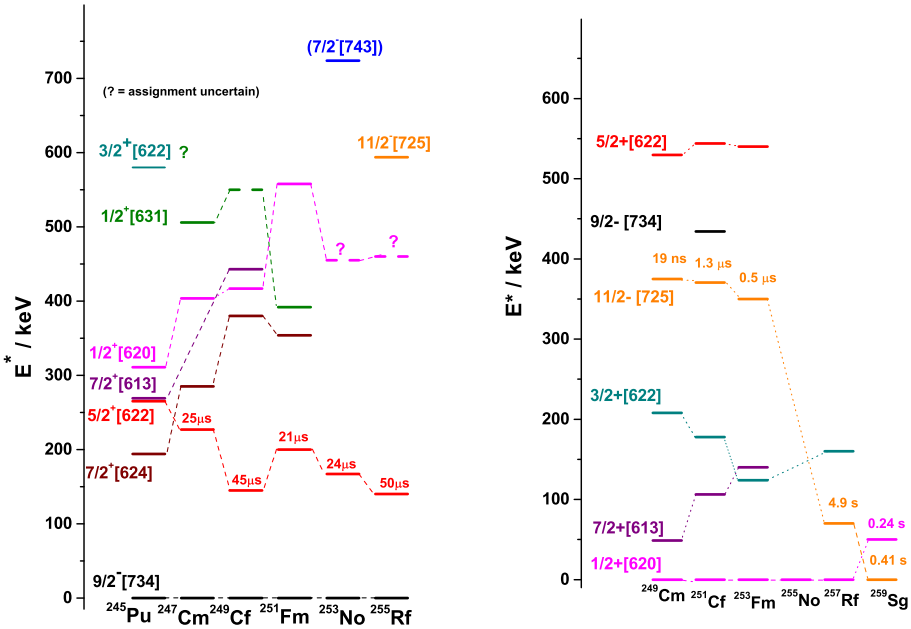

Fig. 3: (left side) Systematics of experimentally assigned low lying Nilsson levels in N = 151 nuclei

Fig. 4: (right side) Systematics of experimentally assigned low lying Nilsson levels in N = 153 nuclei

NUCLEAR STRUCTURE INVESTIGATIONS

The present status of the experiments on synthesis of SHE strongly suggests the existence of a region of shell stabilized nuclei in the region Z > 110 and N ≈ 170 - 184. Its exact location ('center') and extension, however, are experimentally not yet established and from theoretical side controversial as discussed above. Also, the strength of the shells, which may be characterized in terms of 'shell effects', is strongly model dependent and so are nuclear properties strongly related to it as ground-state mass excesses, fission barriers, Q_α - values etc. Detailed decay studies are a proper tool to shed light into the structure of nuclei. Therefore their results are at one side a stringent test for the predictive power of nuclear models and can be used on the other side as input parameters to enhance the quality of theoretical models. The experimental work at SHIP (GSI) concentrated so far on systematic investigation of low lying single particle levels in odd-mass nuclei, with some emphasis on N = 151 and N = 153 isotones in even-Z nuclei up to seaborgium (Sg, Z = 106). Recent major results were the proof of the change of the ground-state configuration in the N = 153 isotones from ^{257}Rf ($1/2^+[620]$) to ^{259}Sg ($11/2^-[725]$), the assignment of the fission branch of ^{259}Sg to the isomeric $1/2^+[620]$ - state, identification of the 5/2+[622] isomeric state and the location of the $11/2^-[725]$ - state in ^{255}Rf [52]. The present experimental knowledge on single particle levels in N = 151 and N = 153 isotones is shown in figs. 3 and 4.

After identifying the α-transition $11/2^-[725](^{259}\text{Sg}) \rightarrow 11/2^-[725](^{255}\text{Rf})$ [52] it seemed of interest also to search for the corresponding transition $11/2^-[725](^{257}\text{Rf}) \rightarrow 11/2^-[725](^{253}\text{No})$ as for ^{257}Rf the $11/2^-[725]$ level is known as a low-lying ($E^* \approx 70$ keV) isomeric state decaying by α emission [53]. As halflives of ^{257m}Rf and ^{257g}Rf are comparable (see fig. 5) both α decays could be discriminated only on the basis of the production mode as shown in fig. 5. In the direct production via ^{208}Pb(^{50}Ti,n)^{257}Rf both states are populated and consequently α decay from both states is observed [53] (black line in fig. 5), while in production via α decay of ^{261}Sg only the ground state is populated [54] (red line in fig. 5). In the low energy part of the spectrum an enhancement of α events in the range E_α = (8.25-8.30) MeV is indicated in the direct production. Indeed, this peak may suggest, similar to the case of ^{259}Sg, the α transition $11/2^-[725](^{257}\text{Rf}) \rightarrow 11/2^-[725](^{253}\text{No})$. The energy difference between this line and the transition energy of the isomer into

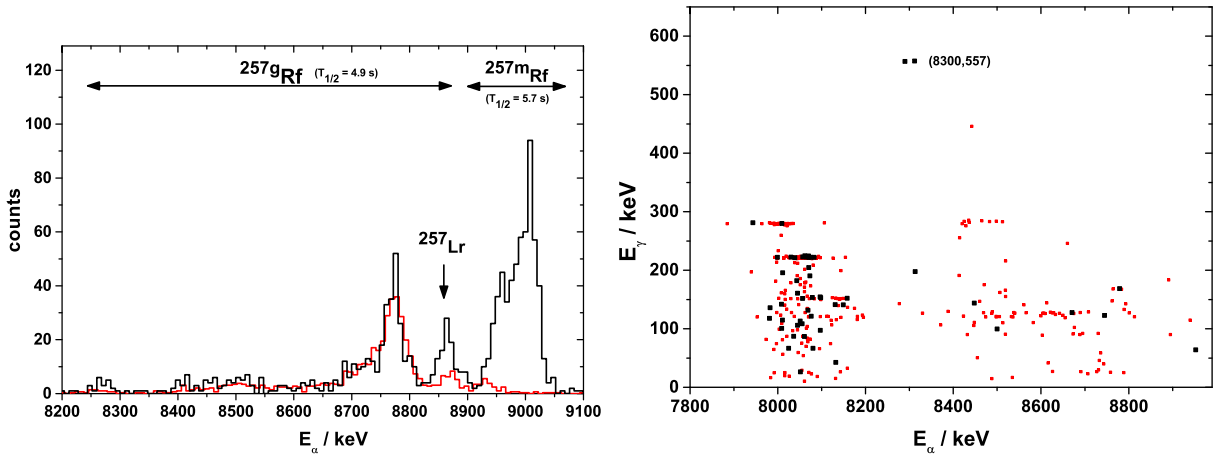

Fig. 5: (left side) Alpha decay spectrum of ^{257}Rf; black line: α spectrum observed in direct production via the reaction ^{208}Pb(^{50}Ti,n)^{257}Rf (data from [53]); red line: production of ^{257}Rf by α decay of ^{261}Sg (data from [54]); the α spectrum from direct production is downscaled (normalized to same α intensities in the interval E = 8.65 - 8.82 MeV) for better presentation.

Fig. 6: (right side) Alpha - gamma coincidence matrix for ^{253}No ($E_\alpha = 7.9$ - 8.2 MeV) and ^{257}Rf ($E_\alpha > 8.2$ MeV; red points: data from production by α decay of ^{261}Sg [54]; black points: direct production; new data from a recent SHIP experiment.

the ground-state of ^{253}No would suggest an excitation energy of $E^* \approx 760$ keV of the $11/2^-[725]$ state in ^{253}No, about 170 keV higher than in ^{255}Rf [52]. Indeed, calculations [55] settle this level in ^{253}No at an excitation energy about 100 keV higher than in ^{255}Rf.
The result of a recent α - γ coincidence measurement using the production reaction ^{208}Pb(^{50}Ti,n)^{257}Rf is shown in fig. 6. Besides single events in the range of K X-rays of nobelium (120-150 keV) and the range of γ lines (96.2, 167.1 keV) reported in [54] two events at $E_\gamma = 557.2 \pm 0.2$ keV and $E_\alpha = 8300 \pm 13$ keV are observed. Both γ events are registered between the beam pulses and appear in prompt coincidence (within ± 0.5 μs) with the α particles. An analysis of the background revealed a probability of $p < 10^{-6}$ for the coincidences to be random. The sum of the energies $E_\alpha + E_\gamma = 8857$ keV does not suggest a decay into the ground-state of ^{253}No. In addition, although the energy value is very close to the α-decay energy of ^{257}Lr the coincidences cannot be assigned to this isotope as one of α events is followed by an α decay of ^{253}No, which identifies it as decay of ^{257}Rf. On the other side, subtracting the excitation energy of the $11/2^-[725]$ state ($E^* = 70$ keV) one obtains a value $E_\alpha + E_\gamma - E^* = 8787$ keV, which is close to the energy of the transition from the ground-state of ^{257}Rf into the $5/2^+[622]$ level of ^{253}No. Considering the items above, the observed coincidence cannot be assigned to the $11/2^-[725](^{257}\text{Rf}) \rightarrow 11/2^-[725](^{253}\text{No})$ transition, as the latter level preferably would decay by an M1 transition into the ground-state and not by an E3 transition into the $5/2^+[622]$ level. On the other hand, a hindrance factor of 5-10 is evaluated for the α transition. This low value requires a transition between states of same parity and spin projection. The only level predicted at $E^* \leq 1$ MeV [55] fulfilling this request (assuming $11/2^-[725]$ as emitting level) is the $7/2^-[743]$ Nilsson level. Therefore we tentatively assign the α - γ coincidences to the transition $11/2^-[725](^{257}\text{Rf}) \stackrel{\alpha}{\rightarrow} 7/2^-[743](^{253}\text{No}) \stackrel{\gamma(E1)}{\rightarrow} 5/2^+[622](^{253}\text{No})$ and place it into the level scheme of ^{253}No as shown in fig. 7.

Electron Capture Decay of ^{258}Db

The α - decay chains starting from isotopes produced in bombardments of actinide targets with ^{48}Ca do not end in known α emitters, but are terminated by spontaneous fission (SF). So the method to identify the chain members by α - α - correlations, which requires at least one known nuclide within the decay chain, cannot be applied. Consequently assignment of those isotopes so far has been done on the basis of cross-bombardments and excitation function measurements. To achieve an unambiguous Z - identification of isotopes produced in the reaction ^{243}Am(^{48}Ca,xn)$^{291-x}$115 an attempt to measure α - K X-ray coincidences has been undertaken recently using the highly efficient spectroscopy set-up TASISpec [24]; only 'candidates' for K X-rays were observed, but no clear identification was achieved. Search for α - K X-ray coincidences requires α decay into excited levels that decay by magnetic transitions (preferably M1) with energies above

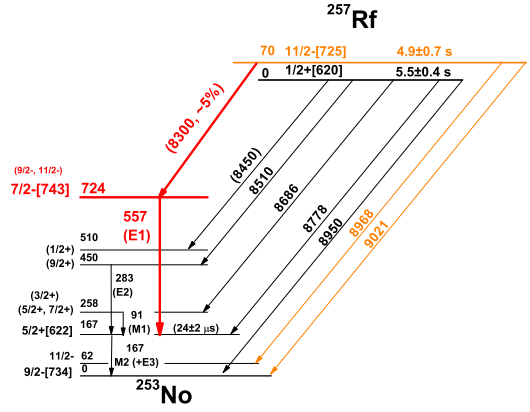

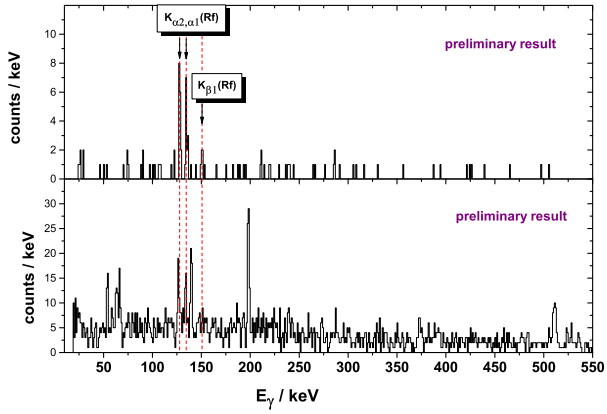

Fig. 7: (left side) proposed enhanced decay scheme of ^{257}Rf

Fig. 8: (right side) γ spectra observed in delayed coincidence with fission events produced in the reaction ^{50}Ti + ^{209}Bi $\rightarrow$ ^{259}Db* (E* = 16 MeV); upper figure: Δt(γ-SF)$\leq$36 ms, prompt coincidence of the γ with CE required; lower figure: Δt(γ-SF)$\leq$36 ms, no coincidence of the γ with CE required.

the K - binding energy (above 160 keV in the region of transactinide elements). These requirements make such search experiments a bit a gamble. As an alternative method for identification, at least of α decay chains starting from odd-odd nuclei, the SF activity terminating the chain could be used. It has been known already for a long time that SF of nuclei with odd proton and/or odd neutron numbers is strongly hindered compared to even - even nuclei [56, 57]. So in case of the decay chains starting from the odd - odd nuclei ^{294}117, ^{288}115 and ^{282}113 (see fig.9, left hand side) it seems questionable if the terminating SF activities are indeed the odd - odd nuclei produced by α emission. It could be also assumed that these nuclei undergo electron capture decay (EC) and SF of the EC - daughters, which are even - even nuclei, is observed. Indeed, short SF halflives of the EC daughters of ^{266,268,270}Db are predicted: T$_{SF}$ = 23 s (^{266}Rf), T$_{SF}$ = 1.4 s (^{268}Rf), T$_{SF}$ = 20 ms (^{270}Rf) [58]. So, measuring K X-rays from EC decay might be an alternative method for Z - identification of the decay-chain members, since due to the high fluorescence yield of $\omega_K > 0.97$ K - capture is a certain source for K X-ray production. To test the feasibility of such a method in the region of transactinides we chose the isotope ^{258}Db. The isotope had been first synthesized about thirty-five years ago in the reaction ^{209}Bi(^{50}Ti,n)^{258}Db and was identified by α - α - correlations to its daughter products ^{254}Lr and ^{250}Md. The atomic number was assured by α - K X-ray coincidences for α decays of ^{258}Db as well as the daughter product ^{254}Lr [59]. Evidence for two long-lived states decaying by α emission was found [59]. In parallel also an SF activity of the same half-life(s) was observed. Due to the assumed strong fission hindrance of odd-odd nuclei the activity was attributed to the EC - daughter ^{258}Rf (see fig. 9, right hand side). In a recent experiment delayed coincidences between K - X-rays from EC - decay of ^{258}Db (produced via ^{209}Bi(^{50}Ti,n)^{258}Db) and SF of ^{258}Rf was searched for. The preliminary results are shown in fig. 8. The upper part shows the spectrum of γ - rays preceding an SF event within 36 ms; a prompt coincidence of the γ event with a low energy event (E < 600 keV), interpreted as a conversion electron, was reqired. In the lower spectrum the same time limit was used, but no coincidence with a CE was required. Evidently the request for a coincident CE drastically reduces the background of γ radiation. Still, the K$_{\alpha 1,2}$ are clearly visible in the lower spectrum and their intensities are about 50% higher than in the spectrum where a coincidence with an CE was required. The energy distribution of the CE indicates an energy E* > 500 keV of the level populated by the EC decay (which corresponds to about the energy expected for the 8^{+} - state of the ground-state rotational band of ^{258}Rf), while the strong component of K X-rays not in coincidence with CE suggests also the population of a state at low excitation energy, delivering CE with a sum energy below the registration threshold of E $\approx$ 80 keV. This finding suggests that EC decay from two levels in ^{258}Db is observed, one of low spin and one of high spin, corroborating the assumption of two long-lived isomeric states drawn from the analysis of the α - decays [59]. From the time differences between K - X-rays and fission events we obtain a half-life of T$_{1/2}$ = 14.5$\pm$5.2 ms, which is in perfect agreement with the value T$_{1/2}$ = 14.7$^{+1.2}_{-1.0}$ ms reported for ^{258}Rf reported in literature [60].

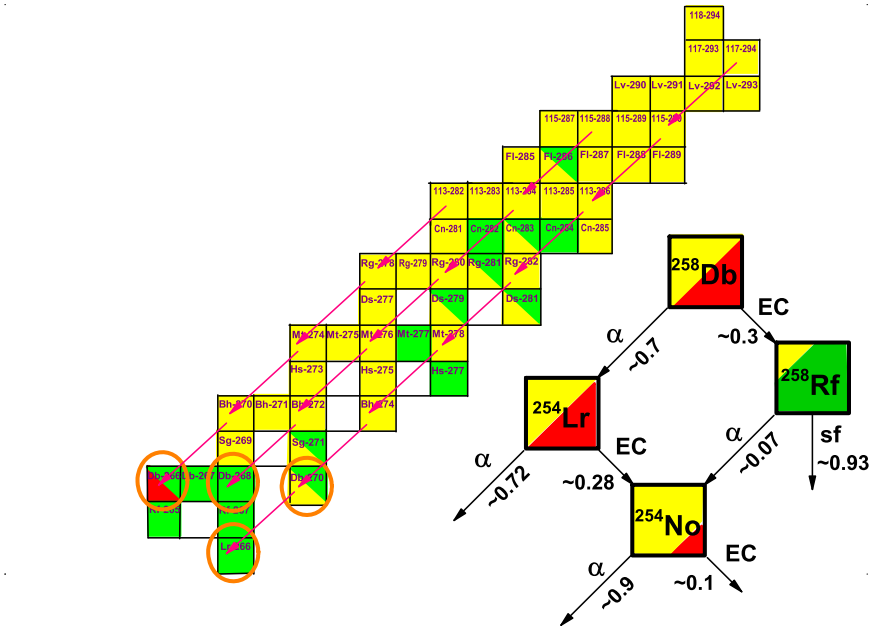

Fig. 9: (left side): alpha decay chains starting from the odd-odd nuclei ^{294}117, ^{288}115 and ^{282}113. (right side): decay pattern of ^{258}Db

CONCLUSIONS

Superheavy elements represent a specific species of exotic nuclei. As liquid drop fission barriers have vanished, they owe their existence, stability and decay properties solely due to their shell structure, which is extremely sensitive to details of the nuclear force. Thus they represent a unique laboratory to study fundamental interactions.

Presently available facilities and experimental techniques allowed for the synthesis of elements up to Z = 118. 'Detailed' decay studies including measurement of γ rays were possible up to Z = 115 so far. Experiments aimed to the synthesis of heavier elements, also performed at GSI, did not show positive results on the basis of present status of data evaluation.

Experiments performed in recent years revealed a vast of new data allowing for a much deeper insight in ground-state and decay properties of SHE as well as in their nuclear structure. This certainly will serve also as a basis for the development of advanced nuclear models. Still, the research work is rather at the beginning but is already fascinating enough to justify the demand for new facilities and set-up allowing to increase sensitivity significantly, which is required to successfully synthesize new elements, to perform nuclear structure investigations of high quality in the region of the expected spherical proton and neutron shells and to investigate the properties of the nuclei there in detail. This will lead to new insights in understanding the existence and stability of our world.

ACKNOWLEDGMENT:
The data of the recent SHIP experiments presented here were obtained in collaboration with S. Antalic, B. Andel, Z. Kalaninova (Comenius University Bratislava), D. Ackermann, J. Piot, M. Vostinar (GANIL, Caen), J. Even, M. Laatiaoui (Helmholtz Institut Mainz) and I. Kojouharov (GSI, Darmstadt).

REFERENCES

[1] M. Göppert-Mayer, Phys. Rev. **74**, 235 (1948).
[2] O. Haxel et al., Phys. Rev. **75**, 1766 (1949).
[3] A. Sobiczewski et al., Phys. Lett. **22**, 500 (1966).
[4] H. Meldner, Arkiv för fysik **36**, 593 (1967).
[5] Yu. Ts. Oganessian, J. Phys. G: Nucl. Part. Phys. **34**, R165 (2007).
[6] C.F. von Weizsäcker, Z. Phys. **96**, 431 (1935).

[7] V.M. Strutinsky, Nucl. Phys. A **95**, 420 (1967).
[8] R. Smolanczuk, A. Sobiczewski, Proc. EPS Conf. 'Low Energy Nuclear Dynamics', St. Petersburg 1995, eds. Yu.Ts. Oganessian et al., World Scientific, Singapore, New Jersey, London, Hong Kong 1995, 313 (1995).
[9] P. Möller et al., At. Data and Nucl. Data Tab. **59**, 185 (1995).
[10] K. Rutz et al., Proc. of the Second Int, Conf. 'Fission and Properties of Neutron-Rich Nuclei', St. Andrews 1999,ed. J.H.Hamilton et al., (World Scientific, Singapore, New Jersey, London, Hong Kong, 2000), 449 (2000).
[11] M. Bender et al., Rev. Mod. Phys. **75**, 121 (2003).
[12] M. Bender et al., Phys. Rev. C **60**, 034304 (1999).
[13] G. Münzenberg et al., Nucl. Instr. Meth. **161**, 65 (1979).
[14] M. Schädel, Eur. Phys. J. D **45**, 67 (2007).
[15] A. Semchenkov et al., Nucl. Instr. Meth. in Phys. Res. B **266**, 4153 (2008).
[16] M. Block et al., Eur. Phys. J. D **45**, 39 (2007).
[17] S. Hofmann, G. Münzenberg, Rev. Mod. Phys. **72**, 733 (2000).
[18] F.P. Heßberger et al., Eur. Phys. J. A **26**, 233 (2005).
[19] F.P. Heßberger et al., Eur. Phys. J. A **30**, 561 (2006).
[20] F.P. Heßberger, Eur. Phys. J. D **45**, 33 (2007)
[21] S. Hofmann et al., Eur. Phys. J. A **10**, 5 (2001).
[22] B. Sulignano et al., Eur. Phys. J. A **33**, 327 (2007).
[23] F.P. Heßberger, Phys. Atom. Nuclei **70**, 1445 (2007).
[24] D. Rudolph et al., Phys. Rev. Lett. **111**, 112502 (2013).
[25] S. Hofmann et al., Eur. Phys. J. A **48:**62 (2012).
[26] J. Khuyagbaatar et al., Phys. Rev. Lett. **112**, 172501 (2014).
[27] Ch. E. Düllmann et al., Nature **418**, 859 (2002).
[28] M. Block et al., Nature **463**, 785 (2010).
[29] M. Dworschak et al., Phys. Rev. C**81**, 064312 (2010).
[30] E. Minaya Ramirez et al., Science **337**, 1207 (2012).
[31] J. Dvorak et al., Phys. Rev. Lett. **97**, 242501 (2006).
[32] S. Hofmann et al., GSI Scientific Report 2011, **PHN-NUSTAR-SHE-01** 205 (2012).
[33] S. Hofmann et al., GSI Scientific Report 2008, **NUSTAR-SHE-01**, 131 (2009).
[34] Yu. Ts. Oganessian, Phys. Rev. C**79**, 024603 (2009).
[35] P. Möller et al., Phys. Rev. C **79**, 064304 (2009).
[36] H. Abusara et al., Phys. Rev. C **85**, 024314 (2012).
[37] M. Kowal et al., Phys. Rev. C **82**, 014303 (2010).
[38] V. Zagrebaev, W. Greiner, Phys. Rev. C**78**, 034610 (2008).
[39] G.G. Adamian et al., Eur. Phys. J. A **41**, 235 (2009).
[40] A.K. Nasirov et al., Phys. Rev. C **84**, 044612 (2011).
[41] Z.H. Liu, Jing-Dong Bao, Phys. Rev. C **80**, 054608 (2009).
[42] K. Siwek-Wilczynska et al., Int. J. Mod. Phys. E **19**, 500 (2010).
[43] Nan Wang et al., Phys. Rev. C **85** 041601(R) (2012).
[44] A.K. Nasirov et al., Phys. Rev. C **79**, 024606 (2009).
[45] K. Siwek-Wilczynska et al., Phys. Rev. C86, 014611 (2012).
[46] P. Möller, J.R. Nix, J. Phys. G: Nucl. Part. Phys. **20**, 1681 (1994).
[47] I. Muntian et al., Phys. Atom. Nucl. **66**, 1015 (2003).
[48] M. Kowal et al., arXiv:1203.5013 (2012).
[49] C.E. Düllmann et al., Phys. Rev. Lett. **104**, 252701 (2010).
[50] J. Gates et al., Phys. Rev. C **83**, 054618 (2011).
[51] J. Khuyagbaatar et al., GSI Scientific Report 2012 **PHN-ENNA-EXP-01**, 131 (2013).
[52] S. Antalic et al., Eur. Phys. J. A **51:**41 (2015).
[53] F.P. Heßberger et al., Z. Phys. A **359**, 415 (1997).
[54] B. Streicher et al., Eur. Phys. J. A **45**, 275 (2010).
[55] A. Parkhomenko, A. Sobiczewski, Acta Phys. Polonica B **36**, 3115 (2005).
[56] J. Randrup et al., Nucl. Phys. A **217**, 221 (1973).
[57] D.C. Hoffman et al., Nucl. Phys. A **502**, 21c (1989).
[58] R. Smolanczuk et al., Phys. Rev. C **52**, 1871 (1995).
[59] F.P. Heßberger et al., Eur. Phys. J. A **41**, 145 (2009).
[60] J. Gates et al. Phys. Rev. C **77**, 034603 (2008).

FARCOS: A new correlator array for nuclear reaction studies at Fermi energy

E.V.Pagano[1,2*], L. Acosta[4], L. Auditore[5], C. Boiano[6], G. Cardella[3], A. Castoldi[7]. D' Andrea[3], E. De Filippo[3], S. De Luca[5], F. Fichera[3], L. Francalanza[8], N. Giudice[1,3], B. Gnoffo[3], A. Grimaldi[3], C. Guazzoni[6,7], G. Lanzalone[2,9], I. Lombardo[8], T. Minniti[11,12], S. Norella[5], A. Pagano[3], M. Papa[3], S. Pirrone[3], G. Politi[3], F. Porto[1,2], L. Quattrocchi[5], F. Rizzo[1,2], P. Russotto[3], G. Saccà[3], A. Trifirò[5], M. Trimarchi[5] , G. Verde[3,10], M. Vigilante[8].

[1]Università di Catania, Catania, Italy.
[2]INFN Laboratori Nazionali del Sud, Catania, Italy.
[3]INFN Sezione di Catania, Catania, Italy.
[4]Istituto de Física, Universidad Nacional Autónoma de México, México D.F. 01000, México.
[5]Dipartimento di Fisica e Scienze della Terra, Università di Messina & INFN gr. collegato di Messina, Messina, Italy.
[6]INFN Sezione di Milano, Milano, Italy.
[7]Politecnico di Milano, Dipartimento di Elettronica, Informazione e Bioingegneria, Milano, Italy.
[8]INFN Sezione di Napoli & Dipartimento di Fisica, Università di Napoli Federico II, Napoli, Italy.
[9]Università Kore Enna, Enna, Italy.
[10]Institut de Physique Nucléaire d' Orsay, Orsay, France.
[11]CNR – Istituto per i Processi Chimico-Fisici, Messina, Italy.
[12]ISIS Facility, Science and Technology Facilities Council, Rutherford Appleton Laboratory, Oxfordshire, UK.

Abstract

Nuclear matter under extreme conditions can be studied in the laboratory with heavy-ion (H.I.) collisions. In this case one can indeed vary both the incident energy and mass asymmetry. By exploring different impact parameters and rapidity regions it is possible to access nuclear densities that extends above and below saturation density. Such opportunities allow one to learn more about the nuclear equation of state and its implications in astrophysics phenomena such as supernovae explosions and neutron stars properties. Furthermore, during the dynamical evolution of the studied systems, short living exotic states can be produced and their properties can be studied by detecting the final products of resonance decays. All these phenomena involve time scales that need to be accessed with multi-particle correlation measurements.

Experimental observables, such as linear momentum and energy, sensitive to both space-time and spectroscopic properties of the nuclear systems produced in the H.I. collisions, need to be measured with both high angle and energy resolution over a large solid angle coverage. In order to address this problem, dedicated geometrically flexible correlator arrays are useful tools to be coupled with 4π detectors. One of these arrays is FARCOS, presently under construction at the INFN Sezione di Catania and Laboratori Nazionali del Sud (LNS). The FARCOS (Femtoscope ARray for COrrelations and Spectroscopy) was designed as an array of twenty telescopes, each composed by two Double Sided Silicon Strip Detectors (DSSSD), of thickness $300\mu m$ and $1500\mu m$, respectively, followed by four CsI(Tl) crystals read-out by silicon photodiodes. In this contribution a brief report of the present status of FARCOS array and future perspectives will be presented. Particular attention will be devoted to some preliminary results obtained in a recent experiment performed using a prototype of 4 clusters of FARCOS array coupled with CHIMERA detector.

INTRODUCTION

The study of dynamics of nuclear reactions in heavy ion collisions at Fermi energy (20 MeV/u < E/A< 200 MeV/u) is an active area in nuclear science. In fact, depending on incident energy and impact parameter, an impressive range of physical phenomena occur within large time-scales (from 10 to 1000 fm/c) with the excitation of different degrees of freedom characterized by the competition between one-body and nucleon-nucleon dissipation mechanisms which are revealed through imprints on space-time and particle-particle correlations. In particular, violent head-on collisions, within time-scales of the order of 100 fm/c, experience a collective compression where the nuclear density in the overlapping region is predicted to achieve values well above the value of the saturation density ρ_0 ($\approx 0.17\ nucleon/fm^3$) [1, 2]. Then, the evolution of the

*E-mail: epagano@lns.infn.it

system is predicted to undergo an expansion phase: the density goes down to a freeze-out configuration with significantly lower value (of the order of $0.3\rho_0$) and a rapid multi-fragmentation of the system in many excited clusters and light particles takes place. This scenario opens the possibility to explore transient systems under extreme conditions with baryonic density lower or larger than the one characterizing the saturation properties of normal nuclear matter [3]. The studies have shown that beside nuclei lying close to the stability valley also exotic isotopes of short life-decay time are produced in different phases of the reaction. In particular, their decay properties can be studied by measuring the correlation properties of the emitted particles in order to pin down valuable spectroscopic information of unbound exotic states [4, 5, 6, 7].

On this aspect heavy ion collisions can be viewed not only as a powerful tool to study nuclear dynamics and the decay path towards equilibrium configurations but also as unique opportunities in terrestrial laboratory to produce several nuclear exotic species in one single experiment. It is within this complex scenario that experimental methods and techniques for probing space-time properties of the different emitting nuclear sources have been developed. Furthermore, with the advent of new-generations radioactive ion-beam facilities (RIB), like as examples SPES at LNL, SPIRAL II at GANIL, FAIR at GSI or FRIB at MSU or the possible upgrade of the heavy ion CS facility in Catania towards high intensity beams, such studies and methods assume renewed interest in order to study the structure of rare isotopes and the propriety of isospin asymmetric nuclear matter [8], so, bringing together also the interest of the nuclear astrophysics community.

From the experimental point of view, both high energy and angular resolution of dedicated detection systems are mandatory requests. For this reason experimental efforts have been devoted at the Fermi energies to design specific and flexible position sensitive detector arrays to be coupled to 4π detectors in order to characterize the reaction in event-by-event mode (total multiplicity of emitted particles, reaction plane determination, etc.) [9, 10, 11]. In this paper we briefly describe the next-generation correlator FARCOS (Femtoscope ARray for COrrelation and Spectroscopy) [12, 13, 14] that is under construction in Catania, in collaboration among INFN-LNS and Sezione di Catania and gr. coll. di Messina, INFN Sezione di Milano and Politecnico di Milano and INFN sezione di Napoli. We briefly describe also the first test with beam in Catania, during the INKIISSY experiment performed on April 2013 to study $^{124}Xe + ^{64}Zn$ reactions at 35 MeV/u.

FARCOS

Description and characterization

FARCOS is a modular array of telescopes each one consisting of three detection stages. The first two stages are two Double Sided Silicon Strip Detectors (DSSSD) with 32 vertical strips in the front side and 32 horizontal strips in the back side. For both sides the area is $6.4 \times 6.4\ cm^2$. The first stage is 300 μm thick and the second one is 1500 μm thick. The last stage consists of four CsI(Tl) crystals of 6 cm of thickness read by a photodiode, of area $18 \times 18\ mm^2$. The Fig. 1 shows the three stages of a single cluster of FARCOS (left side) and their typical close assembling (right side). It is important to note that each cluster has been designed to be equipped with 132 independent read-out electronics channels.

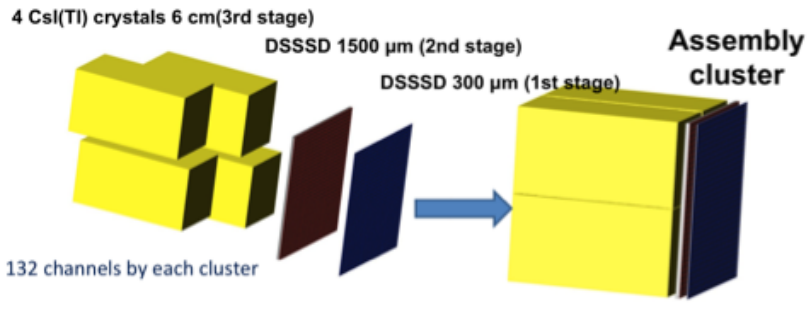

Fig. 1: schematic view of a cluster of FARCOS.

Particle identification techniques in FARCOS are performed by ΔE/E, pulse shape (PSD) and Time of Flight (TOF) methods. Beside the innovative design, portability and modularity are important characteristics making feasible the easy coupling with 4π detectors or other kind of correlators and/or magnetic spectrometers. Digital Signal Acquisition (DSA) is also envisaged by using integrated and reconfigurable electronics jointly with the possibility of updating and upgrading.

Few words about the front-end read out electronics. As preliminary prototypes, we were using improved versions of CHIMERA-like standard preamplifiers (PAC) for both CsI(Tl) crystals and silicon detectors already developed to match with the necessity of low electronics noise and TOF performances as required in CHIMERA detector [15]. As first step of the R&D activity, the read-out of 32 silicon strips was performed by a compact housing (86x80x10 mm (NPA-16FL), 98x80x15 mm (NPA-16FE)) allocating 32-channels Charge Preamplifiers (PACs) with pseudo-differential signal output of low power consumption (<900 mW for 32 channels).

Characterization of DSSSDs with Beam and Identifications and calibrations procedures

FARCOS was tested and coupled with the 4π CHIMERA [16] for the first time during the experiment INKIISSY (INverse KInematic ISobaric System) on April 2013, performed at INFN-LNS of Catania using the K800 Superconducting Cyclotron. The idea of the INKIISSY experiment was to use projectile/target combination having the same mass of the neutron rich $^{124}Sn + ^{64}Ni$ system and N/Z similar to the neutron poor $^{112}Sn + ^{58}Ni$ one, that is the system $^{124}Xe + ^{64}Zn$, at the same bombarding energy of 35 MeV/u as in the previous experiment [17] in order to disentangle Isospin against size effects in dynamics fission reactions. The experiment was performed with the CHIMERA detector in his full configuration in coincidence with four detection modules of FARCOS prototype. In the experimental configuration FARCOS covered a theta angle in the lab frame in the range of polar angles $\theta_{lab} \approx 16^\circ \div 44^\circ$ and azimuthal opening of value $\Delta\phi \approx 75^\circ$. The detector was positioned close to the target at a distance of 25 *cm* with a solid angle coverage of ≈ 262 *msr* (see Fig. 2). Evidently in this configuration a portion of CHIMERA was shielded by FARCOS telescopes. However, signals coming from the shielded telescopes of CHIMERA were used to investigate for the possibility to detect neutrons coming from reactions in CsI(Tl) scintillators [18] that is part of an R&D work in progress aimed to extend capability of CHIMERA also to neutral particles including γ ray [19]. In this first experiment different configurations of the threshold settings were investigated in order to study the response of the whole cluster against hits multiplicity and cross talk among different strips. The observed hits multiplicity was studied in some details.

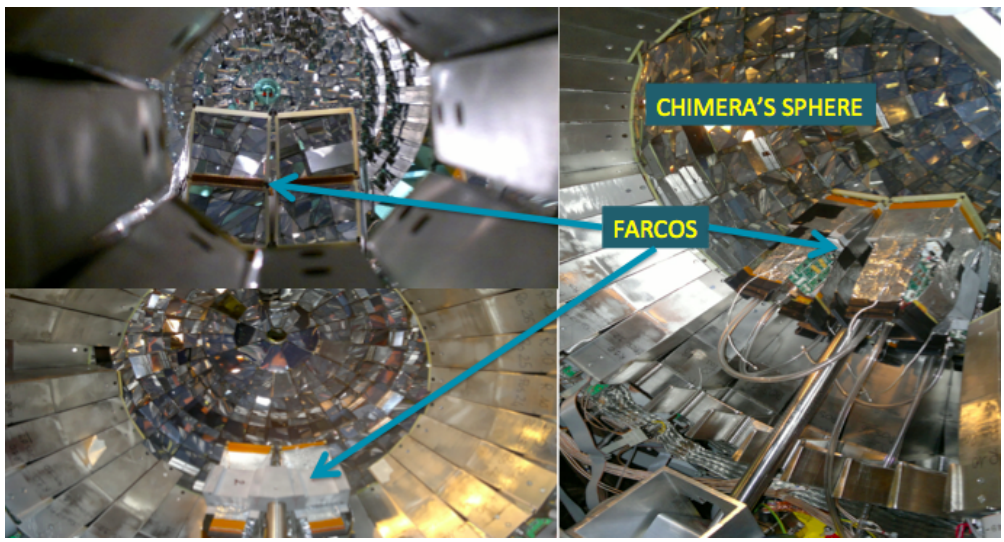

Fig. 2: The INKIISSY experimental setup.

After a cut in the total strips hits multiplicity for physical reasons ($1 \leq mult_{DSSSD} \leq 8$) good $\Delta E/E$ identification matrices between the first two DSSSD have been obtained. A typical identification matrix of IMFs is reported in Fig. 3. In Fig. 3 is shown, as an example, a ΔE/E identification matrix between the fifth strip of the first DSSSD stage and the correlated twenty-sixth strip of the second DSSSD stage.

Identifications and calibrations procedures

For the identification of the particles and for energy and time calibrations it is highly recommended to devise automatic procedures in order to reduce as much as possible time-consuming and man power. To achieve a satisfactory method for saving of time and man power it was necessary to study in detail the response function of single-independent strips and a suitable ensemble of them. As a first guess it was

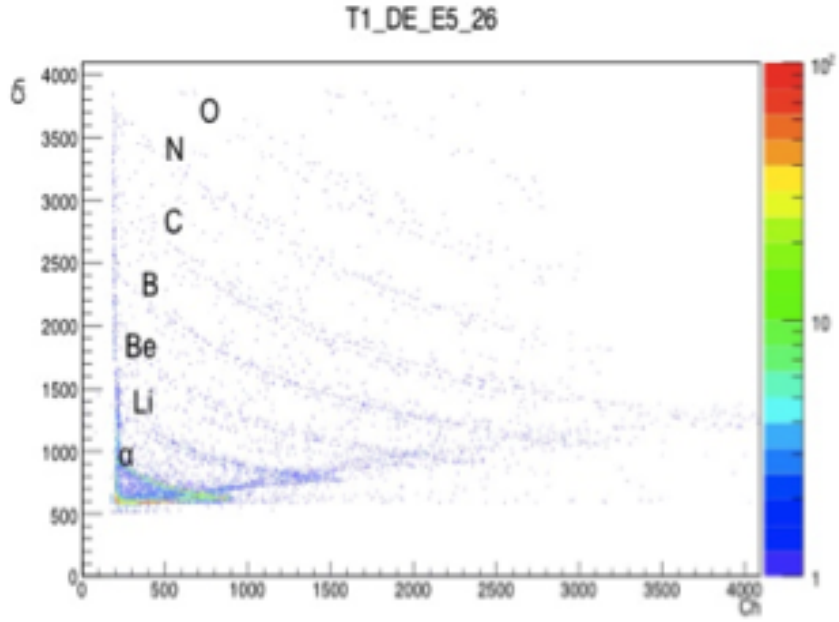

Fig. 3: ΔE/E identification matrix for 5th strip of first DSSSD stage and 26th of second.

possible to choose two simple ways to perform the particle identification. One way was to study the particle identification by doing the analysis strip by strip (single-strip way). Evidently, it means a time consuming identification job; indeed if the method was extensively applied to all the strips it would require to analyze about 100 identification matrices for each cluster and the integration of the available statistics collected by integrating (in this test) 320 runs of the experiments. The obvious advantage of this single-strip way is to exploit the full resolving power of each cluster of the apparatus. Alternatively, it was possible to perform the identification by adding the statistics collected by a given number of independent strips (sum-strips way) in such a way to obtain a comparable statistics as in the single-strip way and to minimize the small intrinsic differences(thickness, active depletion, resistivity,....) among the independent strips. After some studies performed on different strips it was chosen to add eight strips by integrating the statistics of a sample of about 15% of the available runs. Notice that by adding the statistics of 8 strips the effort for data analysis was substantial reduced of about a factor 6. In principle it should be possible to add statistics of all the strips in the same DSSSD by assuming that the differences in the thickness among the different strips were negligible. However, due to the independent electronic channels for each strip it is necessary to homogenize all the pulses of the electronic signals (from preamplifier to DAC) or maybe better to perform the full energy calibration of the two stages of DSSSD. As main result for the fragment identification, it has to be noticed that in the present preliminary study for light ions, i.e., $3 \leq Z \leq 6$, where Z is the atomic number, both methods have shown a comparable and satisfactory resolution (see Fig. 4). However, in the range of atomic number $7 \leq Z \leq 10$ the resolution of the isotopic identification has shown the tendency for better results in the case of one-strip way (see Fig. 5) than in the case of sum-strips way [14].

Tests of GET electronic

Description of GET Electronic

The GET electronics for read-out and DAC (Generic Electronic for TPC), is an integrated system of data acquisition designed to handle a very large number of independent electronic channels (more than 30kch). GET process starts from the analog charge signals coming from the detectors and goes on towards digital acquisition and storage (DAC). The innovative GET performances such as high versatility and compactness make the GET project also a good candidate to process signals in a detector array like FARCOS having a large number of electronic channels (132 for each cluster) in a very small volume (about 7x7x10 cm^3).

GET is based on a chip, AGET, that is able to process 64 independent electronic channels with a preamplifier, a filter, a discriminator and with an array of 512 capacitors for each channel. The sampling frequency is in the range from 1 to 100 MHz. Four of this AGET chips are allocated on another board, called ASAD, where the analog signals are digitalized. Each ASAD is able to process 256 channels. These ASADs

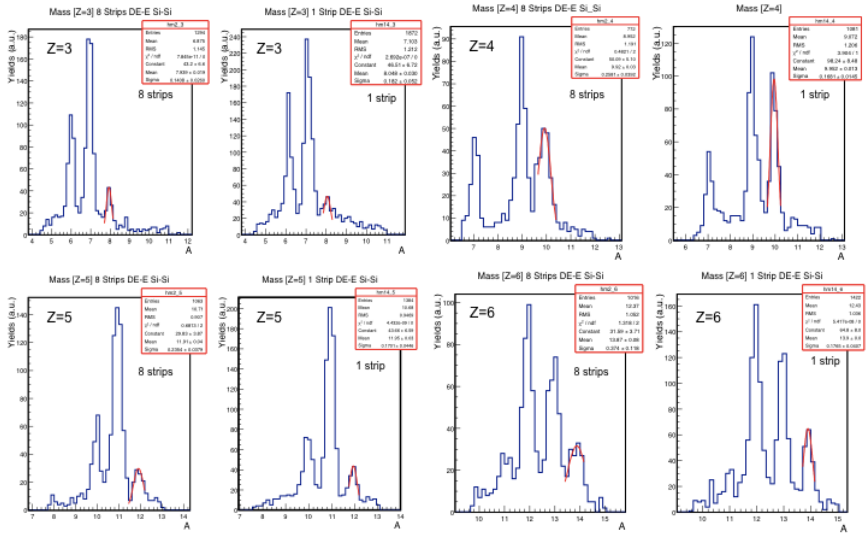

Fig. 4: Isotopic identification resolution for fragments having charge between 3≤Z≤6 as compared with the two identification methods (see text).

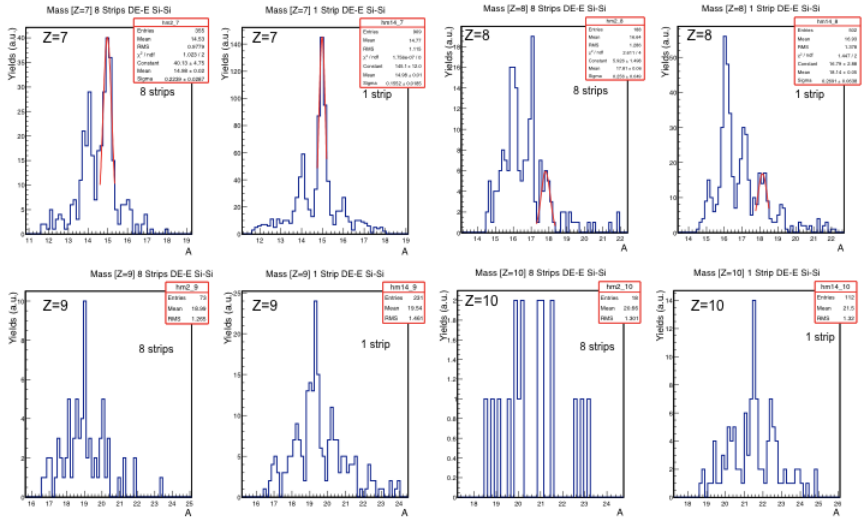

Fig. 5: Idem pictures as in Fig.4 for fragments having charge between 7≤Z≤10.

are read-out by an electronic module called CoBo that is able to collect signals from 4 ASADs (1024chs). The CoBos are allocated in a specific crate, the μTCA, allowing to allocate up to 10 CoBos. In this crate is also present the MUTAND card that is useful for the trigger handling and to synchronize the different CoBos. MUTAND is also performing the inter-communications among the different devices of the DAC system and even among different DAC systems [20].

Description of the first test in CsI(Tl) and DSSSD

In our more recent work we have tested both the DSSSD strip detectors and the CsI(Tl) crystals read by photodiodes. As already seen in the past chapters, the signals of the detectors were processed by improved versions of standard PAC in use in CHIMERA Detector (i.e., the GET preamplifiers were not used). After that, the signals were processed by GET electronic and the results are shown in Fig. 6 and Fig. 7.

Fig. 6 reports on the CsI(Tl) crystal's tests. In this case, a Tandem beam @ INFN-LNS of Catania of ^{7}Li of a total energy of 27 MeV was used. The used targets were gold (red line), hydrogenated carbon (violet line) and deuterated carbon (blue line). The left panel corresponds to the case of standard CHIMERA data acquisition, while on the right panel the GET data acquisition is reported. In our tests we found that, in the case of the GET data acquisition, the energy resolution was about a factor 2 better than in CHIMERA one.

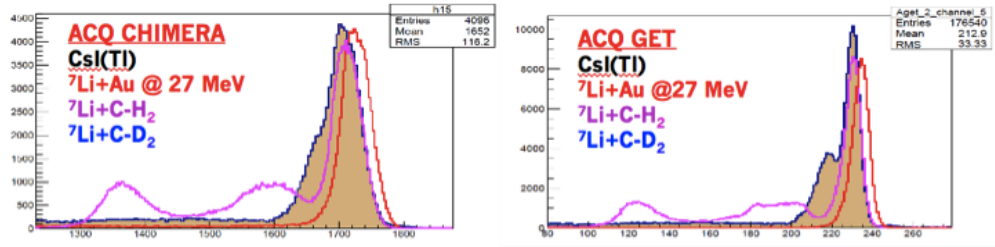

Fig. 6: Test of CsI(Tl) crystals. The beam is ^{7}Li @ 27 MeV and the three colors are related to the three different target used in the experiment, in red Gold target, violet CH_2 and blue CD_2.

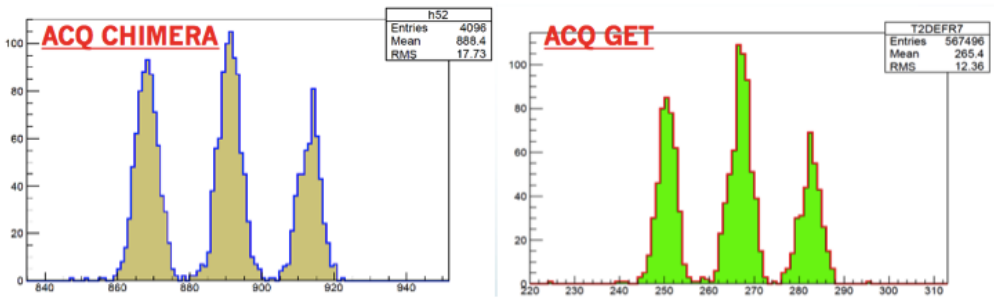

Fig. 7: Test of DSSSD. In this test the peaks are related to the Alpha particles emitted from a typical three peak alpha source.

In Fig. 7 the DSSSD tests performed with alpha source are shown. In this case, a standard three peaks alpha source (^{231}Am, ^{239}Pu, ^{244}Cm) was used. Comparing the left panel (CHIMERA data acquisition) to the right panel (GET data acquisition) we can conclude that the obtained energy resolution around the energy value of 5 MeV looks like almost comparable for the two compared DAC acquisition systems.

Milestones of FARCOS construction

Milestones of FARCOS constructions can be briefly summarized as follows. The GET electronics tests (standard configuration) will be completed within the first semester of 2015 year, while in the second semester it is expected to start with procedures to test the ASIC preamplifiers. In 2016 six new clusters are planned to be assembled; in 2017 and in 2018 four new clusters for each year are planned to be added. The final configuration of 20 clusters of FARCOS array is planned to be in operation on 2019.

CONCLUSIONS

In conclusion, we have performed different tests to extract performances of four clusters of the first FARCOS prototype. The obtained results are encouraging and indicate good energy resolution for both light charged particles (not shown in the paper) and light fragments detected in the Silicon strips allowing for a satisfactory isotopic identification for light fragments, that is mandatory requirement for new generation correlators in HI physics with both stable and exotic beam at intermediate energies. In the spirit of portability and versatility for both mechanical handling and data analysis (On line and off line), some procedures are under developing to make faster and easier the calibration and the identification analysis. An analysis of the data is going on to calibrate the energy vs. pixel position in order to obtain relevant physics data on space-momentum correlations of the observed charged particles. Beside the light fragments, the identification and calibration procedures will be extended also to the light charged particles (p,d,t,..) measured in the CsI(Tl) crystals.

About the electronics front end and the data acquisition, the GET compact integrated electronic could represent an appropriate and feasible method to process a very large number of channels in a portable and compact way. However, further tests are in progress. In the second part of the 2015 a first test of new ASICs preamplifiers under development are envisaged. The new preamplifiers will be integrated in the mechanical structure of FARCOS in order to be coupled with GET. In the next five years, it is expected to complete the full configuration of FARCOS. With the new device, further new results will be expected in solving open problems in the field of nuclear physics (dynamics and thermodynamics) and astrophysics (structure of unbounded states and their decay properties) and in opening new perspectives. However, since 2015 year

FARCOS prototype will play an important role in two experiments already approved at LNS, i.e., CLIR and SIKO. Beside that, the detector is also involved in a couple of Letters of Intent submitted to the new radioactive Ion beam facility, SPES, that is under construction at INFN-Laboratori Nazionali di Legnaro.

REFERENCES

[1] Bao-An Li et al., Phys. Rev. C **71**, 044604 (2005).
[2] V. Baran et al., Nucl. Phys. A **730**, 329 (2004).
[3] F. Gulminelli et al., Eur. Phys. J. A **30**, 1 (2006).
[4] R. Hanbury Brown, R.Q. Twiss, Nature **178**, 1046 (1956).
[5] S.E. Koonin, Phys. Lett. B **70**, 43 (1977).
[6] R.J. Charity et al., Phys. Rev. C **52**, 3126 (1995).
[7] W.P. Tan et al., Phys. Rev. C **69**, 061304 (2004).
[8] V. Baran, M. Colonna, V. Greco, M. Di Toro, Phys. Rep. **410**, 335 (2005).
[9] B. Davin et al., Nucl. Instrum. Methods Phys. Res. A **473**, 302 (2001).
[10] E. Pollacco et al., J.L. Duggan, I.L. Morgan (Eds.), AIP Conf. Proc., **680**, 313 (2003).
[11] M.S. Wallace et al., Nucl. Instrum. Methods Phys. Res. A **583**, 302 (2007).
[12] G. Verde et al., J. Phys.: Conf. Ser. **420**, 012158 (2013).
[13] L. Acosta et al., EPJ Web Conf. **31**, 00035 (2012).
[14] E.V. Pagano et al., EPJ Web Conf. **88**, 00013 (2015).
[15] C. Boiano et al., IEEE Trans. Nucl. Sci. **5**, 1931 (2004).
[16] E. De Filippo, A. Pagano, Eur. Phys. J. A **50**, 32 (2014), and reference therein.
[17] P. Russotto et al., Phys. Rev. C **91**, 014610 (2015).
[18] L. Auditore et al., EPJ Web Conf. **88**, 01001 (2015).
[19] G. Cardella et al., Nucl. Instrum. Methods Phys. Res. A **799**, 64 (2015).
[20] E. Pollacco et al., Phys. Procedia **37**, 1799 (2012).

Shapes and collectivity in the ^{188}Pb nucleus – in-beam spectroscopy employing the SAGE spectrometer

Janne Pakarinen[1,*], Philippos Papadakis[1,2], Daniel M Cox[1,2,], Kalle Auranen[1], Tuomas Grahn[1], Paul Greenlees[1], Katarzyna Hadynska-Klek[3], Andrej Herzáň[1], Rolf-Dietmar Herzberg[2], Ulrika Jakobsson[1], Rauno Julin[1], Sakari Juutinen[1], Joonas Konki[1], Matti Leino[1], Andrew Mistry[2], David O'Donnell[2], Jari Partanen[1], Pauli Peura[1], Panu Rahkila[1], Panu Ruotsalainen[1], Mikael Sandzelius[1], Jan Sarén[1], Cath Scholey[1], Juha Sorri[1], Sanna Stolze[1], Juha Uusitalo[1] and Katarzyna Wrzosek-Lipska[4]

[1]University of Jyväskylä, Department of Physics, P.O. Box 35, FI-40014 University of Jyväskylä, Finland
[2]Oliver Lodge Laboratory, University of Liverpool, Liverpool L69 7ZE, United Kingdom
[3]Heavy Ion Laboratory, University of Warsaw, PL-020-093 Warsaw, Poland
[4]Katholieke Universiteit Leuven, Instituut voor Kern- en Stralingsfysica, BE-3001 Leuven, Belgium

Abstract

Competing structures in the neutron-deficient ^{188}Pb nucleus have been probed in a simultaneous in-beam γ-ray and conversion-electron experiment employing the SAGE spectrometer in conjunction with the gas-filled separator RITU and the focal-plane spectrometer GREAT. The extracted internal conversion coefficients for the yrast-band transitions confirm their E2 character. The spectra obtained with SAGE are compared to simulated spectra obtained with the SAGE GEANT4 simulation package. This study is part of our experimental programme in investigations of shape coexistence and collectivity in the neutron-deficient Pb isotopes.

INTRODUCTION

The region around the neutron mid-shell nucleus $^{186}Pb_{104}$ provides a fruitful ground for studies of shape coexistence in atomic nuclei [1]. Over the years, a considerable body of experimental evidence for shape-coexisting configurations in the even-mass Pb isotopes has been obtained using various different techniques [2, 3, 4, 5, 6, 7]. When approaching the N=104 mid-shell, these structures intrude down to energies close to the spherical ground state and can be associated with intruder 2p-2h and 4p-4h proton shell-model excitations across the Z=82 energy gap [1, 6, 7]. Calculations using the deformed mean-field approach, essentially equivalent to the shell-model method, reveal three different shapes (spherical, oblate and prolate configurations) [8, 9, 10, 11], suggesting that a subtle rearrangement of only few protons can result in a drastic nuclear shape change [12]. However, it remains a challenge for both theoretical and experimental studies to obtain a consistent and detailed description of all the observed phenomena.

In α-decay studies, a low-lying excited state at $\sim$591 keV in ^{188}Pb has been assigned as a 0^+ state [13, 14, 5]. On the basis of α-decay hindrance factors, it is associated with a π(2p-2h) configuration (oblate). The existence of deformed structures has been confirmed in in-beam γ-ray measurements through the observation of rotational prolate and oblate bands. Moreover, the triple-shape coexistence has been revealed by the existence of three isomeric states associated with different structures (spherical 12^+, oblate 11^- and prolate 8^-) and characteristic band structures on top of these states [15]. In an in-beam conversion-electron spectroscopy measurement, two low-lying 0^+ states were found at 591 keV (oblate) and 725 keV (prolate) [16]. However, there is no consensus regarding the level energies of proposed oblate and prolate bandhead states.

The advent of the SAGE spectrometer has raised the sensitivity of in-beam electron spectroscopy into a new level. The ability to measure cross-coincidences between conversion electrons and γ rays allows some of the remaining open questions in this nucleus to be addressed. Concerning the present experiment, the two main objectives were to:

- measure the conversion electron strengths of the $I_2 \rightarrow I_1$ inter-band transitions
- probe the location and feeding of the low-lying 0^+ states

In this paper, the focus is on confirming the multipole character of the yrast-band transitions and validating the SAGE performance.

*E-mail: janne.pakarinen@jyu.fi

EXPERIMENTAL DETAILS

The experiment was carried out in the Accelerator Laboratory of the University of Jyväskylä, Finland, employing beams from the K130 cyclotron [17]. Data were obtained using the SAGE spectrometer [18] in conjunction with the gas-filled separator RITU [19] and the GREAT focal-plane spectrometer [20]. Prompt γ rays and conversion electrons correlated with recoils were selected in the data analysis. The nuclei of interest were produced via two different reactions, namely ^{108}Pd(^{83}Kr,3n)^{188}Pb and ^{160}Dy(^{32}S,4n)^{188}Pb. The beam currents were limited by the counting rate of the SAGE Si-detector. More parameters related to the reactions used are listed in table 1. The results presented in this paper were obtained using data from the ^{160}Dy(^{32}S,4n)^{188}Pb reaction. The events occurring in detectors were recorded by the triggerless total data readout data acquisition system and time-stamped using a 100 MHz clock [21]. Subsequent temporal and spatial correlations between the various detector groups were performed using the GRAIN data analysis package [22].

Tab. 1: Beam and target properties in the present experiment.

Beam	Target	Target thickness [μg/cm^2]	Beam energy [MeV]	Average beam current [pnA]	Irradiation time [d]
^{83}Kr	^{108}Pd	800	355 and 365	3	1.5
^{32}S	^{160}Dy	500	165	13	5.8

RESULTS

The long half-life and low α-decay branching ratio (25.1 s and 9.3%, respectively [23]), rendered the use of the recoil-decay tagging technique unfeasible. However, the high detection efficiency of SAGE for both γ rays and conversion electrons enabled the collection of sufficient recoil-gated γ-e^- coincidence events to carry out cross-coincidence analysis. This allowed γ rays originating from ^{188}Pb nuclei and nuclei produced via other open fusion-evaporation channels to be distinguished. The two nuclei with highest cross-sections, ^{188}Pb and ^{188}Tl, were produced via the 4n and p3n reaction channels, respectively, at similar levels. In figure 1, recoil-gated singles γ-ray and conversion-electron energy spectra are plotted. In the uppermost spectrum, the most prominent γ-ray transitions have been labelled and associated with the nucleus of origin. In the conversion-electron energy spectrum (bottom), the transitions associated with ^{188}Tl (M1) are more pronounced over transitions associated with ^{188}Pb (E2) due to their higher internal conversion coefficients.

In figure 2, recoil-gated γ-ray and conversion-electron energy spectra in coincidence with the 434 keV γ ray stemming from the $8^+ \rightarrow 6^+$ transition are plotted. This γ-ray transition provided clean conditions needed for extraction of the internal conversion coefficient for the yrast-band transitions within the same cascade. In addition, a partial level scheme of ^{188}Pb is shown in figure 2 to help interpret the energy spectra.

The peak areas of the spectra shown in figure 2 were measured and corrected for efficiency using absolute efficiency curves extracted from radioactive calibration source data. The resulting values were used to calculate the internal conversion coefficients summarized in table 2. No angular distribution correction or other adjustments were used in the analysis. The results obtained employing this method are compared with values calculated using the BrIcc conversion coefficient calculator [24] for M1 and E2 transitions. The E2 character of the $4^+ \rightarrow 2^+$ and $6^+ \rightarrow 4^+$ transitions of 340 keV and 370 keV, respectively, was confirmed.

Tab. 2: Comparison of the conversion coefficients obtained for the yrast-band transitions in ^{188}Pb with the BrIcc database values.

	340keV			370keV		
Source	α_K	α_L	$\alpha_{K/L}$	α_K	α_L	$\alpha_{K/L}$
M1 (BrIcc)	0.248(4)	0.0422(6)	5.87(12)	0.198(3)	0.0336(5)	5.89(12)
E2 (BrIcc)	0.0486(7)	0.0237(4)	2.05(4)	0.0402(6)	0.0176(3)	2.28(5)
SAGE	0.052(4)	0.025(2)	2.08(22)	0.043(3)	0.018(3)	2.44(39)

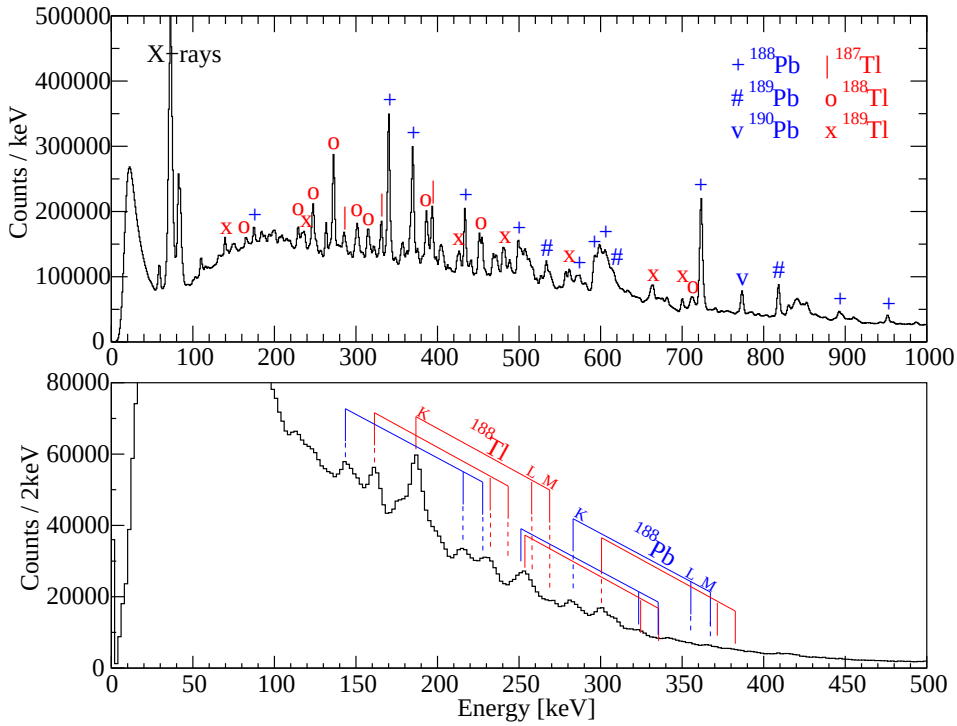

Fig. 1: Recoil-gated, γ-ray (top) and conversion-electron (bottom) energy spectra obtained with SAGE. The most prominent transitions have been labelled according to their parent nucleus. The conversion-electron lines have been marked according to the orbital of origin.

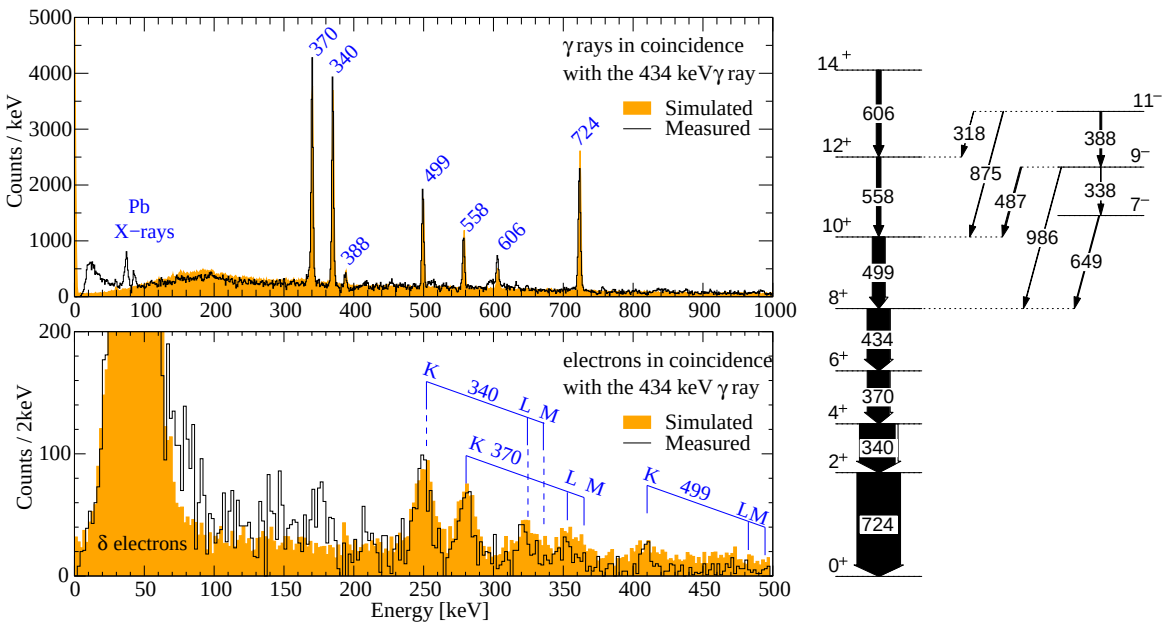

Fig. 2: Recoil-gated, γ-ray and conversion-electron energy spectra in coincidence with the 434 keV γ ray measured with SAGE. The most prominent transitions can be associated with ^{188}Pb nuclei and have been labelled. The conversion-electron lines have been marked according to the orbital of origin. On the right, partial level scheme of ^{188}Pb is shown [15]. The simulated γ-ray and conversion-electron spectra in coincidence with the 434 keV γ ray are shown in orange for comparison with measured spectra.

SIMULATIONS

The decay of excited states and subsequent detection of γ rays and conversion electrons can be modelled using the SAGE GEANT4 simulation package [25]. The simulation allow the veracity of the level scheme and the accuracy of the extracted intensities to be tested. The input parameters include the level energies, transition energies and multipolarities, and the γ-ray intensities. According to this input, conversion coefficients were calculated using the BrIcc conversion coefficient calculator allowing the total transition intensity to be inferred. In the present work, the decay of the excited states in ^{188}Tl and ^{188}Pb was simulated to match the measured data set.

As with measured data it was possible to perform γ-e^- coincidence analysis on the simulated data. Comparisons between simulated and measured γ-ray and conversion-electron energy spectra are shown in figure 2. In both cases these spectra require a coincidence with the 434 keV γ ray stemming from the $8^+ \rightarrow 6^+$ transition. It can be seen that there is close agreement between the measured and simulated data. The background was extracted from the measured spectra using the fitting program TV [26] using polynomial fits along with a gaussian curve in the case of the δ electrons and was added to simulated spectra.

SUMMARY

The excited states in the very neutron-deficient nucleus ^{188}Pb have been measured in a combined in-beam γ-ray and conversion-electron experiment employing the SAGE spectrometer. This paper carries two main messages. Firstly, the internal conversion coefficients of the $6^+ \rightarrow 4^+$ and $4^+ \rightarrow 2^+$ yrast-band transitions in ^{188}Pb have been measured and confirm the earlier E2 electromagnetic multipole assignment. Secondly, these results were obtained through direct comparison of observed γ rays and conversion electrons for given transitions using the absolute detection efficiencies of SAGE. Strong support for the interpretation of data was obtained through the GEANT4 simulations.

The results presented here provide an important step towards the complete analysis of the ^{188}Pb SAGE data set. It has been shown that the internal conversion coefficients can be extracted without normalizing to a known transition, but using absolute detection efficiencies. The work is part of our physics programme in studies of shapes and collectivity in the neutron-deficient Pb region and complements our Coulomb excitation measurements. Another complementary experiment will be performed at HIE-ISOLDE employing the MINIBALL spectrometer [27] in conjunction with the recently developed SPEDE electron spectrometer [28].

ACKNOWLEDGMENTS

This work has been supported by the Academy of Finland under the Finnish Centre of Excellence Programme 2012–2017 (Nuclear and Accelerator Based Physics Programme at JYFL and Contract No. 257562) and by the ENSAR project (Contract No. 262010) and Marie Curie Career Integration Grant (Contract No. 304033) of the EU 7th Framework Programme. The GAMMAPOOL European Spectroscopy Resource is greatly acknowledged for the loan of germanium detectors for JUROGAM.

REFERENCES

[1] K. Heyde and J.L. Wood, Rev. Mod. Phys. **83**, 1467 (2011).
[2] H. De Witte et al., Phys. Rev. Lett. **98**, 112502 (2007).
[3] P. Van Duppen et al., Phys. Rev. Lett. **52**, 1974 (1984).
[4] P. Van Duppen et al., J. Phys. G: Nucl. Part. Phys. **16**, 441 (1990).
[5] A.N. Andreyev et al., J. Phys. G: Nucl. Part. Phys. **25**, 835 (1999).
[6] R. Julin, K. Helariutta, M. Muikku, J. Phys. G: Nucl. Part. Phys. **27**, R109 (2001).
[7] R. Julin, T. Grahn, J. Pakarinen and P. Rahkila, J. Phys. G: Nucl. Part. Phys. **43**, 024004 (2016).
[8] N. Tajima, H. Flocard, P. Bonche, J. Dobaczewski, and P.-H. Heenen, Nucl. Phys. A **551**, 409 (1993).
[9] T. Duguet, M. Bender, P. Bonche, and P.-H. Heenen, Phys. Lett. B **559**, 201 (2003).
[10] M. Bender, P. Bonche, T. Duguet, and P.-H. Heenen, Phys. Rev. C **69**, 064303 (2004).
[11] R.R. Rodríguez-Guzmán, J.L. Egido, and L.M. Robledo, Phys. Rev. C **69**, 054319 (2004).
[12] A.N. Andreyev et al., Nature **405**, 430 (2000).
[13] N. Bijnens et al., Z. Phys. A **356**, 3 (1996).
[14] R.G. Allatt et al., Phys. Lett. B **437**, 29 (1998).
[15] G.D. Dracoulis et al., Phys. Rev. C **69**, 054318 (2004).
[16] Y. Le Coz et al., EPJ direct **1**, A3, (1999).
[17] P. Heikkinen and E. Liukkonen, in Cyclotrons and Their Applications: Proceedings of the 14th International Conference, Cape Town, South Africa 8–13 October 1995, edited by J. C. Cornell (World Scientific,

Singapore, 1996).
[18] J. Pakarinen et al., Eur. Phys. J. A **50**, 53 (2014).
[19] M. Leino et al., Nucl. Instrum. Methods B **99**, 653 (1995).
[20] R.D. Page et al., Nucl. Instrum. Methods B **204**, 634 (2003).
[21] I. Lazarus et al., IEEE Trans. Nucl. Sci. **48**, 567 (2001).
[22] P. Rahkila, Nucl. Instrum. Methods A **595**, 637 (2008).
[23] J. Wauters et al., Z. Phys. A **345**, 21 (1993).
[24] T. Kibédi et al., Nucl. Instrum. Methods A **589**, 202 (2008).
[25] D.M. Cox et al., Eur. Phys. J. A **51**, 64 (2015).
[26] J. Theuerkauf et al., Institute for Nuclear Physics, Cologne (1993).
[27] N. Warr et al., Eur. Phys. J. A **49**, 40 (2013).
[28] P. Papadakis et al., JPS Conf. Proc. **6**, 030023 (2015).

The transitional structure of ^{132,134}Xe from inelastic neutron scattering

E. E. Peters[1*], T. J. Ross[1,2], A. Chakraborty[1,2], B. P. Crider[2], A. Kumar[1,2], M. T. McEllistrem[2], F. M. Prados-Estévez[1,2], S. W. Yates[1,2]

[1]Department of Chemistry, University of Kentucky, 505 Rose St., Lexington, KY 40506 USA
[2]Department of Physics & Astronomy, University of Kentucky, 505 Rose St., Lexington, KY 40506 USA

Abstract

The xenon isotopes are of interest for various structural reasons: candidates for the quadrupole mixed-symmetry states have been proposed, the stable isotopes span a transitional region within which a critical-point nucleus may exist, and some of the isotopes have implications for neutrinoless double-beta decay. With opportunities to gain new information, ^{132}Xe and ^{134}Xe were investigated using inelastic neutron scattering at the University of Kentucky Accelerator Laboratory. Highly enriched (> 99.9%) ^{132}Xe and ^{134}Xe gases were converted to solid $^{132}XeF_2$ and $^{134}XeF_2$ and were used as scattering samples. Angular distribution and excitation function data were obtained for levels up to 3.5 MeV in excitation energy for J $\leq$ 6. Level lifetimes were obtained using the Doppler-shift attenuation method, allowing the determination of reduced transition probabilities, and new excited 0^+ states were identified in both nuclei. New data of relevance to the aforementioned three subjects of interest were obtained.

Introduction

The stable isotopes of xenon, in particular ^{132}Xe and ^{134}Xe, are of interest for various reasons. First, candidates for 2^+ mixed-symmetry states have been proposed in both isotopes. Second, the stable isotopes of xenon span a region of transitional nuclear structure, where ^{136}Xe at a closed neutron shell is considered spherical in shape, while the light isotopes are more deformed and considered to be gamma-soft rotors. One potential interpretation is that a critical-point nucleus exists for the shape transition, and studying these isotopes can lend insight into the nature of this transition and determine whether such a nucleus exists. Finally, ^{134}Xe is of interest for neutrinoless double-beta decay experiments, as it is a component in several of the detectors employed in the search for this yet-to-be-observed process and could create additional backgrounds in the region of interest.

The second version of the interacting boson model (IBM) [1], the IBM-2, creates a distinction between proton and neutron bosons [2]. In doing so, two types of states emerge, full-symmetry states (FSSs) and mixed-symmetry states (MSSs). FSSs are fully symmetric with respect to interchange of an arbitrary pair of proton and neutron bosons, and correspond to the states of the IBM-1 where no distinction is made between proton and neutron bosons. MSSs possess at least one pair of proton and neutron bosons that are antisymmetric with respect to interchange of the bosons. Such states, therefore, provide information on the effective proton-neutron interactions in play. A review of the experimental evidence for MSSs was published by Pietralla *et al.* [3]. The signature for a MSS in a weakly deformed nucleus is an off-yrast 2^+ state around 2 MeV with a strong $M1$ decay to the 2_1^+ state [$B(M1; 2_{MS}^+ \rightarrow 2_1^+) \sim 1\mu_n^2$] and a weakly collective $E2$ decay to the ground state [$B(E2; 2_{MS}^+ \rightarrow 0_1^+) \sim$ few W.u.] [3]. MSSs have now been observed in many regions of the nuclear chart. Candidates for states in ^{132}Xe and ^{134}Xe have been proposed from Coulomb excitation measurements [4, 5, 6].

Isotopic chains typically exhibit a transition in structure with changing neutron number. For example, the stable xenon isotopes appear spherical in nature at the closed neutron shell (N = 82), while the lighter mass isotopes are more gamma-soft in character. It is not well understood how this transition occurs. One proposed description in terms of the symmetries of the IBM, is that a critical-point symmetry, E(5), exists in the transition between the U(5) and O(6) symmetries. Candidacy for the E(5) symmetry has been based on the allowed decays of the excited 0^+ states, *i.e.*, the 0_2^+ decays only to the 2_1^+ with a B(E2) relative to that for the $2_1^+ \rightarrow 0_1^+$ of 0.86 and the 0_3^+ decays only to the 2_2^+ with a relative B(E2) value of 2.21. Clark, et al. [7] proposed ^{128}Xe as a possible E(5) candidate, but Coulomb excitation measurements by Coquard, et al. [8] showed that the decays of the excited 0^+ states were not consistent with those allowed in the E(5) symmetry, and it was concluded that ^{128}Xe does not embody the E(5) critical-point symmetry. The excited 0^+ states in ^{132}Xe and ^{134}Xe were not known at the time ^{128}Xe was proposed; if these states and their decays could be identified, the possibility of these isotopes as E(5) nuclei could be evaluated.

*E-mail: fe.peters@uky.edu

The search for neutrinoless double-beta decay ($0\nu\beta\beta$) is currently the focus of significant effort. This process is of interest because the observation of $0\nu\beta\beta$ would provide the mass of the neutrino and establish whether neutrinos are Majorana particles (their own antiparticles). One such search involves the decay of ^{136}Xe to ^{136}Ba; the $2\nu\beta\beta$ decay has been observed [9]. As such decays are extremely rare, if they occur at all, large-scale experiments are designed for their observation. The EXO-200 (Enriched Xenon Observatory) experiment is composed of 200 kg of liquid xenon enriched to 80.6% ^{136}Xe with the remaining 19.4% being ^{134}Xe [10]. The liquid xenon itself serves as a scintillation fluid and the detector is also designed to act as an ionization chamber. While EXO-200 is located deep underground at WIPP (the Waste Isolation Pilot Plant) near Carlsbad, New Mexico, and a muon veto has been incorporated in order to reduce backgrounds, not all background events can be eliminated. Neutron-induced background γ rays may arise due to muon-produced neutrons or from natural radioactivity present in the surroundings. It is therefore important to understand these backgrounds in the region of the $0\nu\beta\beta$ signal to prevent a false observation. In the case of ^{136}Xe, the end-point energy is 2457.8 keV. Any transitions in either ^{136}Xe or ^{134}Xe creating γ rays in this region could complicate the unambiguous identification of neutrinoless double-beta decay. The resolution of the detector is also of relevance; the FWHM of a peak in this region is quoted to be $\sim$100 keV [10].

Experiments

Inelastic neutron scattering (INS) experiments were carried out at the University of Kentucky Accelerator Laboratory (UKAL). A 7-MV Van de Graaff accelerator was used to produce proton beams which were pulsed at a rate of 1.875 MHz and were approximately 1 ns in width. Nearly monoenergetic neutrons were created by reaction of the accelerated protons with tritium gas. About 1 atm of tritium gas was contained within a 1 cm in diameter by 3 cm in length tantalum-lined stainless steel cell separated from the beam line by a 3-μm Mo foil. A single HPGe detector of approximately 50% relative efficiency, which was surrounded by an annular BGO for Compton suppression, was used to detect the emitted γ rays. Scattering samples of the two xenon isotopes were approximately 10 g of each highly enriched ($>$ 99.9%) difluoride contained in polytetrafluoroethylene vials.

Excitation functions were measured for ^{132}Xe for incident neutron energies of 1.8 – 3.4 MeV ^{132}Xe and for energies of 2.0 – 3.5 MeV for ^{134}Xe. From these data, thresholds for new γ rays were determined, which aided in placing them in the level scheme. Comparisons of the data with statistical model calculations from the code CINDY were also made and assisted in the determination of the spins of new levels. Angular distribution measurements were made for each isotope at neutron energies of 2.2 and 2.7 MeV, and for ^{132}Xe at 3.4 MeV and for ^{134}Xe at 3.5 MeV. From these data, more information concerning the spins of the new levels was obtained and multipole mixing ratios were extracted upon comparison of the angular distribution coefficients, a_2 and a_4, with statistical model calculations. Also, level lifetimes in the femtosecond regime were obtained using the Doppler-shift attenuation method [11, 12]. With this combined information, reduced transition probabilities were calculated. In some cases, only limits on the level lifetimes could be obtained, resulting in upper limits on the reduced transition probabilities.

Results

Mixed-symmetry States

For ^{132}Xe, the 1985.7-keV level was first proposed as the 2^+ mixed-symmetry state by Hamada *et al.* [13] and this assignment was recently reaffirmed [4]. While the $B(M1)$ value determined from INS is larger, it is within twice the uncertainty of the value quoted in Ref. [4]. The results disagree in part due to the difference in the mixing ratio used in the calculation. The value presented in Tab. 1 is smaller than that given in Ref. [4], which was taken from the NDS [14], and was measured by directional correlations following thermal neutron capture [13]. The large $B(M1)$ value for the transition to the 2_1^+ state, as well as the small $B(E2)$ value for the transition to the ground state, is consistent with the assignment of this level as the mixed-symmetry state.

For ^{134}Xe, the 1948.1-keV level was proposed as the 2^+ mixed-symmetry state by Ahn *et al.* [5] based on results from Coulomb excitation. The measured $B(M1)$ value presented in Tab. 1 is nearly in agreement with that presented in Ref. [5], and is consistent with the characteristics of a mixed-symmetry state. The $B(E2)$ to the ground state is also small and consistent with a mixed-symmetry assignment.

Tab. 1: Comparison of the information obtained for the previously proposed mixed-symmetry states from Coulomb excitation measurements [4, 5] with the data from the present measurements (in bold).

E_{level} (keV)	E_γ (keV)	$J_i^\pi \rightarrow J_f^\pi$	B.R.	τ (fs)	δ	B(E2) (W.u.)	B(M1) (μ_N^2)
^{132}Xe							
1985.66(2)	**1317.94(1)**	$\mathbf{2_3^+ \rightarrow 2_1^+}$	**0.90(1)**	**63(4)**	$\mathbf{-0.041^{+25}_{-38}}$	$\mathbf{0.12^{+15}_{-12}}$	**0.351(27)**
					2.6(2)	**63(5)**	**0.043(7)**
	From Ref. [4]				-0.16(5)	1.14(73)	0.22(6)
	1985.69(3)	$\mathbf{2_3^+ \rightarrow 0_1^+}$	**0.10(1)**			**1.05(12)**	
	From Ref. [4]					0.37(18)	
^{134}Xe							
1947.16(2)	**1100.08(1)**	$\mathbf{2_3^+ \rightarrow 2_1^+}$	**0.88(1)**	$\mathbf{100^{+14}_{-12}}$	$\mathbf{0.044^{+82}_{-75}}$	$\mathbf{0.2^{+8}_{-2}}$	**0.39(5)**
					$\mathbf{2.12^{+53}_{-36}}$	$\mathbf{90^{+14}_{-15}}$	**0.068(30)**
	From Ref. [5, 6]			124(7)	0.08(2)	0.56(4)	0.30(2)
	1947.20(4)	$\mathbf{2_3^+ \rightarrow 0_1^+}$	**0.12(1)**			$\mathbf{0.86^{+12}_{-14}}$	
	From Ref. [5, 6]					0.72(7)	

The E(5) Critical-point Symmetry

New excited 0^+ states were identified in this work in both ^{132}Xe and ^{134}Xe. Comparison of the theoretical E(5) decays of these states and the experimentally observed decays are shown in Figs. 1 and 2. In neither case does the E(5) theoretical depiction accurately describe the experimental findings. The second and third excited 0^+ states both decay only to the 2_1^+ state, which for the 0_3^+ state is not an allowed decay in the E(5) description. As the decays of these excited 0^+ states have previously been used as a signature of an E(5) nucleus, and lack of the allowed decays has been used as conclusive evidence against E(5) behavior [8], it can be concluded that neither ^{132}Xe nor ^{134}Xe is an example of an E(5) nucleus.

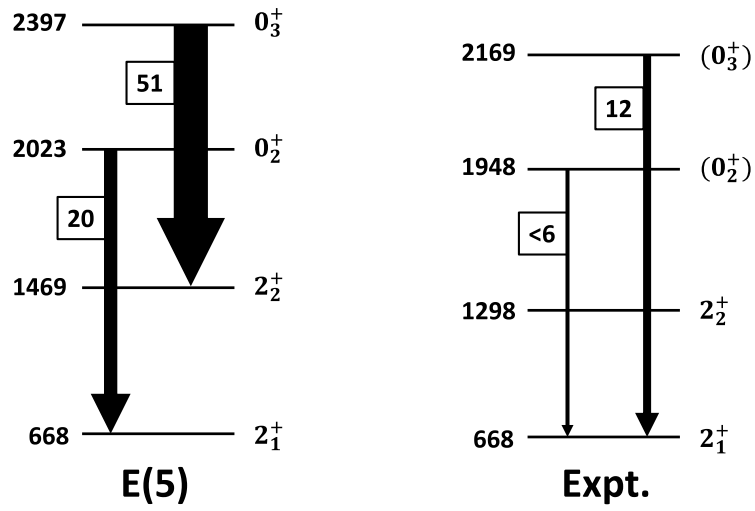

Fig. 1: Comparison of the E(5) theoretical decays (left) of the excited 0^+ states with the experimentally observed decays (right) for ^{132}Xe. The values in boxes are the B(E2)s in W.u.

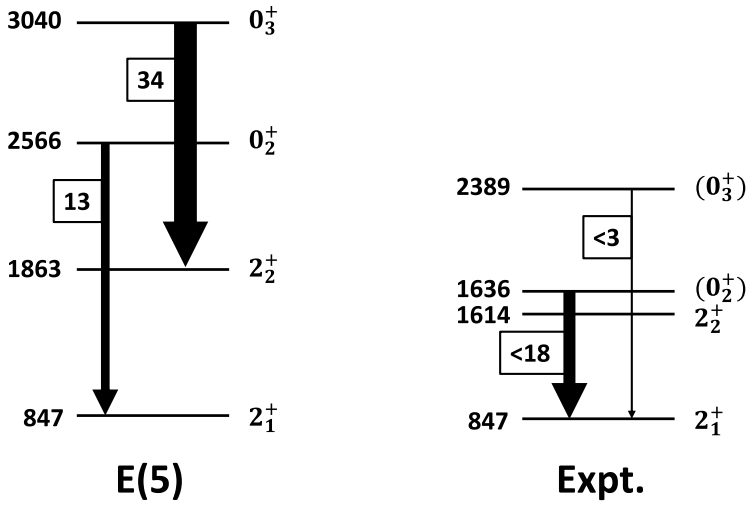

Fig. 2: Comparison of the E(5) theoretical decays (left) of the excited 0^+ states with the experimentally observed decays (right) for ^{134}Xe. The values in boxes are the B(E2)s in W.u.

Possible Interference for the Observation of Neutrinoless Double-Beta Decay of ^{136}Xe

The experimental signature for $0\nu\beta\beta$ is a single peak at the Q-value for the decay, which for ^{136}Xe is 2457.8 keV. As discussed previously, ^{134}Xe may be present in amounts as much as 20% of the liquid xenon in the detector, and thus γ rays near this energy arising from ^{134}Xe are also of relevance. In the present experiments for ^{134}Xe, a new ground-state γ ray from a new level at 2485.7 keV was observed. Well within the resolution of the EXO-200 detector, this γ ray will significantly overlap with the potential $0\nu\beta\beta$ signal, as shown in Fig. 3. As this is the case, a measurement of the cross section for the production of this γ ray would be valuable information, allowing the calculation of the number of expected events from neutron scattering backgrounds. Experiments to obtain the cross section have been completed and will be published elsewhere.

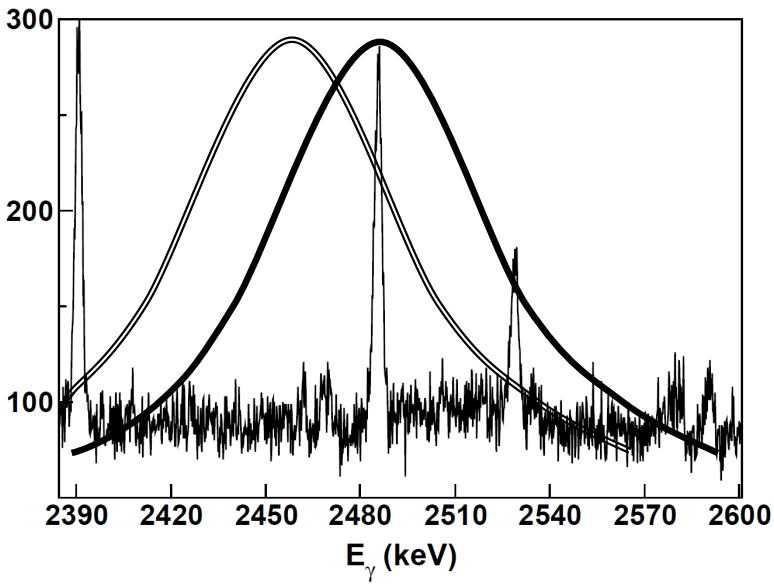

Fig. 3: The 2485.7-keV γ ray in ^{134}Xe as shown in the spectrum obtained at $E_n = 2.7$ MeV. The solid curve demonstrates a schematic representation of the γ ray at the resolution quoted by the EXO collaboration and the outlined curve is a representation of the signal that would be created by a 2457.8-keV $0\nu\beta\beta$ event.

Conclusions

Results for three areas of interest in the nuclear structure of ^{132}Xe and ^{134}Xe have been presented. First, the current data are in agreement with the previously assigned mixed-symmetry states. Second, the first and second excited 0^+ states were identified in both isotopes and their decays were compared with those predicted by the E(5) critical-point symmetry. Based on the absence of the allowed decays of these states, neither ^{132}Xe nor ^{134}Xe embodies an E(5) nucleus. Finally, a new state in ^{134}Xe with a ground-state transition near in energy to the signature for the $0\nu\beta\beta$ of ^{136}Xe has been identified that will create additional backgrounds in the region of interest for experiments which employ detector materials containing ^{134}Xe. These findings are initial results from the $(n, n'\gamma)$ measurements and more details concerning the structure of these nuclei are forthcoming.

ACKNOWLEDGMENT:
This material is based upon work supported by the U. S. National Science Foundation under Grant No. PHY-1305801. The authors wish to thank H. E. Baber for his assistance in maintaining the UKAL.

REFERENCES

[1] H. Feshbach and F. Iachello, Ann. Phys. (NY) **84**, 211 (1974).
[2] A. Arima, T. Ohtsuka, F. Iachello, and I. Talmi, Phys. Lett. B **66**, 205 (1977).
[3] N. Pietralla, P. von Brentano, and A.F. Lisetskiy, Prog. Part. Nucl. Phys. **60**, 225 (2008).
[4] L. Coquard, N. Pietralla, G. Rainovski, T. Ahn, L. Bettermann, M.P. Carpenter, R.V.F. Janssens, J. Leske, C.J. Lister, O. Möller, W. Rother, V. Werner, and S. Zhu, Phys. Rev. C **82**, 024317 (2010).
[5] T. Ahn, L. Coquard, N. Pietralla, G. Rainovski, A. Costin, R.V.F. Janssens, C.J. Lister, M. Carpenter, S. Zhu, and K. Heyde, Phys. Lett. B **679**, 19 (2009).
[6] T. Ahn, L. Coquard, N. Pietralla, G. Rainovski, A. Costin, R.V.F. Janssens, C.J. Lister, M. Carpenter, S. Zhu, and K. Heyde, Phys. Lett. B **682**, 490 (2010).
[7] R.M. Clark, M. Cromaz, M.A. Deleplanque, M. Descovich, R.M. Diamond, P. Fallon, I.Y. Lee, A.O. Macchiavelli, H. Mahmud, E. Rodriguez-Vieitez, F.S. Stephens, and D. Ward, Phys. Rev. C **69**, 064322 (2004).
[8] L. Coquard, N. Pietralla, T. Ahn, G. Rainovski, L. Bettermann, M.P. Carpenter, R.V.F. Janssens, J. Leske, C. J. Lister, O. Möller, W. Rother, V. Werner, and S. Zhu, Phys. Rev. C **80**, 061304 (2009).
[9] N. Ackerman, et al., Phys. Rev. Lett. **107**, 212501 (2011).
[10] M. Auger, et al., Phys. Rev. Lett. **109**, 032505 (2012).
[11] T. Belgya, G. Molnár, and S.W. Yates, Nucl. Phys. A **607**, 43 (1996).
[12] E.E. Peters, A. Chakraborty, B.P. Crider, B.H. Davis, M.K. Gnanamani, M.T. McEllistrem, F.M. Prados-Estévez, J.R. Vanhoy, and S.W. Yates, Phys. Rev. C **88**, 024317 (2013).
[13] S.A. Hamada, W.D. Hamilton, and B. More, J. Phys. G: Nucl. Phys. **14**, 1237 (1988).
[14] Yu. Khazov, A.A. Rodionov, S. Sakharov, and B. Singh, Nucl. Data Sheets **104**, 497 (2005).

Skyrme RPA for spherical and axially symmetric nuclei

Anton Repko[1,*], Jan Kvasil[1,†], V.O. Nesterenko[2] and P.-G. Reinhard[3]

[1]Institute of Particle and Nuclear Physics, Charles University, V Holešovičkách 2, 180 00 Prague 8, Czech Republic
[2]Joint Institute for Nuclear Research, Dubna, Moscow region 141980, Russia
[3]Institut für Theoretische Physik II, Universität Erlangen, D-91058 Erlangen, Germany

Abstract

Random Phase Approximation (RPA) is the basic method for calculation of excited states of nuclei over the Hartree-Fock ground state, suitable also for energy density functionals (EDF or DFT). We developed a convenient formalism for expressing densities and currents in a form of reduced matrix elements, which allows fast calculation of spectra for spherical nuclei. All terms of Skyrme functional were taken into account, so it is possible to calculate electric, magnetic and vortical/toroidal/compression transitions and strength functions of any multipolarity. Time-odd (spin) terms in Skyrme functional become important for magnetic and isovector toroidal (i.e. second-order term in long-wave expansion of E1) transitions. It was also found that transition currents in pygmy region (low-lying part of E1 resonance) exhibit isoscalar toroidal flow, so the previously assumed picture of neutron-skin vibration is not the only mechanism present in pygmy transitions.

RPA calculations with heavy axially-symmetric nuclei now become feasible on ordinary PC. Detailed formulae for axial Skyrme RPA are given. Some numerical results are shown in comparison with the approximate approach of separable RPA, previously developed in our group for fast calculation of strength functions.

INTRODUCTION

Energy density functional in nuclear physics is a self-consistent microscopic phenomenological approach to calculate nuclear properties and structure over the whole periodic table. The method is analogous to Kohn-Sham density functional theory (DFT) used in electronic systems. Three types of functionals are frequently used nowadays: non-relativistic Skyrme functional [1] with zero-range two-body and density dependent interaction, finite-range Gogny force [2] and relativistic (covariant) mean-field [3]. Typical approach employs Hartree-Fock-Bogoliubov or HF+BCS calculation scheme to obtain ground state and single-(quasi)particle wavefunctions and energies. These results are then utilized to fit the parameters of the functionals, thus obtaining various parametrizations suitable for specific aims, such as: calculation of mass-table, charge radii, fission barriers, spin-orbit splitting and giant resonances.

Random Phase Approximation (RPA) is a textbook standard [4] to calculate one-phonon excitations of the nucleus. Increasing computing power has enabled to employ fully self-consistent residual interaction derived from the same density functional as the underlying ground state. While the spherical nuclei can be treated directly (by matrix diagonalization) [5, 6, 7], axially deformed nuclei still pose certain difficulties due to large matrix dimensions [8]. Our group developed a separable RPA (SRPA) approach [9, 10], which greatly reduces the computational cost by utilizing separable residual interaction, entirely derived from the underlying functional by means of multi-dimensional linear response theory.

Present article gives a convenient formalism for rotationally-invariant treatment of spherical full RPA, and also gives detailed expressions for matrix elements in axial symmetry. Both time-even and time-odd terms of Skyrme functional are employed, so the method is suitable for various electric and magnetic multipolarities. Finally, some results are shown by means of strength functions and transition currents.

Skyrme functional and density operators

Skyrme interaction is defined as

$$\begin{aligned}\hat{V}_{\rm Sk}(\vec{r}_1,\vec{r}_2) = {} & t_0(1+x_0\hat{P}_\sigma)\delta(\vec{r}_1-\vec{r}_2) - \tfrac{1}{8}t_1(1+x_1\hat{P}_\sigma)\big[(\overleftarrow{\nabla}_1-\overleftarrow{\nabla}_2)^2\delta(\vec{r}_1-\vec{r}_2)+\delta(\vec{r}_1-\vec{r}_2)(\overrightarrow{\nabla}_1-\overrightarrow{\nabla}_2)^2\big] \\ & + \tfrac{1}{4}t_2(1+x_2\hat{P}_\sigma)(\overleftarrow{\nabla}_1-\overleftarrow{\nabla}_2)\cdot\delta(\vec{r}_1-\vec{r}_2)(\overrightarrow{\nabla}_1-\overrightarrow{\nabla}_2) + \tfrac{1}{6}t_3(1+x_3\hat{P}_\sigma)\delta(\vec{r}_1-\vec{r}_2)\rho^\alpha\big(\tfrac{\vec{r}_1+\vec{r}_2}{2}\big) \\ & + \tfrac{\rm i}{4}t_4(\vec{\sigma}_1+\vec{\sigma}_2)\cdot\big[(\overleftarrow{\nabla}_1-\overleftarrow{\nabla}_2)\times\delta(\vec{r}_1-\vec{r}_2)(\overrightarrow{\nabla}_1-\overrightarrow{\nabla}_2)\big] \qquad (1)\end{aligned}$$

*E-mail: anton@a-repko.sk
†E-mail: kvasil@ipnp.troja.mff.cuni.cz

with parameters $t_0, t_1, t_2, t_3, t_4, x_0, x_1, x_2, x_3, \alpha$ and a spin-exchange operator $\hat{P}_\sigma = \frac{1}{2}(1 + \vec{\sigma}_1 \cdot \vec{\sigma}_2)$. Since it is a zero-range interaction, the solution of many-body problem by Hartree-Fock method can be equivalently reformulated as a density functional theory [1], where the complete density functional is

$$\begin{aligned}
\mathcal{H}_{\rm Sk} &= \frac{1}{2}\sum_{\alpha\beta}\langle\alpha\beta|\hat{V}_{\rm Sk}|\alpha\beta\rangle - \frac{1}{2}\sum_{q=p,n}\sum_{\alpha\beta\in q}\langle\alpha\beta|\hat{V}_{\rm Sk}|\beta\alpha\rangle \\
&= \int \mathrm{d}^3r\Big\{\frac{b_0}{2}\rho^2 - \frac{b_0'}{2}\sum_q\rho_q^2 + b_1(\rho\tau - \vec{j}^2) - b_1'\sum_q(\rho_q\tau_q - \vec{j}_q^2) + \frac{b_2}{2}(\vec{\nabla}\rho)^2 - \frac{b_2'}{2}\sum_q(\vec{\nabla}\rho_q)^2 \\
&\quad + \tilde{b}_1\Big(\vec{s}\cdot\vec{T} - \sum_{ij}\mathcal{J}_{ij}^2\Big) + \tilde{b}_1'\sum_q\Big(\vec{s}_q\cdot\vec{T}_q - \sum_{ij}\mathcal{J}_{q;ij}^2\Big) + \frac{b_3}{3}\rho^{\alpha+2} - \frac{b_3'}{3}\rho^\alpha\sum_q\rho_q^2 \\
&\quad - b_4\big[\rho\vec{\nabla}\cdot\vec{\mathcal{J}} + \vec{s}\cdot(\vec{\nabla}\times\vec{j})\big] - b_4'\sum_q\big[\rho_q\vec{\nabla}\cdot\vec{\mathcal{J}}_q + \vec{s}_q\cdot(\vec{\nabla}\times\vec{j}_q)\big] \\
&\quad + \frac{\tilde{b}_0}{2}\vec{s}^2 - \frac{\tilde{b}_0'}{2}\sum_q\vec{s}_q^2 + \frac{\tilde{b}_2}{2}\sum_{ij}(\nabla_i s_j)^2 - \frac{\tilde{b}_2'}{2}\sum_q\sum_{ij}(\nabla_i s_j)_q^2 + \frac{\tilde{b}_3}{3}\rho^\alpha\vec{s}^2 - \frac{\tilde{b}_3'}{3}\rho^\alpha\sum_q\vec{s}_q^2\Big\}
\end{aligned} \tag{2}$$

where the last line contains the spin (time-odd) terms, which are usually omitted. However, they have quite important contribution for magnetic excitations [11], as will be illustrated below, so we use them in all calculations. Parameters b_j depend on the parameters t_j, x_j from (1):

$$\begin{aligned}
&b_0 = \tfrac{t_0(2+x_0)}{2}, \quad b_0' = \tfrac{t_0(1+2x_0)}{2}, \quad \tilde{b}_0 = \tfrac{t_0x_0}{2}, \quad \tilde{b}_0' = \tfrac{t_0}{2}, \\
&b_1 = \tfrac{t_1(2+x_1)+t_2(2+x_2)}{8}, \quad b_1' = \tfrac{t_1(1+2x_1)-t_2(1+2x_2)}{8}, \quad \tilde{b}_1 = \tfrac{t_1x_1+t_2x_2}{8}, \quad \tilde{b}_1' = \tfrac{-t_1+t_2}{8}, \\
&b_2 = \tfrac{3t_1(2+x_1)-t_2(2+x_2)}{16}, \quad b_2' = \tfrac{3t_1(1+2x_1)+t_2(1+2x_2)}{16}, \quad \tilde{b}_2 = \tfrac{3t_1x_1-t_2x_2}{16}, \quad \tilde{b}_2' = \tfrac{3t_1+t_2}{16}, \\
&b_3 = \tfrac{t_3(2+x_3)}{8}, \quad b_3' = \tfrac{t_3(1+2x_3)}{8}, \quad \tilde{b}_3 = \tfrac{t_3x_3}{8}, \quad \tilde{b}_3' = \tfrac{t_3}{8}, \quad b_4 = b_4' = \tfrac{t_4}{2}
\end{aligned} \tag{3}$$

Most Skyrme parametrization set explicitly $\tilde{b}_1 = \tilde{b}_1' = 0$ and this fact is denoted as exclusion of the "tensor term". There are also parametrizations fitted with the tensor term included, e.g. SGII [12], SLy7 [13].

The operators corresponding to the densities and currents in (2) are defined as

$$\begin{aligned}
\text{density:}\quad & \hat{\rho}(\vec{r}_0) = \delta(\vec{r}-\vec{r}_0), && \text{kinetic energy:}\quad \hat{\tau}(\vec{r}_0) = \overleftarrow{\nabla}\cdot\delta(\vec{r}-\vec{r}_0)\overrightarrow{\nabla} \\
\text{spin-orbital:}\quad & \hat{\mathcal{J}}_{jk}(\vec{r}_0) = \tfrac{\mathrm{i}}{2}\big[\overleftarrow{\nabla}_j\sigma_k\delta(\vec{r}-\vec{r}_0) - \delta(\vec{r}-\vec{r}_0)\overrightarrow{\nabla}_j\sigma_k\big] \\
\text{vector spin-orbital:}\quad & \hat{\vec{\mathcal{J}}}(\vec{r}_0) = \tfrac{\mathrm{i}}{2}\big[\overleftarrow{\nabla}\times\vec{\sigma}\delta(\vec{r}-\vec{r}_0) - \delta(\vec{r}-\vec{r}_0)\overrightarrow{\nabla}\times\vec{\sigma}\big], && \hat{\mathcal{J}}_i = \textstyle\sum_{ijk}\varepsilon_{ijk}\mathcal{J}_{jk} \\
\text{current:}\quad & \hat{\vec{j}}(\vec{r}_0) = \tfrac{\mathrm{i}}{2}\big[\overleftarrow{\nabla}\delta(\vec{r}-\vec{r}_0) - \delta(\vec{r}-\vec{r}_0)\overrightarrow{\nabla}\big], && \text{spin:}\quad \hat{\vec{s}}(\vec{r}_0) = \vec{\sigma}\delta(\vec{r}-\vec{r}_0) \\
\text{kinetic energy-spin:}\quad & \hat{T}_j(\vec{r}_0) = \overleftarrow{\nabla}\cdot\sigma_j\delta(\vec{r}-\vec{r}_0)\overrightarrow{\nabla}
\end{aligned} \tag{4}$$

and they are understood as single-particle operators in a many-body system. The densities $\rho, \tau, \mathcal{J}$ are time-even and the currents $\vec{j}, \vec{s}, \vec{T}$ are time-odd. Spin-orbital current $\mathcal{J}_{ij}$ and current $\nabla_i s_j$ have two indices, so we will decompose them into scalar, vector and (symmetric) tensor part

$$\sum_{ij}\mathcal{J}_{ij}^2 = \frac{1}{3}\sum_i\mathcal{J}_{ii}^2 + \frac{1}{2}\vec{\mathcal{J}}^2 + \sum_{m=-2}^{2}(-1)^m[\boldsymbol{\mathcal{J}}_t]_m[\boldsymbol{\mathcal{J}}_t]_{-m} = \frac{1}{3}\mathcal{J}_s^2 + \frac{1}{2}\vec{\mathcal{J}}^2 + \boldsymbol{\mathcal{J}}_t^2 \tag{5}$$

The coefficients related to the (non-relativistic) time-reversal symmetry of the operators are defined as

$$|\bar{\alpha}\rangle = (-1)^{l_\alpha+j_\alpha+m_\alpha}|-\alpha\rangle, \quad u_{\alpha\beta}^{(\pm)} = u_\alpha v_\beta \pm v_\alpha u_\beta, \quad \hat{T}^{-1}\hat{A}\hat{T} = \gamma_T^A\hat{A}^\dagger, \quad \gamma_T^A = \begin{cases} +1: & \text{time-even} \\ -1: & \text{time-odd} \end{cases} \tag{6}$$

$$\hat{A} = \frac{1}{2}\sum_{\alpha\beta}u_{\alpha\beta}^{(\gamma_T^A)}\langle\alpha|\hat{A}|\bar{\beta}\rangle(-\hat{\alpha}_\alpha^+\hat{\alpha}_\beta^+ + \gamma_T^A\hat{\alpha}_{\bar{\alpha}}\hat{\alpha}_{\bar{\beta}}) = \frac{1}{2}\sum_{\alpha\beta}u_{\alpha\beta}^{(\gamma_T^A)}\langle\bar{\alpha}|\hat{A}|\beta\rangle(\hat{\alpha}_{\bar{\alpha}}^+\hat{\alpha}_{\bar{\beta}}^+ - \gamma_T^A\hat{\alpha}_\alpha\hat{\alpha}_\beta) \tag{7}$$

where factors u_β, v_β define the Bogoliubov transformation of particles $\hat{a}_\beta^+$ to quasiparticles $\hat{\alpha}_\beta^+$ [4]. Pairing interaction in the particle-particle channel is defined as ($\rho(\vec{r})$ is the nucleon ground-state density)

$$\hat{V}_{\rm pair} = \sum_{q=p,n}\sum_{ij\in q}^{i<j}V_q\delta(\vec{r}_i-\vec{r}_j) \qquad \text{or} \qquad \hat{V}'_{\rm pair} = \sum_{q=p,n}\sum_{ij\in q}^{i<j}V_q\Big(1-\frac{\rho(\vec{r}_i)}{\rho_0}\Big)\delta(\vec{r}_i-\vec{r}_j) \tag{8}$$

with constant parameters V_p, V_n and ρ_0. Contribution to the density functional is then

$$\mathcal{H}_{\rm pair} = \langle {\rm BCS}|\hat{V}_{\rm pair}|{\rm BCS}\rangle = \frac{1}{4}\sum_{q=p,n} V_q \int \kappa_q^2(\vec{r}){\rm d}^3r, \quad \text{optionally with } \times\Big(1-\frac{\rho(\vec{r})}{\rho_0}\Big); \tag{9}$$

and the pairing density with the corresponding operator is

$$\kappa_q(\vec{r}) = \sum_{\beta\in q}^{m_\beta>0} 2f_\beta u_\beta v_\beta \psi^\dagger_{\bar\beta}(\vec{r})\psi_\beta(\vec{r}) \tag{10}$$

$$\hat\kappa(\vec{r}) = \sum_{\beta>0} f_\beta \psi^\dagger_{\bar\beta}(\vec{r})\psi_\beta(\vec{r})\big[2u_\beta v_\beta(1-\hat\alpha^+_\beta\hat\alpha_\beta-\hat\alpha^+_{\bar\beta}\hat\alpha_{\bar\beta})+(u^2_\beta-v^2_\beta)(\hat\alpha^+_\beta\hat\alpha^+_{\bar\beta}+\hat\alpha_{\bar\beta}\hat\alpha_\beta)\big] \tag{11}$$

with energy-cutoff weight f_β [14]. We use monopole pairing, and we involve only diagonal pairs.

RPA formalism in spherical symmetry

Notation of the Clebsch-Gordan coefficients comes from the book of Varshalovich [15]. In the language of spherical tensors, a hermitian operator $\hat{A}$ satisfies

$$\hat{A}^\dagger_m = (-1)^m \hat{A}_{-m}, \tag{12}$$

for example a vector (rank-1) operator:

$$\hat{A}_1 = (-\hat{A}_x - {\rm i}\hat{A}_y)/\sqrt{2}, \quad \hat{A}_0 = \hat{A}_z, \quad \hat{A}_{-1} = (\hat{A}_x - {\rm i}\hat{A}_y)/\sqrt{2}. \tag{13}$$

The position-dependent operators (4), in general denoted as $\hat{\mathbf{J}}_d(\vec{r})$, are as well expressed in terms of quasiparticles (7) and decomposed in a manner reminiscent of Wigner-Eckart theorem

$$\hat{\mathbf{J}}_d(\vec{r}) = \frac{1}{2}\sum_{\alpha\beta LJM} J^{JL}_{d;\alpha\beta}(r)\frac{(-1)^{l_\beta}}{\sqrt{2J+1}} C^{JM}_{j_\alpha m_\alpha j_\beta m_\beta}\mathbf{Y}^{L*}_{JM}(\vartheta,\varphi)(-\hat\alpha^+_\alpha\hat\alpha^+_\beta+\gamma^d_T\hat\alpha_{\bar\alpha}\hat\alpha_{\bar\beta}) \tag{14}$$

where the symbol $\mathbf{Y}^{L*}_{JM}$ in bold font represents the (complex-conjugated) spherical harmonics in its scalar, vector or tensor form (depending on the rank of operator $\hat{\mathbf{J}}_d(\vec{r})$: $s=0$, 1, 2):

$$\mathbf{Y}^L_{JM}(\vartheta,\varphi) = \sum_{m\mu} C^{JM}_{Lms\mu}Y_{Lm}\mathbf{e}_\mu = \sum_m (-1)^m\big[\mathbf{Y}^L_{JM}\big]_m\mathbf{e}_{-m} = (-1)^{J+L+M+s}\mathbf{Y}^{L*}_{J,-M}(\vartheta,\varphi) \tag{15}$$

Expression (14) defines the reduced matrix elements $J^{JL}_{d;\alpha\beta}(r)$, e.g., a standard density matrix element:

$$\rho^L_{\alpha\beta}(r) = u^{(+)}_{\alpha\beta}\sqrt{(2j_\alpha+1)(2l_\alpha+1)(2j_\beta+1)(2l_\beta+1)}\,R_\alpha(r)R_\beta(r)\frac{(-1)^{j_\beta+\frac{1}{2}}}{\sqrt{4\pi}}\begin{Bmatrix} l_\alpha & l_\beta & L\\ j_\beta & j_\alpha & \frac{1}{2}\end{Bmatrix}C^{L0}_{l_\alpha 0 l_\beta 0} \tag{16}$$

and radial wavefunctions are taken from

$$\langle\vec{r}|\alpha\rangle = \psi_\alpha(\vec{r}) = R_\alpha(r)\sum_{\nu,s} C^{j_\alpha,m_\alpha}_{l_\alpha,\nu,\frac{1}{2},s}Y_{l_\alpha,\nu}(\vartheta,\varphi)\,\chi_s \tag{17}$$

with spinors $\chi_{\pm1/2} = \binom{1}{0}$, $\binom{0}{1}$. Remaining reduced matrix elements will be published later.

Excitations of a given multipolarity are treated as the RPA phonons. One-phonon state, $|\nu\rangle$, is created by action of an operator $\hat{C}^+_\nu$ on the RPA ground state $|{\rm RPA}\rangle$, and has an excitation energy $E_\nu = \hbar\omega_\nu$.

$$\hat{C}^+_\nu|{\rm RPA}\rangle = |\nu\rangle, \quad \hat{C}_\nu|{\rm RPA}\rangle = 0 \tag{18}$$

The operator $\hat{C}^+_\nu$ is a two-quasiparticle ($2qp$) operator defined by real coefficients $c^{(\nu\pm)}_{\alpha\beta}$

$$\hat{C}^+_\nu = \frac{1}{2}\sum_{\alpha\beta} C^{\lambda_\nu\mu_\nu}_{j_\alpha m_\alpha j_\beta m_\beta}\Big(c^{(\nu-)}_{\alpha\beta}\hat\alpha^+_\alpha\hat\alpha^+_\beta + c^{(\nu+)}_{\alpha\beta}\hat\alpha_{\bar\alpha}\hat\alpha_{\bar\beta}\Big) \tag{19}$$

and satisfies the RPA equation

$$[\hat{H},\hat{C}^+_\nu]_{2qp} = E_\nu\hat{C}^+_\nu \tag{20}$$

where the index $2qp$ means that we take only the two-quasiparticle portion of the commutator (after normal ordering). Although all commutators should be evaluated in the RPA ground state, it is common to evaluate them in the HF+BCS ground state (i.e., we use quasi-boson approximation), since the contribution of $4qp$ and higher correlations in the ground state is assumed to be low.

Formulae (14) and (19) involve duplicate $2qp$ pairs. To remove them consistently, we will rescale diagonal pairing factors

$$\frac{1}{2}\sum_{\alpha\beta} \mapsto \sum_{\alpha\geq\beta}, \quad u^{(+)}_{\alpha\alpha} = \sqrt{2}\,u_\alpha v_\alpha \quad \text{(instead of } 2u_\alpha v_\alpha) \tag{21}$$

and $c^{(\nu\pm)}_{\alpha\alpha}$ will be rescaled automatically. Diagonal matrix elements contribute only to electric transitions with λ even.

The hamiltonian is taken as a sum of mean-field part (HF+BCS) and the second functional derivative of Skyrme density functional (+ Coulomb and pairing interaction).

$$\hat{H} = \hat{H}_0 + \hat{V}_{\rm res} = \sum_\gamma \varepsilon_\gamma \hat{\alpha}^+_\gamma \hat{\alpha}_\gamma + \frac{1}{2}\sum_{dd'} \iint \mathrm{d}^3r_1\,\mathrm{d}^3r_2 \frac{\delta^2\mathcal{H}}{\delta J_d(\vec{r}_1)\delta J_{d'}(\vec{r}_2)} :\hat{J}_d(\vec{r}_1)\hat{J}_{d'}(\vec{r}_2): \tag{22}$$

RPA equation (20) then turns into a matrix equation

$$\begin{pmatrix} A & B \\ B & A \end{pmatrix}\begin{pmatrix} c^{(\nu-)} \\ c^{(\nu+)} \end{pmatrix} = \begin{pmatrix} E_\nu & 0 \\ 0 & -E_\nu \end{pmatrix}\begin{pmatrix} c^{(\nu-)} \\ c^{(\nu+)} \end{pmatrix} \tag{23}$$

which can be recast into half-dimensional symmetric-matrix eigenvalue problem [4]. Matrices A and B are

$$A_{pp'} = \delta_{pp'}\varepsilon_p + \sum_{dd'L} \frac{(-1)^{l_\beta+l_\delta}}{2\lambda+1} \int_0^\infty \frac{\delta^2\mathcal{H}}{\delta J_d \delta J_{d'}} J^{\lambda L}_{d;p}(r) J^{\lambda L*}_{d';p'}(r) r^2\mathrm{d}r \tag{24a}$$

$$B_{pp'} = \sum_{dd'L} \gamma^d_T \frac{(-1)^{l_\beta+l_\delta}}{2\lambda+1} \int_0^\infty \frac{\delta^2\mathcal{H}}{\delta J_d \delta J_{d'}} J^{\lambda L}_{d;p}(r) J^{\lambda L*}_{d';p'}(r) r^2\mathrm{d}r, \qquad (p\equiv\alpha\beta,\ p'\equiv\gamma\delta) \tag{24b}$$

The expression $\frac{\delta^2\mathcal{H}}{\delta J_d \delta J_{d'}}$ is symbolical, and includes the integration of the delta function, yielding $\vec{r}_1 = \vec{r}_2$. The exchange Coulomb interaction can be treated by Slater approximation as a density functional

$$\mathcal{H}_{\rm xc} = -\frac{3}{4}\left(\frac{3}{\pi}\right)^{1/3} \frac{e^2}{4\pi\epsilon_0} \int \mathrm{d}^3r \rho_p^{4/3}(\vec{r}) \tag{25}$$

however, the direct Coulomb interaction gives rise to a double integral instead

$$\sum_L \int_0^\infty \frac{\delta^2\mathcal{H}}{\delta J_d \delta J_{d'}} J^{\lambda L*}_{d;\alpha\beta}(r) J^{\lambda L}_{d';\gamma\delta}(r) r^2\mathrm{d}r \quad \mapsto$$

$$\frac{e^2}{4\pi\epsilon_0}\frac{4\pi}{2\lambda+1} \int_0^\infty r^2\mathrm{d}r \int_0^\infty r'^2\mathrm{d}r' \rho^\lambda_{\alpha\beta}(r)\rho^\lambda_{\gamma\delta}(r') \times \begin{cases} r^\lambda/r'^{\lambda+1} & (r<r') \\ r'^\lambda/r^{\lambda+1} & (r\geq r') \end{cases} \tag{26}$$

After calculation of the RPA states, yielding E_ν and $c^{(\nu\pm)}_{\alpha\beta}$, we are interested in the matrix elements of electric and magnetic transition operators and in the transition densities and currents.

$$\langle\nu|\hat{M}_{\lambda\mu}|\mathrm{RPA}\rangle = \langle[\hat{C}_\nu, \hat{M}_{\lambda\mu}]\rangle = \sum_{\alpha\geq\beta} \frac{(-1)^{l_\beta+1}}{\sqrt{2\lambda+1}} M_{\lambda;\alpha\beta}\left(c^{(\nu-)}_{\alpha\beta} + \gamma^M_T c^{(\nu+)}_{\alpha\beta}\right)^* \tag{27}$$

$$\delta\rho_{q;\nu}(\vec{r}) = \langle[\hat{C}_\nu, \hat{\rho}_q(\vec{r})]\rangle = \sum_{\alpha\geq\beta} \frac{(-1)^{l_\beta+1}}{\sqrt{2\lambda+1}} \rho^\lambda_{q;\alpha\beta}(r)\left(c^{(\nu-)}_{\alpha\beta} + c^{(\nu+)}_{\alpha\beta}\right)^* Y^*_{\lambda\mu}(\vartheta,\varphi) \tag{28}$$

$$\delta\vec{j}_{q;\nu}(\vec{r}) = \langle[\hat{C}_\nu, \hat{\vec{j}}_q(\vec{r})]\rangle = \sum_L \sum_{\alpha\geq\beta} \frac{(-1)^{l_\beta+1}}{\sqrt{2\lambda+1}} j^{\lambda L}_{q;\alpha\beta}(r)\left(c^{(\nu-)}_{\alpha\beta} - c^{(\nu+)}_{\alpha\beta}\right)^* \vec{Y}^{L*}_{\lambda\mu}(\vartheta,\varphi) \tag{29}$$

Besides electric ($\gamma^{\mathrm{E}\lambda}_T = 1$) and magnetic ($\gamma^{\mathrm{M}\lambda}_T = -1$) operators in long-wave approximation, we implement also electric vortical, toroidal and compression operators [16] (toroidal operator constitutes the next-order term in long-wave expansion of the exact electric transition operator)

$$\hat{M}^{\mathrm{E}}_{\lambda\nu} = \sum_i \hat{M}^{\mathrm{E}}_{\lambda\mu}(\vec{r}_i) = e\sum_{q=p,n} z_q \sum_{i\in q} \Big(r^\lambda Y_{\lambda\mu}(\vartheta,\varphi)\Big)_i \tag{30a}$$

$$\hat{M}^{\mathrm{M}}_{\lambda\nu} = \frac{\mu_N}{c}\sqrt{\lambda(2\lambda+1)} \sum_{q=p,n}\sum_{i\in q} \left(\left[\frac{g_{s,q}}{2}\vec{\sigma} + \frac{2g_{l,q}}{\lambda+1}\hat{\vec{L}}\right] r^{\lambda-1}\vec{Y}^{\lambda-1}_{\lambda\mu}(\vartheta,\varphi)\right)_i \tag{30b}$$

$$\hat{M}^{\mathrm{E}}_{\mathrm{vor};\lambda\mu} = \frac{-\mathrm{i}/c}{2\lambda+3}\sqrt{\frac{2\lambda+1}{\lambda+1}}\int \mathrm{d}^3r\,\hat{\vec{j}}_{\mathrm{nuc}}(\vec{r})r^{\lambda+1}\vec{Y}^{\lambda+1}_{\lambda\mu}(\vartheta,\varphi) = \hat{M}^{\mathrm{E}}_{\mathrm{tor};\lambda\mu} + \hat{M}^{E}_{\mathrm{com};\lambda\mu} \tag{30c}$$

$$\hat{M}^{\mathrm{E}}_{\mathrm{tor};\lambda\mu} = \frac{-1}{2c(2\lambda+3)}\sqrt{\frac{\lambda}{\lambda+1}}\int \mathrm{d}^3r\,\hat{\vec{j}}_{\mathrm{nuc}}(\vec{r})\cdot\vec{\nabla}\times\left[r^{\lambda+2}\vec{Y}^{\lambda}_{\lambda\mu}(\vartheta,\varphi)\right] \tag{30d}$$

$$\hat{M}^{\mathrm{E}}_{\mathrm{com};\lambda\mu} = \frac{\mathrm{i}}{2c(2\lambda+3)}\int \mathrm{d}^3r\,\hat{\vec{j}}_{\mathrm{nuc}}(\vec{r})\cdot\vec{\nabla}\left[r^{\lambda+2}Y_{\lambda\mu}(\vartheta,\varphi)\right] \qquad \left(=-k\hat{M}^{\mathrm{E}\prime}_{\mathrm{com};\lambda\mu}\right) \tag{30e}$$

$$\hat{M}^{\mathrm{E}\prime}_{\mathrm{com};\lambda\mu} = \sum_i \hat{M}^{\mathrm{E}\prime}_{\mathrm{com};\lambda\mu}(\vec{r}_i) = \frac{e}{2(2\lambda+3)}\sum_{q=p,n} z_q \sum_{i\in q}\Big(r^{\lambda+2}Y_{\lambda\mu}(\vartheta,\varphi)\Big)_i \tag{30f}$$

where z_q are effective charges of the nucleons, $g_{l/s,q}$ are orbital/spin g-factors (we take $g_{l,q} = z_q$; spin g-factors are reduced by a quenching factor $\varsigma = 0.7$) and $\vec{j}_{\mathrm{nuc}}$ is the nuclear current composed of convective and magnetization part

$$\hat{\vec{j}}_{\mathrm{nuc}}(\vec{r}) = \frac{e\hbar}{m_p}\sum_{q=p,n}\sum_{i\in q}\Big[z_q\hat{\vec{j}}_i(\vec{r}) + \frac{1}{4}g_{s,q}\vec{\nabla}\times\hat{\vec{s}}_i(\vec{r})\Big] \tag{31}$$

where (convective) current and spin one-body operators are the same as in Skyrme functional (4).

RPA formalism in axial symmetry

Axial coordinates are

$$\varrho = \sqrt{x^2+y^2},\ z,\ \varphi; \qquad x = \varrho\cos\varphi,\ y = \varrho\sin\varphi \tag{32}$$

Calculations in axially deformed nuclei don't conserve total angular momentum (previously denoted J or λ), nevertheless, they conserve its z-projection (μ) and parity, so it is convenient to preserve part of the formalism from spherical symmetry, namely the convention of m-components for vector and tensor operators, and their hermitian conjugation (12). Operators of differentiation are then

$$\nabla_{\pm1} = \frac{1}{\sqrt{2}}\left(\mp\frac{\partial}{\partial x} - \mathrm{i}\frac{\partial}{\partial y}\right) = \mp\frac{\mathrm{e}^{\pm\mathrm{i}\varphi}}{\sqrt{2}}\left(\frac{\partial}{\partial\varrho} \pm \frac{\mathrm{i}}{\varrho}\frac{\partial}{\partial\varphi}\right), \qquad \nabla_0 = \frac{\partial}{\partial z} \tag{33}$$

Single-particle wavefunction (and its time-reversal conjugate) is expressed as a spinor

$$\psi_\alpha(\vec{r}) = \begin{pmatrix} R_{\alpha\uparrow}(\varrho,z)\mathrm{e}^{\mathrm{i}m^-_\alpha\varphi} \\ R_{\alpha\downarrow}(\varrho,z)\mathrm{e}^{\mathrm{i}m^+_\alpha\varphi}\end{pmatrix}, \quad \psi_{\bar\alpha}(\vec{r}) = \begin{pmatrix} R_{\alpha\downarrow}(\varrho,z)\mathrm{e}^{-\mathrm{i}m^+_\alpha\varphi} \\ -R_{\alpha\uparrow}(\varrho,z)\mathrm{e}^{-\mathrm{i}m^-_\alpha\varphi}\end{pmatrix}, \quad \text{where } \ m^\pm_\alpha = m_\alpha \pm \frac{1}{2} \tag{34}$$

and the radial parts of its derivatives will be denoted by a shorthand notation

$$\begin{aligned}\nabla_{\pm1}\psi_\alpha &= \mp\frac{\mathrm{e}^{\pm\mathrm{i}\varphi}}{\sqrt{2}}\begin{pmatrix}(\partial_\varrho R_{\alpha\uparrow} \mp m^-_\alpha R_{\alpha\uparrow}/\varrho)\mathrm{e}^{\mathrm{i}m^-_\alpha\varphi} \\ (\partial_\varrho R_{\alpha\downarrow} \mp m^+_\alpha R_{\alpha\downarrow}/\varrho)\mathrm{e}^{\mathrm{i}m^+_\alpha\varphi}\end{pmatrix} \equiv \mathrm{e}^{\pm\mathrm{i}\varphi}\begin{pmatrix}R^{(\pm)}_{\alpha\uparrow}\mathrm{e}^{\mathrm{i}m^-_\alpha\varphi} \\ R^{(\pm)}_{\alpha\downarrow}\mathrm{e}^{\mathrm{i}m^+_\alpha\varphi}\end{pmatrix} \\ \nabla_0\psi_\alpha &= \begin{pmatrix}\partial_z R_{\alpha\uparrow}\mathrm{e}^{\mathrm{i}m^-_\alpha\varphi} \\ \partial_z R_{\alpha\downarrow}\mathrm{e}^{\mathrm{i}m^+_\alpha\varphi}\end{pmatrix} \equiv \begin{pmatrix}R^{(0)}_{\alpha\uparrow}\mathrm{e}^{\mathrm{i}m^-_\alpha\varphi} \\ R^{(0)}_{\alpha\downarrow}\mathrm{e}^{\mathrm{i}m^+_\alpha\varphi}\end{pmatrix}\end{aligned} \tag{35}$$

Radial functions $R_{\alpha\uparrow\downarrow}(\varrho,z)$, $R^{(\pm)}_{\alpha\uparrow\downarrow}(\varrho,z)$ are real, and their spinor-wise products will be denoted by a dot to keep the expressions simple:

$$R_\alpha\cdot R_\beta \ \equiv\ R_{\alpha\uparrow}(\varrho,z)R_{\beta\uparrow}(\varrho,z) + R_{\alpha\downarrow}(\varrho,z)R_{\beta\downarrow}(\varrho,z) \tag{36}$$

Vector currents will be decomposed in the style of rank-1 tensor operators. Vector product in the expression for spin-orbital current leads to (for vector product in m-scheme see [15, (1.2.28)])

$$(\vec{\nabla}\times\vec{\sigma})\psi_\alpha = \begin{cases} +1: & \mathrm{i}\,\mathrm{e}^{\mathrm{i}\varphi}\begin{pmatrix}(-R^{(+)}_{\alpha\uparrow} - \sqrt{2}\,R^{(0)}_{\alpha\downarrow})\mathrm{e}^{\mathrm{i}m^-_\alpha\varphi} \\ R^{(+)}_{\alpha\downarrow}\mathrm{e}^{\mathrm{i}m^+_\alpha\varphi}\end{pmatrix} \\ 0: & \mathrm{i}\begin{pmatrix}-\sqrt{2}\,R^{(-)}_{\alpha\downarrow}\mathrm{e}^{\mathrm{i}m^-_\alpha\varphi} \\ -\sqrt{2}\,R^{(+)}_{\alpha\uparrow}\mathrm{e}^{\mathrm{i}m^+_\alpha\varphi}\end{pmatrix} \\ -1: & \mathrm{i}\,\mathrm{e}^{-\mathrm{i}\varphi}\begin{pmatrix}R^{(-)}_{\alpha\uparrow}\mathrm{e}^{\mathrm{i}m^-_\alpha\varphi} \\ (-R^{(-)}_{\alpha\downarrow} - \sqrt{2}\,R^{(0)}_{\alpha\uparrow})\mathrm{e}^{\mathrm{i}m^+_\alpha\varphi}\end{pmatrix}\end{cases} \tag{37}$$

Matrix elements of densities and currents are then

$$\langle\alpha|\hat{\rho}|\beta\rangle = R_\alpha \cdot R_\beta \, \mathrm{e}^{\mathrm{i}(m_\beta - m_\alpha)\varphi} \tag{38a}$$

$$\langle\alpha|\hat{\tau}|\beta\rangle = \big(R^{(0)}_\alpha \cdot R^{(0)}_\beta + R^{(+)}_\alpha \cdot R^{(+)}_\beta + R^{(-)}_\alpha \cdot R^{(-)}_\beta\big) \, \mathrm{e}^{\mathrm{i}(m_\beta - m_\alpha)\varphi} \tag{38b}$$

Factor $\mathrm{e}^{\mathrm{i}(m_\beta - m_\alpha)\varphi}$ will be omitted in the following expressions.

$$\langle\alpha|\vec{\mathcal{J}}|\beta\rangle = \begin{cases} +1: & \frac{1}{2}\mathrm{e}^{\mathrm{i}\varphi}\big[\big(R^{(-)}_{\alpha\downarrow} + \sqrt{2}\,R^{(0)}_{\alpha\uparrow}\big)R_{\beta\downarrow} - R^{(-)}_{\alpha\uparrow}R_{\beta\uparrow} - R_{\alpha\uparrow}\big(R^{(+)}_{\beta\uparrow} + \sqrt{2}\,R^{(0)}_{\beta\downarrow}\big) + R_{\alpha\downarrow}R^{(+)}_{\beta\downarrow}\big] \\ 0: & \frac{1}{2}\big[-\sqrt{2}\,\big(R^{(-)}_{\alpha\downarrow}R_{\beta\uparrow} + R^{(+)}_{\alpha\uparrow}R_{\beta\downarrow} + R_{\alpha\uparrow}R^{(-)}_{\beta\downarrow} + R_{\alpha\downarrow}R^{(+)}_{\beta\uparrow}\big)\big] \\ -1: & \frac{1}{2}\mathrm{e}^{-\mathrm{i}\varphi}\big[\big(R^{(+)}_{\alpha\uparrow} + \sqrt{2}\,R^{(0)}_{\alpha\downarrow}\big)R_{\beta\uparrow} - R^{(+)}_{\alpha\downarrow}R_{\beta\downarrow} - R_{\alpha\downarrow}\big(R^{(-)}_{\beta\downarrow} + \sqrt{2}\,R^{(0)}_{\beta\uparrow}\big) + R_{\alpha\uparrow}R^{(-)}_{\beta\uparrow}\big] \end{cases} \tag{38c}$$

$$\langle\alpha|\vec{j}|\beta\rangle = \begin{cases} +1: & \frac{\mathrm{i}}{2}\mathrm{e}^{\mathrm{i}\varphi}\big(-R^{(-)}_\alpha \cdot R_\beta - R_\alpha \cdot R^{(+)}_\beta\big) \\ 0: & \frac{\mathrm{i}}{2}\big(R^{(0)}_\alpha \cdot R_\beta - R_\alpha \cdot R^{(0)}_\beta\big) \\ -1: & \frac{\mathrm{i}}{2}\mathrm{e}^{-\mathrm{i}\varphi}\big(-R^{(+)}_\alpha \cdot R_\beta - R_\alpha \cdot R^{(-)}_\beta\big) \end{cases} \qquad \langle\alpha|\vec{s}|\beta\rangle = \begin{cases} +1: & \mathrm{e}^{\mathrm{i}\varphi}\big(-\sqrt{2}\,R_{\alpha\uparrow}R_{\beta\downarrow}\big) \\ 0: & R_{\alpha\uparrow}R_{\beta\uparrow} - R_{\alpha\downarrow}R_{\beta\downarrow} \\ -1: & \mathrm{e}^{-\mathrm{i}\varphi}\big(\sqrt{2}\,R_{\alpha\downarrow}R_{\beta\uparrow}\big) \end{cases} \tag{38d}$$

$$\langle\alpha|\vec{T}|\beta\rangle = \begin{cases} +1: & \mathrm{e}^{\mathrm{i}\varphi}(-\sqrt{2}\,)\big[R^{(0)}_{\alpha\uparrow}R^{(0)}_{\beta\downarrow} + R^{(+)}_{\alpha\uparrow}R^{(+)}_{\beta\downarrow} + R^{(-)}_{\alpha\uparrow}R^{(-)}_{\beta\downarrow}\big] \\ 0: & R^{(0)}_{\alpha\uparrow}R^{(0)}_{\beta\uparrow} - R^{(0)}_{\alpha\downarrow}R^{(0)}_{\beta\downarrow} + R^{(+)}_{\alpha\uparrow}R^{(+)}_{\beta\uparrow} - R^{(+)}_{\alpha\downarrow}R^{(+)}_{\beta\downarrow} + R^{(-)}_{\alpha\uparrow}R^{(-)}_{\beta\uparrow} - R^{(-)}_{\alpha\downarrow}R^{(-)}_{\beta\downarrow} \\ -1: & \mathrm{e}^{-\mathrm{i}\varphi}\sqrt{2}\,\big[R^{(0)}_{\alpha\downarrow}R^{(0)}_{\beta\uparrow} + R^{(+)}_{\alpha\downarrow}R^{(+)}_{\beta\uparrow} + R^{(-)}_{\alpha\downarrow}R^{(-)}_{\beta\uparrow}\big] \end{cases} \tag{38e}$$

$$\langle\alpha|\vec{\nabla}\times\vec{j}|\beta\rangle = -\mathrm{i}\big(\vec{\nabla}\psi_\alpha\big)^\dagger \times \vec{\nabla}\psi_\beta = \begin{cases} +1: & \mathrm{e}^{\mathrm{i}\varphi}\big(R^{(-)}_\alpha \cdot R^{(0)}_\beta + R^{(0)}_\alpha \cdot R^{(+)}_\beta\big) \\ 0: & R^{(-)}_\alpha \cdot R^{(-)}_\beta - R^{(+)}_\alpha \cdot R^{(+)}_\beta \\ -1: & \mathrm{e}^{-\mathrm{i}\varphi}\big(-R^{(+)}_\alpha \cdot R^{(0)}_\beta - R^{(0)}_\alpha \cdot R^{(-)}_\beta\big) \end{cases} \tag{38f}$$

$$\begin{aligned} \langle\alpha|\vec{\nabla}\cdot\vec{\mathcal{J}}|\beta\rangle = {} & -R^{(+)}_{\alpha\uparrow}R^{(+)}_{\beta\uparrow} + R^{(+)}_{\alpha\downarrow}R^{(+)}_{\beta\downarrow} + R^{(-)}_{\alpha\uparrow}R^{(-)}_{\beta\uparrow} - R^{(-)}_{\alpha\downarrow}R^{(-)}_{\beta\downarrow} \\ & - \sqrt{2}\,\big(R^{(0)}_{\alpha\uparrow}R^{(-)}_{\beta\downarrow} + R^{(-)}_{\alpha\downarrow}R^{(0)}_{\beta\uparrow} + R^{(0)}_{\alpha\downarrow}R^{(+)}_{\beta\uparrow} + R^{(+)}_{\alpha\uparrow}R^{(0)}_{\beta\downarrow}\big) \end{aligned} \tag{38g}$$

$$\begin{aligned} \langle\alpha|\mathcal{J}_s|\beta\rangle = {} & \tfrac{\mathrm{i}}{2}\big[\big(R^{(0)}_{\alpha\uparrow} + \sqrt{2}\,R^{(-)}_{\alpha\downarrow}\big)R_{\beta\uparrow} - \big(R^{(0)}_{\alpha\downarrow} + \sqrt{2}\,R^{(+)}_{\alpha\uparrow}\big)R_{\beta\downarrow} \\ & - R_{\alpha\uparrow}\big(R^{(0)}_{\beta\uparrow} + \sqrt{2}\,R^{(-)}_{\alpha\downarrow}\big) + R_{\alpha\downarrow}\big(R^{(0)}_{\beta\downarrow} + \sqrt{2}\,R^{(+)}_{\beta\uparrow}\big)\big] \end{aligned} \tag{38h}$$

$$\langle\alpha|\mathcal{J}_t|\beta\rangle = \begin{cases} +2: & \frac{\mathrm{i}}{\sqrt{2}}\mathrm{e}^{2\mathrm{i}\varphi}\big(R^{(-)}_{\alpha\uparrow}R_{\beta\downarrow} + R_{\alpha\uparrow}R^{(+)}_{\beta\downarrow}\big) \\ +1: & \frac{\mathrm{i}}{2\sqrt{2}}\mathrm{e}^{\mathrm{i}\varphi}\big[-R^{(-)}_{\alpha\uparrow}R_{\beta\uparrow} + \big(R^{(-)}_{\alpha\downarrow} - \sqrt{2}\,R^{(0)}_{\alpha\uparrow}\big)R_{\beta\downarrow} - R_{\alpha\uparrow}\big(R^{(+)}_{\beta\uparrow} - \sqrt{2}\,R^{(0)}_{\beta\downarrow}\big) + R_{\alpha\downarrow}R^{(+)}_{\beta\downarrow}\big] \\ 0: & \frac{\mathrm{i}}{2\sqrt{3}}\big[\big(\sqrt{2}\,R^{(0)}_{\alpha\uparrow} - R^{(-)}_{\alpha\downarrow}\big)R_{\beta\uparrow} - \big(\sqrt{2}\,R^{(0)}_{\alpha\downarrow} - R^{(+)}_{\alpha\uparrow}\big)R_{\beta\downarrow} \\ & \qquad - R_{\alpha\uparrow}\big(\sqrt{2}\,R^{(0)}_{\beta\uparrow} - R^{(-)}_{\beta\downarrow}\big) + R_{\alpha\downarrow}\big(\sqrt{2}\,R^{(0)}_{\beta\downarrow} - R^{(+)}_{\beta\uparrow}\big)\big] \\ -1: & \frac{\mathrm{i}}{2\sqrt{2}}\mathrm{e}^{-\mathrm{i}\varphi}\big[-\big(R^{(+)}_{\alpha\uparrow} - \sqrt{2}\,R^{(0)}_{\alpha\downarrow}\big)R_{\beta\uparrow} + R^{(+)}_{\alpha\downarrow}R_{\beta\downarrow} - R_{\alpha\uparrow}R^{(-)}_{\beta\uparrow} + R_{\alpha\downarrow}\big(R^{(-)}_{\beta\downarrow} - \sqrt{2}\,R^{(0)}_{\beta\uparrow}\big)\big] \\ -2: & \frac{\mathrm{i}}{\sqrt{2}}\mathrm{e}^{2\mathrm{i}\varphi}\big(-R^{(+)}_{\alpha\downarrow}R_{\beta\uparrow} - R_{\alpha\downarrow}R^{(-)}_{\beta\uparrow}\big) \end{cases} \tag{38i}$$

$$\hat{\vec{L}}\psi_\beta = -\mathrm{i}(\vec{r}\times\vec{\nabla})\psi_\beta = \begin{cases} +1: & \mathrm{e}^{\mathrm{i}\varphi}\big(\frac{\varrho}{\sqrt{2}}R^{(0)}_\beta + zR^{(+)}_\beta\big) \\ 0: & \frac{\varrho}{\sqrt{2}}\big(R^{(+)}_\beta + R^{(-)}_\beta\big) \\ -1: & \mathrm{e}^{-\mathrm{i}\varphi}\big(\frac{\varrho}{\sqrt{2}}R^{(0)}_\beta - zR^{(-)}_\beta\big) \end{cases} \tag{38j}$$

In the actual calculation, it is necessary to choose projection of angular momentum μ and parity π (together denoted also as K^π, and $\mu = \pm K$). Transition operators have the form of

$$\hat{M}_{\lambda\mu} = \sum_i M_{\lambda\mu}(\varrho_i, z_i)\,\mathrm{e}^{\mathrm{i}\mu\varphi_i} \tag{39}$$

where $M_{\lambda\mu}(\varrho, z)$ contains a function (or even derivatives) not dependent on φ. Choice of the two-quasiparticle pairs is restricted by $m_\alpha - m_\beta = \mu$ (time-reversed states are omitted from the discussion here for simplicity; in short, it is necessary to add pairs $(\alpha, \bar{\beta})$ with $m_\alpha + m_\beta = \mu$ during the duplicate removal similar to (21)). Commutators are then evaluated in quasiparticle vacuum as

$$\langle[\hat{A}^\dagger, \hat{B}]\rangle = \frac{\gamma^A_T - \gamma^B_T}{2}\sum_{\alpha\beta} u^{(\gamma^A_T)}_{\beta\alpha}u^{(\gamma^B_T)}_{\alpha\beta}\langle\beta|\hat{A}^\dagger|\alpha\rangle\langle\alpha|\hat{B}|\beta\rangle = \frac{1 - \gamma^A_T\gamma^B_T}{2}\sum_{\alpha\beta} u^{(\gamma^A_T)}_{\alpha\beta}u^{(\gamma^B_T)}_{\alpha\beta}\langle\alpha|\hat{A}|\beta\rangle^*\,\langle\alpha|\hat{B}|\beta\rangle \tag{40}$$

Single-particle operators (including densities and currents) can be expressed in terms of quasiparticles

$$\hat{A} = \frac{1}{2}\sum_{\alpha\beta} u^{(\gamma^A_T)}_{\alpha\beta}\langle\alpha|\hat{A}|\beta\rangle\big(\hat{\alpha}^+_\alpha\hat{\alpha}^+_{\bar{\beta}} + \gamma^A_T\hat{\alpha}_{\bar{\alpha}}\hat{\alpha}_\beta\big) \tag{41}$$

$$\hat{\mathbf{J}}_d(\vec{r}) = \frac{1}{2}\sum_\mu \sum_{\alpha\beta\in\mu} \mathbf{J}_{d;\alpha\beta}(\varrho, z)\big(\hat{\alpha}^+_\alpha\hat{\alpha}^+_{\bar{\beta}} + \gamma^d_T\hat{\alpha}_{\bar{\alpha}}\hat{\alpha}_\beta\big)\mathrm{e}^{-\mathrm{i}\mu\varphi}, \qquad \text{where} \;\; m_\alpha - m_\beta = \mu \tag{42}$$

Expression (42) is defining the shorthand notation $\mathbf{J}_{d;\alpha\beta}(\varrho,z)$ for matrix elements of densities and currents which can have scalar, vector or tensor character. RPA phonons are defined as

$$\hat{C}^+_\nu = \frac{1}{2}\sum_{\alpha\beta}\left(c^{(\nu-)}_{\alpha\beta}\hat{\alpha}^+_\alpha\hat{\alpha}^+_{\bar{\beta}} - c^{(\nu+)}_{\alpha\beta}\hat{\alpha}_{\bar{\alpha}}\hat{\alpha}_\beta\right) \tag{43}$$

(factor 1/2 is due to double counting of $\alpha\beta$ vs. $\bar{\beta}\bar{\alpha}$) and their commutator with hermitian density/current operator is

$$\langle[\hat{\mathbf{J}}_d(\vec{r}),\hat{C}^+_\nu]\rangle = \frac{1}{2}\sum_{\alpha\beta}u^{(\gamma^d_T)}_{\alpha\beta}\langle\alpha|\hat{\mathbf{J}}_d(\vec{r})|\beta\rangle^*\left(c^{(\nu-)}_{\alpha\beta}+\gamma^d_T c^{(\nu+)}_{\alpha\beta}\right) = \frac{1}{2}\sum_{\alpha\beta}\mathbf{J}^\dagger_{d;\alpha\beta}(\varrho,z)\left(c^{(\nu-)}_{\alpha\beta}+\gamma^d_T c^{(\nu+)}_{\alpha\beta}\right)\mathrm{e}^{\mathrm{i}\mu\varphi} \tag{44}$$

where hermitian conjugation is understood in the sense of (12) for vector/tensor components (see also decomposition of matrix elements (38) to these components) and the factor $\mathrm{e}^{\mathrm{i}\mu\varphi}$ will get canceled by $\mathrm{e}^{-\mathrm{i}\mu\varphi}$ from another $\hat{\mathbf{J}}_{d'}(\vec{r})$ in Skyrme interaction or in Coulomb integral (48). The matrices A and B coming from the RPA equations $[\hat{H},\hat{C}^+_\nu] = E_\nu\hat{C}^+_\nu$ (23) are then

$$A_{pp'} = \delta_{pp'}\varepsilon_p + \sum_{dd'}\iint \mathrm{d}\vec{r}_1\mathrm{d}\vec{r}_2\frac{\delta^2\mathcal{H}}{\delta J_d(\vec{r}_1)\delta J_{d'}(\vec{r}_2)}\mathbf{J}^\dagger_{d;p}(\varrho_1,z_1)\cdot\mathbf{J}_{d';p'}(\varrho_2,z_2) \tag{45a}$$

$$B_{pp'} = \sum_{dd'}\gamma^d_T\iint \mathrm{d}\vec{r}_1\mathrm{d}\vec{r}_2\frac{\delta^2\mathcal{H}}{\delta J_d(\vec{r}_1)\delta J_{d'}(\vec{r}_2)}\mathbf{J}^\dagger_{d;p}(\varrho_1,z_1)\cdot\mathbf{J}_{d';p'}(\varrho_2,z_2) \tag{45b}$$

Index p labels the $2qp$ pair (e.g. $\alpha\beta$), satisfying $m_\alpha - m_\beta = \mu$ and the scalar product is understood in the spherical-tensor sense

$$\mathbf{A}^\dagger\cdot\mathbf{B} = \sum_s(-1)^s\left[\mathbf{A}^\dagger\right]_{-s}\left[\mathbf{B}\right]_s = \sum_s\left[\mathbf{A}\right]^*_s\left[\mathbf{B}\right]_s \tag{46}$$

Pairing is included only for $\mu = 0$ and positive parity, and only for diagonal $2qp$ pairs ($\beta = \alpha$). Density dependent pairing force then leads to two terms in the residual interaction: $\delta^2\mathcal{H}/\delta\kappa\delta\kappa$ and $\delta^2\mathcal{H}/\delta\kappa\delta\rho$.

Finally, a few words have to be said about numerical integration, in particular about Coulomb integral. Calculations are done on an equidistant cylindrical grid (with the grid spacing denoted here as Δ). In that case, the radial integral has a non-zero (first) Euler-Maclaurin correction in the center (in contrast with spherical integration, which has none):

$$\int_0^\infty f(\varrho)\varrho\,\mathrm{d}\varrho = \left[\tfrac{\Delta}{12}f(0) + 1\Delta f(1\Delta) + 2\Delta f(2\Delta) + 3\Delta f(3\Delta) + \ldots\right]\Delta \tag{47}$$

Coulomb integral is

$$\iint\frac{\rho^*_1(\varrho_1,z_1)\rho_2(\varrho_2,z_2)}{|\vec{r}_1-\vec{r}_2|}\,\mathrm{e}^{\mathrm{i}m_1\varphi_1-\mathrm{i}m_2\varphi_2}\mathrm{d}\vec{r}_1\mathrm{d}\vec{r}_2 = 2\pi\delta_{m_1m_2}\int_0^\infty\rho^*_1(\varrho_1,z_1)\varrho_1\mathrm{d}\varrho_1\mathrm{d}z_1\int_0^\infty\rho_2(\varrho_2,z_2)\varrho_2\mathrm{d}\varrho_2\mathrm{d}z_2$$
$$\times\frac{g_m\left(\frac{2\varrho_1\varrho_2}{(z_1-z_2)^2+\varrho_1^2+\varrho_2^2}\right)}{\sqrt{(z_1-z_2)^2+\varrho_1^2+\varrho_2^2}} \tag{48}$$

$$\text{where}\quad g_m(x) = \int_{-\pi}^{\pi}\frac{\cos(m\varphi)}{\sqrt{1-x\cos\varphi}}\mathrm{d}\varphi = 2\pi\sum_{k=0}^{\infty}\frac{(4k+2m-1)!!}{k!(k+m)!}\left(\frac{x}{4}\right)^{m+2k} \tag{49}$$

Function $g_m(x)$ is evaluated by numerical integration or by Taylor expansion (for small x and large m). It has a logarithmic singularity in $x\to1^-$ like $g_m(1-t) = (O(t)-\sqrt{2})\ln t + O(1)$. The singularity can be replaced in the equidistant cylindrical grid by an empirical expression (found by investigation of the convergence with decreasing grid spacing):

$$\left.\frac{g_m\left(\frac{2\varrho_1\varrho_2}{(z_1-z_2)^2+\varrho_1^2+\varrho_2^2}\right)}{\sqrt{(z_1-z_2)^2+\varrho_1^2+\varrho_2^2}}\right|_{z_1=z_2,\,\varrho_1=\varrho_2} = \frac{1}{\varrho}\left[2\ln\frac{\varrho}{\Delta} + 6.779948935 - 4\sum_{n=1}^{m}\frac{1}{2n-1}\right] + O(\Delta^2) \tag{50}$$

For the point on the axis ($z_1 = z_2$ and $\varrho_1 = \varrho_2 = 0$, assuming $m = 0$; otherwise the contribution is zero), the first term in (47) is replaced as

$$\frac{\Delta}{12}\frac{\rho_2(0,z_2)g_0(0)}{\sqrt{0^2+0^2+0^2}} \quad\mapsto\quad 2.1770180559\,\rho_2(0,z_1) \tag{51}$$

Numerical results

The influence of omission of tensor and spin terms in Skyrme functional (2) is illustrated for spherical nucleus ^{208}Pb. Skyrme parametrization SLy7 [13], fitted with tensor term, was utilized. Isovector E1 strength functions (long-wave, toroidal and compression) are given in Fig. 1 with Lorentzian smoothing of 1 MeV. Magnetic M1 strength functions are given in Fig. 2 (smoothing 0.15 MeV).

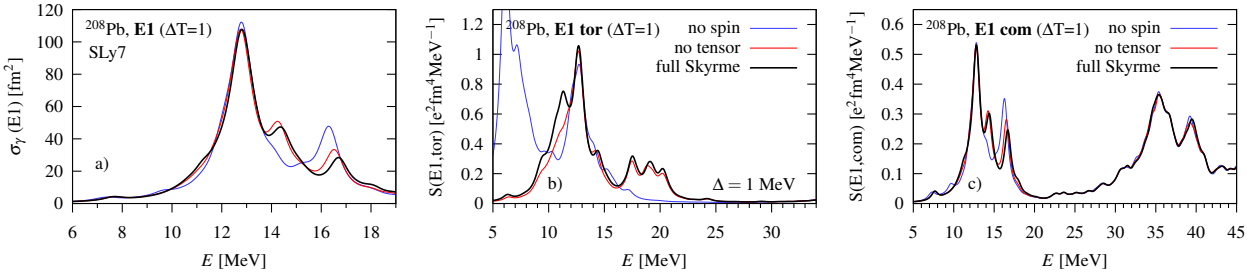

Fig. 1: Isovector E1 resonances in ^{208}Pb for parametrization SLy7 [13] with corresponding effective charges: a) giant dipole (long-wave), $z_p = N/A$, $z_n = -Z/A$; b) toroidal and c) compression resonances with $z_p = -z_n = 0.5$, $g_p = -g_n = 4.7\varsigma$ ($\varsigma = 0.7$).

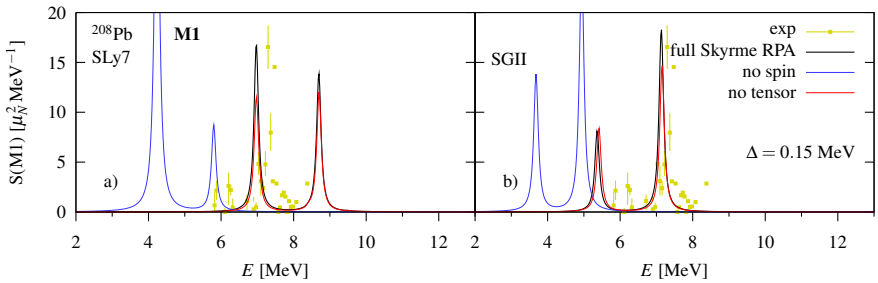

Fig. 2: M1 resonances in ^{208}Pb with natural charges and parametrizations: a) SLy7 [13], b) SGII [12]. Experimental data are from [17].

As can be seen, omission of tensor terms has only a minor influence on all results, while the omitted spin terms give a large unphysical shift mainly in M1 strength functions, and also in toroidal E1. Both E1 and M1 were calculated with exhaustive basis: 120 main shells of spherical harmonic oscillator (with length 1.7 fm) in HF, and 106 main shells passed to RPA. Spurious state in E1 is under 1 keV for the full Skyrme and "no spin" case, while the "no tensor" case gave imaginary state at 0.78i MeV due to broken self-consistency in residual interaction (tensor term was omitted only in RPA).

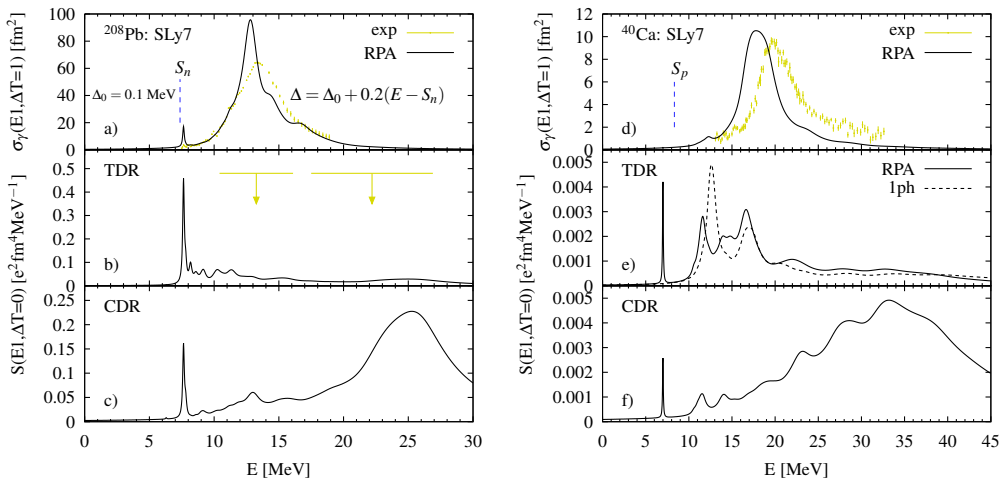

Fig. 3: E1 strengths in ^{208}Pb and ^{40}Ca with pygmy region emphasized by variable smoothing. Dipolar resonances are compared with experiment a) [18], b,c) [19] (isoscalar E1), d) [20]. Isoscalar toroidal (b,e) and compression (c,f) strength functions are calculated with $z_p = z_n = 0.5$, $g_p = g_n = 0.88\varsigma$ ($\varsigma = 0.7$).

As was shown in our previous work [21, 22], pygmy resonance (low-lying part of the E1 resonance) has a pronounced isoscalar toroidal nature, contrary to the previous interpretations, which assumed vibration of neutron skin against the core of the nucleus. These conclusions are illustrated here for spherical ^{208}Pb and ^{40}Ca by the strength function of isovector E1 (long-wave) and isoscalar toroidal and compression E1, with variable smoothing: starting with $\Delta = 0.1$ MeV up to particle emission threshold, and then linearly increasing to approximately simulate the escape width and coupling to complex configurations. Fig. 3 shows that pygmy resonance is not visible in isovector E1 for symmetric nucleus ^{40}Ca in agreement with its isoscalar nature (as found also in [23]). Strength functions and Fig. 4 demonstrate that the toroidal flow is dominant in low-energy region, while the compression flow (more akin to surface vibration) dominates for higher energies.

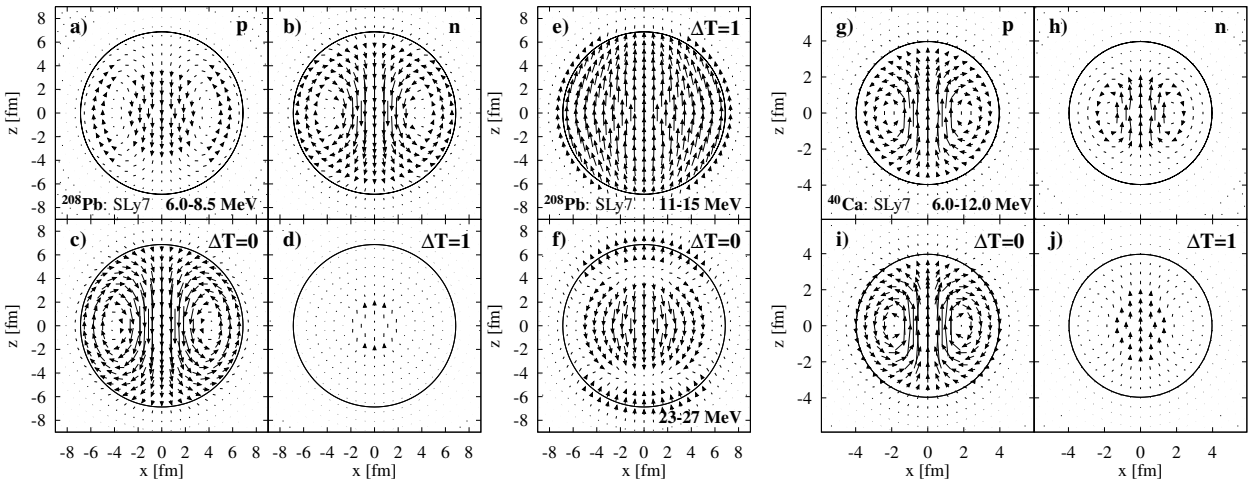

Fig. 4: E1 transition currents in ^{208}Pb and ^{40}Ca in various energy intervals, weighted by isovector E1 operator. ΔT=0 is the sum of proton and neutron current, ΔT=1 gives their difference.

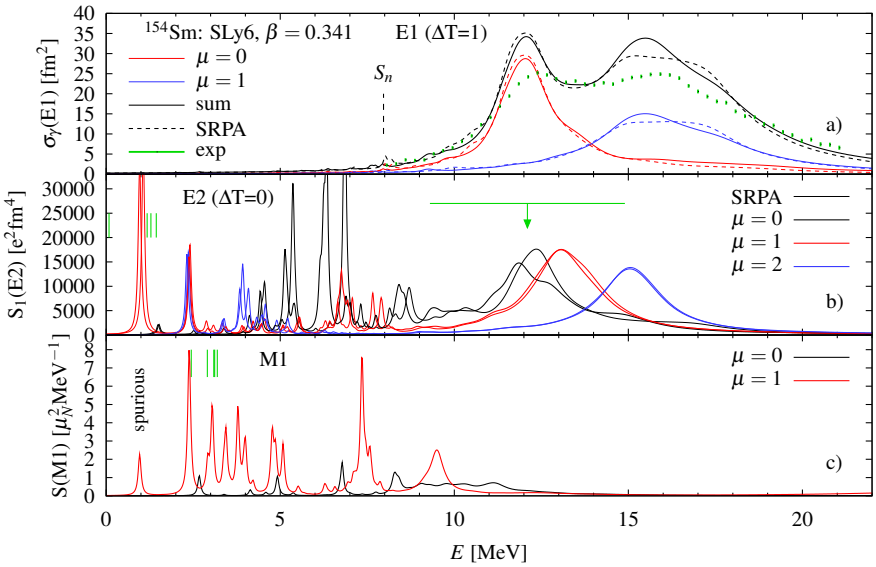

Fig. 5: Giant resonances in deformed nucleus ^{154}Sm given with variable smoothing, and showing pronounced deformation splitting as a function of μ. a) E1 resonance with SRPA denoted by dashed lines + experiment [24], b) E2 resonance with SRPA denoted by thin lines + experiment [19], c) M1 resonance, showing spurious peak at 0.96 MeV, corresponding to collective rotation.

Finally, a calculation with deformed nucleus ^{154}Sm is shown to demonstrate the accuracy of SRPA vs. full RPA (see Fig. 5), with a grid spacing of 0.4 fm, using single-particle states up to 40 MeV in RPA. The slowest calculations were for $\mu = 1$ (E1 and E2) with around 22.6 thousand $2qp$ pairs, taking around 24 hours utilizing 8 threads and around 23 GB of RAM for single $\lambda\mu$. Pairing strengths V_q for SLy6 were taken from [25]. Slight differences between full and separable RPA can be explained by an imperfect coverage of the residual interaction by its separable approximation (generated by five operators in each case). Toroidal currents are present in the pygmy region of ^{154}Sm E1 resonance, as is shown in Fig. 6.

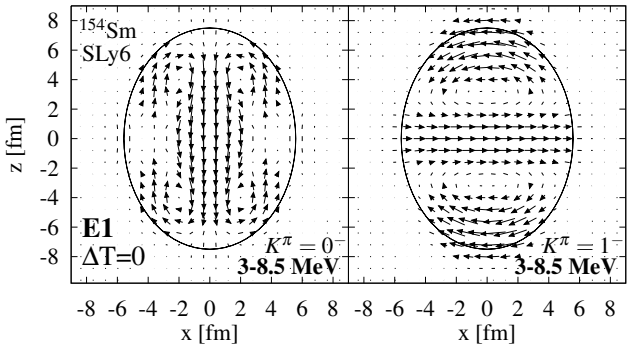

Fig. 6: Isoscalar E1 transition currents in the pygmy region of ^{154}Sm by full RPA.

CONCLUSIONS

Skyrme RPA formalism and some numerical results are presented for the case of spherical and axial symmetry. Formulae in axial basis are given here in detail as a reference for further calculations with full RPA, which is now becoming feasible on the common workstations.

Importance of time-odd Skyrme terms was shown for magnetic and toroidal transitions. Toroidal nature of pygmy resonance was demonstrated by transition current maps for both spherical (^{40}Ca, ^{208}Pb) and deformed nuclei (^{154}Sm).

ACKNOWLEDGMENT:
This work was supported by the Czech Science Foundation (P203-13-07117S) and by Votruba-Blokhintsev grant (Czech Republic-BLTP JINR).

REFERENCES

[1] D. Vautherin and D.M. Brink, Phys. Rev. C **5**, 626 (1972).
[2] W. Younes and D. Gogny, Phys. Rev. C **80**, 054313 (2009).
[3] T. Nikšić, N. Paar, D. Vretenar and P. Ring, Comput. Phys. Commun. **185**, 1808 (2014).
[4] P. Ring and P. Schuck, The Nuclear Many-Body Problem. Springer-Verlag, Berlin, 1980.
[5] P.-G. Reinhard and Y.K. Gambhir, Annalen der Physik **504**, 598 (1992).
[6] J. Terasaki, J. Engel, M. Bender, J. Dobaczewski, W. Nazarewicz and M. Stoitsov, Phys. Rev. C **71**, 034310 (2005).
[7] G. Colò, L. Cao, N. Van Giai and L. Capelli, Comput. Phys. Commun. **184**, 142 (2013).
[8] K. Yoshida and T. Nakatsukasa, Phys. Rev. C **88**, 034309 (2013).
[9] V.O. Nesterenko, J. Kvasil and P.-G. Reinhard, Phys. Rev. C **66**, 044307 (2002).
[10] V.O. Nesterenko, W. Kleinig, J. Kvasil, P. Vesely, P.-G. Reinhard and D.S. Dolci. Phys. Rev. C **74**, 064306 (2006).
[11] P. Vesely, J. Kvasil, V.O. Nesterenko, W. Kleinig, P.-G. Reinhard and V.Yu. Ponomarev, Phys. Rev. C **80**, 031302(R) (2009).
[12] N. Van Giai and H. Sagawa, Phys. Lett. B **106**, 379 (1981).
[13] E. Chabanat, P. Bonche, P. Haensel, J. Meyer and R. Schaeffer. Nucl. Phys. A **635**, 231 (1998).
[14] M. Bender, K. Rutz, P.-G. Reinhard and J.A. Maruhn. Eur. Phys. J. A **8**, 59 (2000).
[15] D.A. Varshalovich, A.N. Moskalev and V.K. Khersonskii, Quantum Theory of Angular Momentum. World Scientific, Singapore, 1988.
[16] J. Kvasil, V.O. Nesterenko, W. Kleinig, P.-G. Reinhard and P. Vesely, Phys. Rev. C **84**, 034303 (2011).
[17] R.M. Laszewski, R. Alarcon, D.S. Dale and S.D. Hoblit, Phys. Rev. Lett. **61**, 1710 (1988).
[18] A. Veyssiere, H. Beil, R. Bergere, P. Carlos and A. Lepretre, Nucl. Phys. A **159**, 561 (1970).
[19] D.H. Youngblood, Y.-W. Lui, H.L. Clark, B. John, Y. Tokimoto and X. Chen, Phys. Rev. C **69**, 034315 (2004).
[20] J. Ahrens et al., Nucl. Phys. A **251** 479 (1975).
[21] A. Repko, P.-G. Reinhard, V.O. Nesterenko and J. Kvasil, Phys. Rev. C **87**, 024305 (2013).
[22] P.-G. Reinhard, V.O. Nesterenko, A. Repko and J. Kvasil, Phys. Rev. C **89**, 024321 (2014).
[23] P. Papakonstantinou, V.Yu. Ponomarev, R. Roth and J. Wambach, Eur. Phys. J. A **47**, 14 (2011).
[24] P. Carlos, H. Beil, R. Bergere, A. Lepretre, A. De Miniac and A. Veyssiere, Nucl. Phys. A **225**, 171 (1974).
[25] L. Guo, J.A. Maruhn and P.-G. Reinhard, Phys. Rev. C **76**, 034317 (2007).

The ASY-EOS experiment at GSI: Constraining the symmetry energy at supra-saturation densities

P. Russotto[1,*], M. Chartier[2], M.D. Cozma[3], E. De Filippo[1], A. Le Fèvre[4], S. Gannon[2], I. Gašparić[5,6], M. Kiš[4,5], S. Kupny[7], Y. Leifels[4], R.C. Lemmon[8], Q. Li[9], J. Łukasik[10], P. Marini[11,12], P. Pawłowski[10], W. Trautmann[4], L. Acosta[13], M. Adamczyk[7], A. Al-Ajlan[14], M. Al-Garawi[15], S. Al-Homaidhi[14], F. Amorini[13], L. Auditore[16,17], T. Aumann[6], Y. Ayyad[18], V. Baran[13,19], Z. Basrak[5], R. Bassini[20], J. Benlliure[18], C. Boiano[20], M. Boisjoli[12], K. Boretzky[4], J. Brzychczyk[7], A. Budzanowski[10], G. Cardella[1], P. Cammarata[21], Z. Chajecki[22], A. Chbihi[12], M. Colonna[13], B. Czech[10], M. Di Toro[13,23], M. Famiano[24], V. Greco[13,23], L. Grassi[5], C. Guazzoni[20,25], P. Guazzoni[20,26], M. Heil[4], L. Heilborn[21], R. Introzzi[27], T. Isobe[28], K. Kezzar[15], A. Krasznahorkay[29], N. Kurz[4], E. La Guidara[1], G. Lanzalone[13,30], P. Lasko[7], I. Lombardo[31,32], W.G. Lynch[22], Z. Matthews[2], L. May[21], T. Minniti[1], M. Mostazo[18], A. Pagano[1], M. Papa[1], S. Pirrone[1], R. Pleskač[4], G. Politi[1,23], F. Porto[13,23], R. Reifarth[4], W. Reisdorf[4], F. Riccio[20,25], F. Rizzo[13,23], E. Rosato[31,32], D. Rossi[4,22], S. Santoro[16,17], H. Simon[4] I. Skwirczynska[10], Z. Sosin[7], L. Stuhl[29], A. Trifirò[16,17], M. Trimarchi[16,17], M.B. Tsang[22], G. Verde[1], M. Veselský[33], M. Vigilante[31,32], A. Wieloch[7], P. Wigg[2], H.H. Wolter[34], P. Wu[2], S. Yennello[21], P. Zambon[20,25], L. Zetta[20,26] M. Zoric[5]

[1] INFN-Sezione di Catania, Catania, Italy
[2] University of Liverpool, Liverpool, UK
[3] IFIN-HH, Magurele-Bucharest, Romania
[4] GSI Helmholtzzentrum, Darmstadt, Germany
[5] Ruder Bošković Institute, Zagreb, Croatia
[6] Technische Universität, Darmstadt, Germany
[7] Jagiellonian University, Kraków, Poland
[8] STFC Laboratory, Daresbury, UK
[9] Huzhou Teachers College, China
[10] IFJ-PAN, Kraków, Poland
[11] CENBGn Université de Bordeaux, CNRS/IN2P3, 33175 Gradignan, France
[12] GANIL, Caen, France
[13] INFN-Laboratori Nazionali del Sud, Catania, Italy
[14] KACST Riyadh, Riyadh, Saudi Arabia
[15] King Saud University, Riyadh, Saudi Arabia
[16] INFN-Gruppo Collegato di Messina, Messina, Italy
[17] Università di Messina, Messina, Italy
[18] University of Santiago de Compostela, Santiago de Compostela, Spain
[19] University of Bucharest, Bucharest, Romania
[20] INFN-Sezione di Milano, Milano, Italy
[21] Texas A&M University, College Station, USA
[22] NSCL Michigan State University, East Lansing, USA
[23] Università di Catania, Catania, Italy
[24] Western Michigan University, USA
[25] Politecnico di Milano, Milano, Italy
[26] Università degli Studi di Milano, Milano, Italy
[27] INFN, Politecnico di Torino, Torino, Italy
[28] RIKEN, Wako, Japan
[29] Institute of Nuclear Research, Debrecen, Hungary
[30] Università Kore, Enna, Italy
[31] INFN-Sezione di Napoli, Napoli, Italy
[32] Università di Napoli, Napoli, Italy
[33] Institute of Physics, Slovak Academy of Sciences, Bratislava, Slovakia
[34] LMU, München, Germany

Abstract

The elliptic-flow ratio of neutrons with respect to protons or light complex particles in reactions of heavy ions at pre-relativistic energies has been proposed as an observable sensitive to the strength of the sym-

*E-mail: russotto@lns.infn.it

metry term of the nuclear equation of state at supra-saturation densities. In the ASY-EOS experiment at the GSI laboratory, flows of neutrons and light charged particles were measured for ^{197}Au+^{197}Au, ^{96}Zr+^{96}Zr and ^{96}Ru+^{96}Ru collisions at 400 MeV/nucleon with the Large Area Neutron Detector LAND as part of a setup with several additional detection systems used for the event characterization. Flow results obtained for the Au+Au system, in comparison with predictions of the UrQMD transport model, confirm the moderately soft to linear density dependence of the symmetry energy deduced from the earlier FOPI-LAND data.

INTRODUCTION

The neutron-proton elliptic flow ratio and difference have been proposed as effective probes of the high-density behavior of the nuclear symmetry energy [1, 2, 3]. The comparison of existing data from the FOPI-LAND experiment [4] with calculations performed with the UrQMD transport model [5] suggests a moderately soft to linear symmetry term. The result suffers, however, from the considerable statistical uncertainty of the experimental data [1, 3]. The same data set was also compared to calculations performed with the Tübingen QMD model and a constraint compatible with the UrQMD result was obtained [6]. At the same time, a thorough study of the parameter dependence of the model predictions was performed in order to devise a route towards a model independent constraint of the the high-density symmetry energy [6]. It was, in particular, found that different parameterizations of the isovector part of the equation of state, the Gogny inspired (momentum dependent) vs. the power law (momentum independent) potential, lead to very similar results.

In order to improve the statistical accuracy of the experimental flow parameters for the Au+Au reaction and to extend the flow measurements to other systems, the symmetric collision systems ^{197}Au+^{197}Au, ^{96}Zr+^{96}Zr and ^{96}Ru+^{96}Ru at 400 MeV/nucleon incident energies have been chosen for the ASY-EOS experiment, conducted at the GSI laboratory in May 2011 (S394 experiment). As in the previous experiment, the Large Area Neutron Detector LAND [7] was used for the detection and identification of neutrons and light charged particles. By including the KRATTA telescope array [8] in the setup, the study of isospin effects in these reactions was extended to additional observables as, e.g., the yield ratios of light isobar pairs ^{3}H/^{3}He and ^{7}Li/^{7}Be.

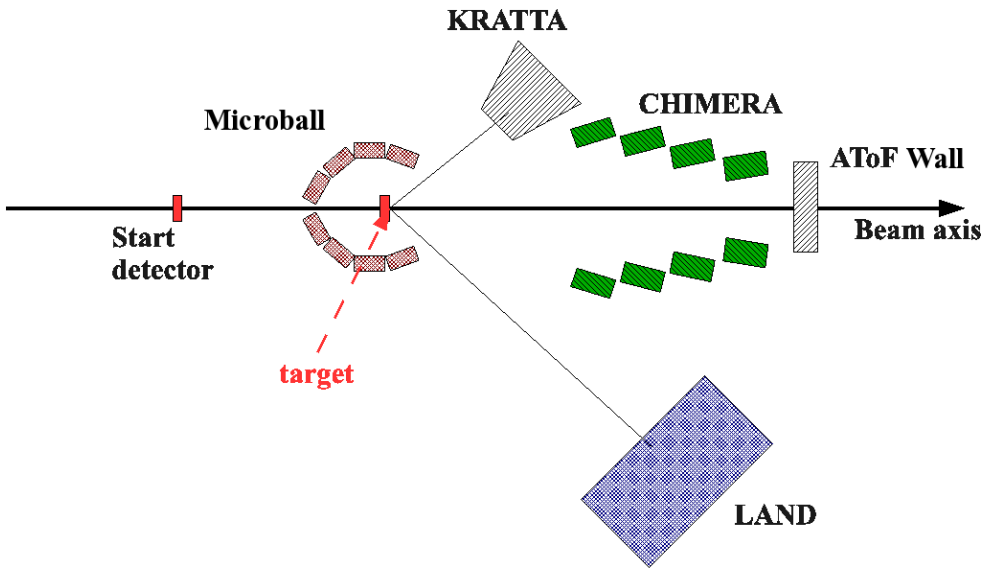

Fig. 1: Schematic view of the experimental setup of the ASY-EOS experiment S394 at GSI (not to scale; KRATTA and the Microball are smaller and closer to the target than shown here).

ASY-EOS EXPERIMENT AT GSI

A schematic view of the experimental set-up is shown in Fig. 1. The Large Area Neutron Detector (LAND) [7] was positioned to cover laboratory angles around 45° with respect to the beam direction, at a distance of about 5 m from the target. A veto-wall of plastic scintillators in front of LAND allowed discriminating neutrons and charged particles. In this configuration, it was possible to measure the direct

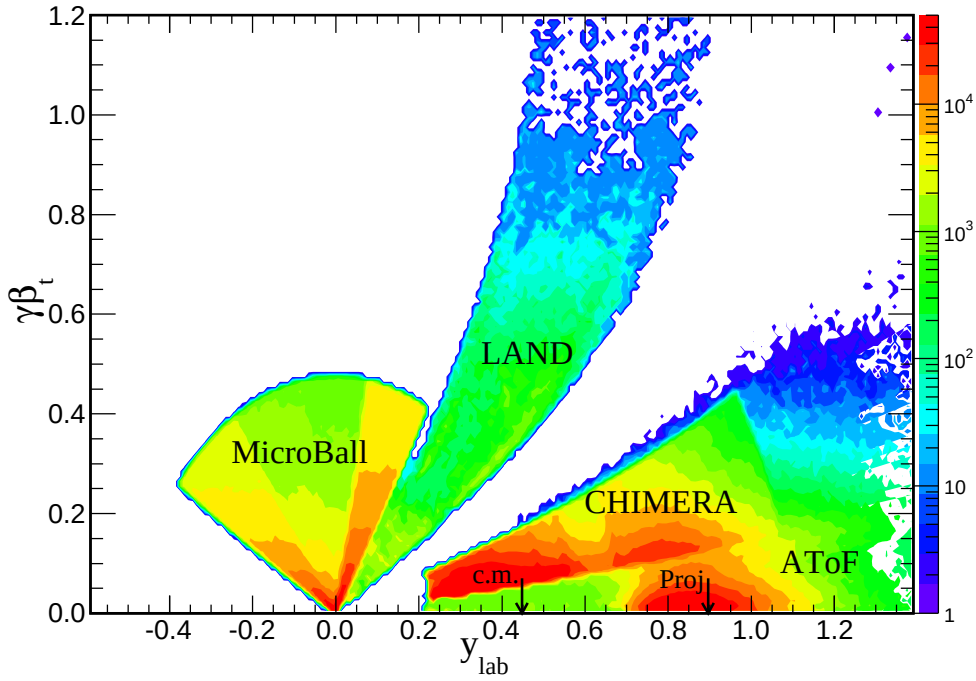

Fig. 2: Measured invariant hit distribution for $^{197}Au + ^{197}Au$ collisions at 400 MeV/nucleon incident energy in the transverse-velocity vs. rapidity plane for charged particles detected with the three systems Microball, CHIMERA, and AToF Wall with full azimuthal coverage and for neutrons detected with LAND. The velocity of particles detected with the Microball is not measured and shown here with an assumed distribution. The rapidities of the projectile $y_p = 0.896$ and of the c.m. system are indicated.

and elliptic flows of neutrons and charged particles at mid-rapidity with high precision in the same angular acceptance. In addition, the Kraków Triple Telescope Array, KRATTA [8], was installed to measure the energy, emission angles and isotopic composition of light charged reaction products. The 35 modules of KRATTA were arranged in a 7x5 array and placed opposite to LAND at a distance of 40 cm from the target. They covered 160 msr of solid angle at polar angles between 24° and 68°. The modules of KRATTA consisted of two, optically decoupled, CsI(Tl) crystals (thickness of 2.5 and 12.5 cm) and three large area, 500 μm thick, PIN photo-diodes. Very good isotopic resolution has been obtained in the whole dynamic range up to $Z \sim 6$ [9].

The determination of the impact parameter and the orientation of the reaction plane required the use of several devices: i) the ALADIN Time-of-Flight (AToF) wall [10] was used to detect charged particles at polar angles smaller than 7°; two walls (front and rear) of 2.5*100 cm^2 plastic scintillators, read by two photo-multipliers at both ends, gave information on emission angle, atomic number and velocity of forward-emitted ions; ii) 50 thin (between 3.6 and 5.6 mm) CsI(Tl) elements, read out by photo-diodes and arranged in 4 rings, of the Washington-University Microball array [11], surrounded the target at polar angles between 60° and 147° with the aim of measuring the multiplicity and angular distribution of backward emitted particles in order to discriminate against background reactions on non-target material; iii) 352 CsI(Tl) scintillators, 12 cm thick, of the CHIMERA multidetector [12], arranged in 8 rings with 2π azimuthal coverage around the beam axis and covering polar angles between 7° and 20°, were used to detect light charged particles from mid-rapidity emissions.

The kinematic coverage achieved with this assembly of detection systems is illustrated in Fig. 2. In particular, the enhanced particle yields in the kinematic regimes of participant and spectator emissions are clearly visible. The product yields from the decay of the projectile spectator seen with CHIMERA and the AToF Wall do not exactly match because the AToF efficiency for hydrogen isotopes in this energy range is lower than that of the CHIMERA modules.

With beam intensities of about 10^5 pps and targets of 1-2% interaction probability, about $5 * 10^6$ events were collected for each system. Special runs were performed with and without target, in order to measure the background from interaction of projectile ions with air, and with iron shadow bars in front of LAND for the neutron background measurement.

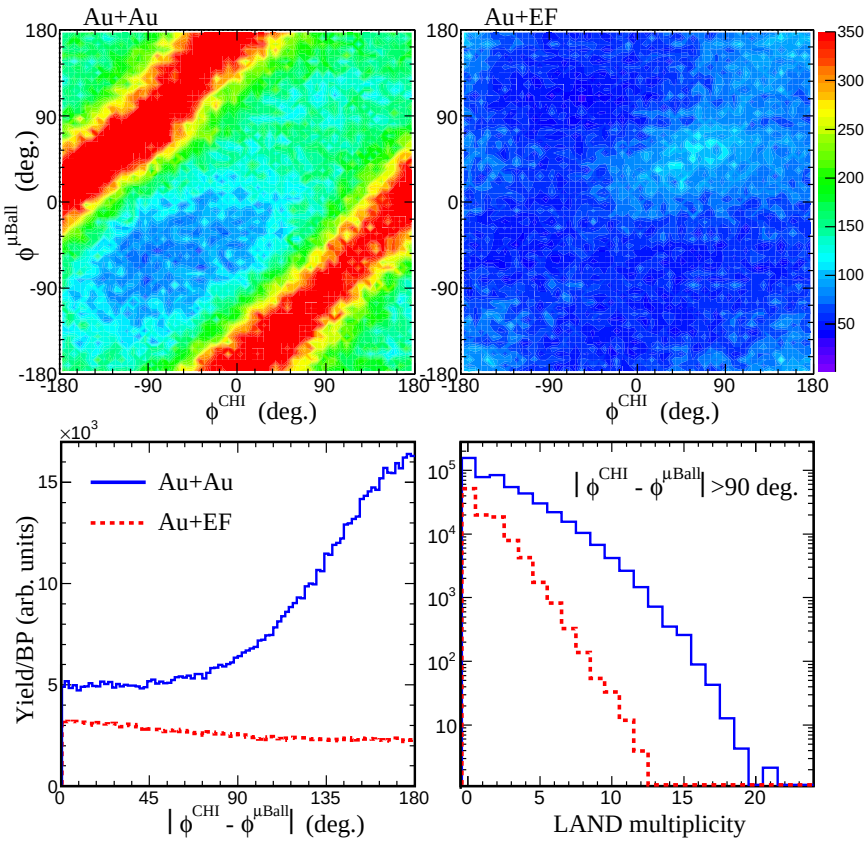

Fig. 3: Top row: Correlation between the Q-vector orientations determined with CHIMERA (abscissa) and with the Microball (ordinate) for data sets taken with (left panel) and without (right panel) a target foil in place (EF = Empty Frame). Bottom row: difference of the Q-vector orientations for Au+Au and for Au+EF data (left panel), normalized with respect to the integrated beam intensity (BP stands for beam particles), and the raw hit multiplicities (right panel) registered with LAND for Au+Au (full line) and for Au+EF data sets (dotted).

DATA ANALYSIS

For rejecting background reactions due to the interaction of Au projectiles with non-target material (mainly air), the correlation of the two reaction plane orientations given by CHIMERA and by the Microball detectors, was used, as shown in fig. 3. From the Microball data, the reaction plane orientation has been estimated by averaging over the azimuthal directions of the recorded hits, i.e. by calculating a $\vec{Q}$ vector (see Ref. [13] for definition) as $\vec{Q} = \sum_{i=1}^{N} \hat{r}_t^i$, where $\hat{r}_t^i$ is the azimuthal unit vector in the direction of the location of the detector module that recorded the i^{th} hit and $N \geq 2$. For CHIMERA, the $\vec{Q}$ vector has been calculated as $\vec{Q} = \sum_{i=1}^{N} Z^i \beta_t^i \gamma^i$, with $N \geq 4$, taking only the forward emitted particles with rapidity in the center of mass reference frame $y_i^{CM} > 0.1$.

Figure 3 shows the correlation between CHIMERA and Microball reaction plane orientations for Au+Au reactions (top left panel) and Au+Empty Frame (top right panel) data, normalized to each other according to the integrated beam intensity. In top left panel, the strong anti-correlation for on-target reactions is evident, as expected because CHIMERA covers the forward and the Microball mainly the backward hemispheres in the c.m. frame. In runs with empty target frames, the recorded yields are low and only a weak positive correlation is observed. The difference between the two reaction plane orientations, normalized with respect to the integrated beam intensity, is presented in bottom left panel. In order to minimize the contributions of non-target collisions in the data analysis, an anti-correlation of the CHIMERA and Microball reaction-plane orientations was required. The condition $|\Phi_{RP}^{CHI} - \Phi_{RP}^{\mu Ball}| > 90^\circ$ was applied, resulting in a relative weight of background reactions of less than 20%. This clearly shows the relevance of the Microball data in rejecting background reactions.

Bottom right panel of Fig. 3 shows the LAND raw multiplicity (number of fired paddles) normalized with respect to the integrated beam intensity for Au+Au and Au+no target data, after applying the indi-

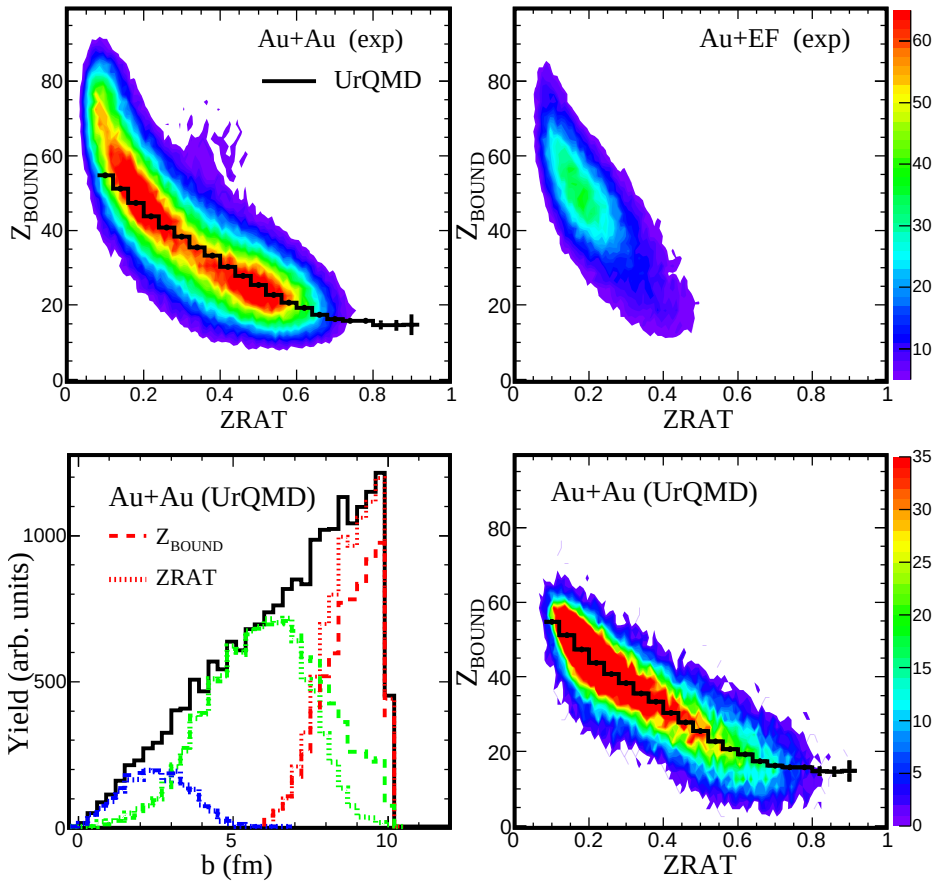

Fig. 4: Top row: Z_{BOUND} vs. $ZRAT$ correlation for data sets taken with (left panel) and without (right panel) a target foil in place (EF = Empty Frame). Bottom row: UrQMD calculations for the correlation of Z_{BOUND} vs. $ZRAT$ for Au+Au collisions at 400 MeV/nucleon and impact parameter b $<$ 10 fm, filtered to match the experimental conditions (right panel), and for impact-parameter distributions obtained under different conditions (left panel). The unbiased distribution for the full reaction for b $<$ 10 fm is given by the black histogram while the blue, green, and red lines show impact parameter distributions obtained when selecting b $<$ 3 fm, 3 $<$ b $<$ 7.5 fm, and b $>$ 7.5 fm, respectively, by gating on either Z_{BOUND} (dashed) or on $ZRAT$ (dotted). The ridge line of the UrQMD distribution (bottom right) is drawn into the experimental distribution (top left).

cated CHIMERA-Microball anticorrelation condition. The contribution from non-target backgrounds in the kinematic region of LAND is apparently rather weak.

For the impact parameter selection global variables were constructed from the CHIMERA and AToF data. They included $Z_{BOUND} = \sum_{i=1}^{N} Z^i$ with $Z^i \geq 2$ and the ratio of transverse to longitudinal charge, $ZRAT = 10 * Z_{Trans}/Z_{Long}$, where $Z_{Trans} = \sum_{i=1}^{N} Z_i * sin^2(\theta_i)$, $Z_{Long} = \sum_{i=1}^{N} Z_i * cos^2(\theta_i)$ and θ_i is the polar angle of the i^{th} particle in the laboratory reference system. The choice of such variables as impact parameter selectors has been guided by UrQMD calculations for given impact parameter ranges, filtered for angular acceptance, detection thresholds and resolution of the detectors.

The Z_{BOUND} vs. $ZRAT$ correlation plot for Au+Au reactions is presented in top left panel of Fig. 4. A strong anti-correlation is found between the two global variables, the smaller Z_{BOUND}, the larger $ZRAT$ and, according to UrQMD calculations, the smaller the impact parameter. The same correlation for Au+no target data is shown in top right panel and the corresponding correlation predicted by the UrQMD model for Au+Au reactions with impact parameter b <10 fm is presented in bottom right panel. There is good qualitative agreement between the experimental data and the calculations. In top left and bottom right panel the UrQMD predicted $\langle Z_{BOUND} \rangle$ vs. $ZRAT$ correlations is shown by full black line. The impact parameter intervals obtained by gating on specific Z_{BOUND} and/or $ZRAT$ intervals are shown in bottom left panel of Fig. 4.

An important parameter for flow studies is the resolution achieved in determining the azimuthal ori-

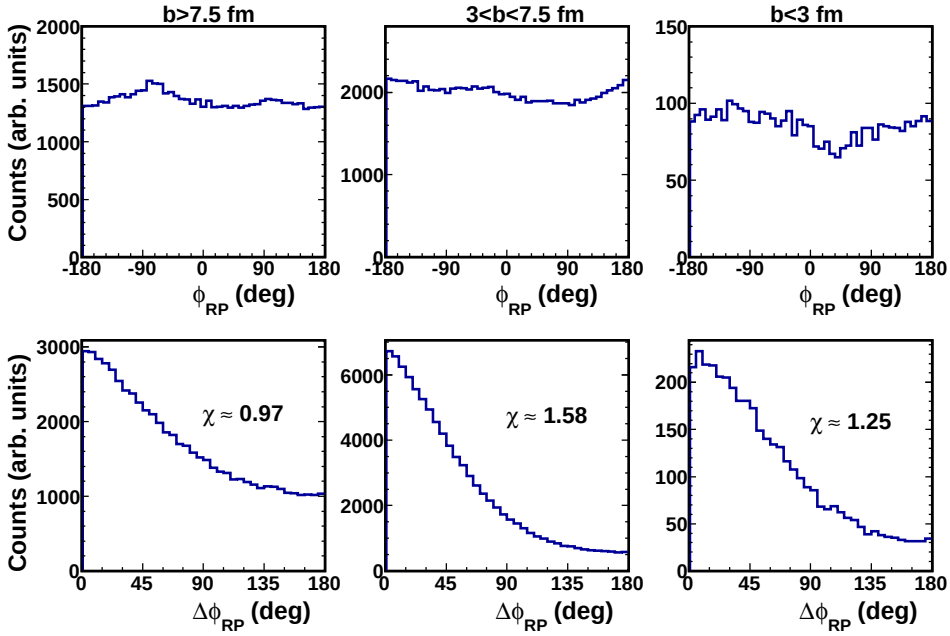

Fig. 5: Top row: Inclusive distribution of reaction-plane orientations obtained with the Q-vector method from the combined CHIMERA and AToF data for the indicated three intervals of nominal impact parameter b. Bottom row: Distributions of the difference of orientations of the sub-event reaction planes obtained with the mixing technique of [15, 16]. The corresponding values of the reaction plane dispersion parameter χ are indicated.

entation of the reaction plane that largely determines the uncertainty associated with the determined flow parameters [14]. The reaction plane distribution as obtained by merging CHIMERA and AToF data, for different selections of impact parameter window, is shown in 1^{st} row of Fig. 5; the flatness indicates that the particle angular distributions have not been biased by the event triggering in the experiment. We also tested the resolution achieved in reconstructing the reaction plane using the sub-event mixing technique of Ref. [15, 16]. The distribution of the difference between the two reaction plane orientations extracted by the sub-events is reported in the 2^{nd} row of Fig. 5. The analysis performed so far shows that the reaction plane orientation achieved with the CHIMERA and AToF modules is well suited for the experiment's aim. Using the method of [15] we have estimated reaction plane dispersion parameter χ and correction factors for the Fourier parameters of the azimuthal distribution, i.e. v_1 and v_2 attenuation factors.

ELLIPTIC NEUTRON AND CHARGED-PARTICLE FLOWS

Azimuthal distributions of neutrons and light charged particles measured with LAND with respect to the reaction plane given by CHIMERA have been extracted for Au+Au reactions from runs with and without the shadow bar. After subtracting the background, the obtained distributions have been fitted with formula (1) of Ref. [1] in order to determine the direct (v_1) and elliptic (v_2) flow coefficients. Due to insufficient energy resolution in the LAND veto-wall, charge identification with the ΔE-vs.-time-of-flight technique has not been possible. Therefore, the results for neutrons and for all recorded charged particles (Ch) are presented. The v_1 and v_2 parameters for Ch and neutrons as functions of the transverse momentum p_t/A are shown in Fig. 6. In the same figure, also the UrQMD predictions for a soft (γ=0.5) and a stiff (γ=1.5) symmetry energy potential [1] are given.

Constraints for the symmetry energy were determined as in Ref. [1] by comparing the ratios of the elliptic flows of neutrons and Ch, v_2^n/v_2^{Ch}, with the corresponding UrQMD predictions for the soft and stiff cases. The results obtained as functions of the transverse momentum p_t/A are shown in Fig. 7. A preliminary value for the power-law coefficient γ, deduced by linearly interpolating between the predictions, is $\gamma = 0.75 \pm 0.10$. The new constraint is compatible with the previous one presented in Ref. [1] by using FOPI-LAND data and the same UrQMD model but the statistical error has been significantly reduced by a factor of ~ 2. The determination of systematic uncertainties is still on-going; a preliminary analysis indicates that they are substantial and may lead to an overall final uncertainty of the order of $\Delta\gamma \approx \pm 0.20$.

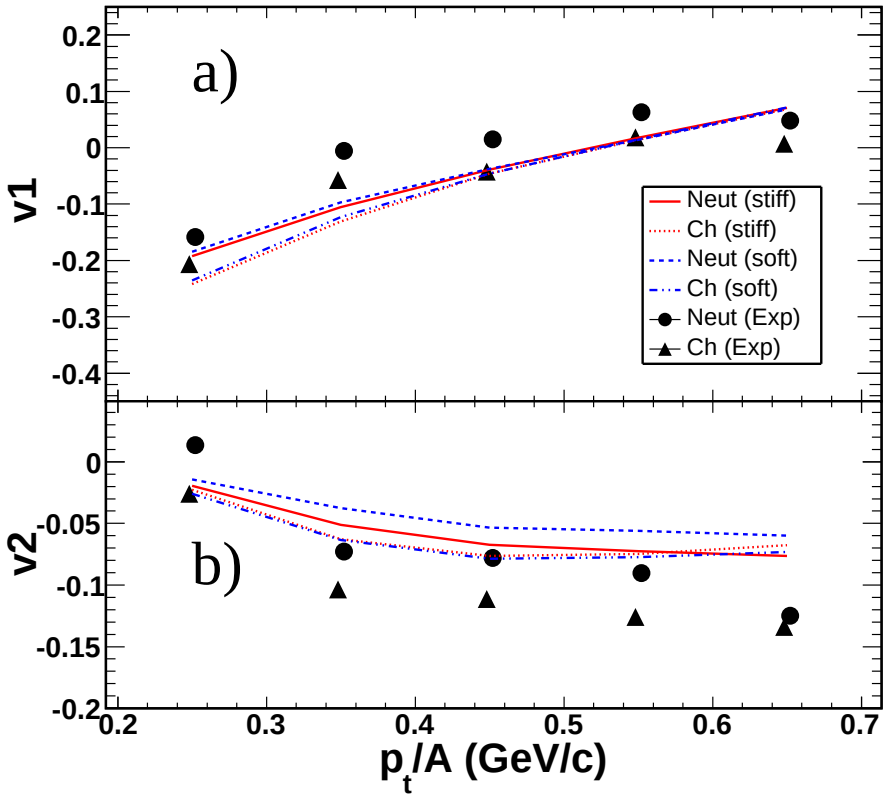

Fig. 6: Measured flow parameters v_1 (top) and v_2 (bottom) for impact parameter b < 7.5 fm in Au+Au collisions at 400 MeV/nucleon for neutrons (black full dots) and charged particles (black full triangles) as a function of the transverse momentum p_t/A. The UrQMD predictions for neutrons and charged particles obtained with a stiff ($\gamma = 1.5$, red full and dotted lines, respectively) and a soft ($\gamma = 0.5$, blue dashed and dash-dotted lines, respectively) density dependence of the symmetry term have been filtered to correspond to the geometrical acceptance of the experiment. The experimental data have been corrected for the dispersion of the reaction-plane orientation.

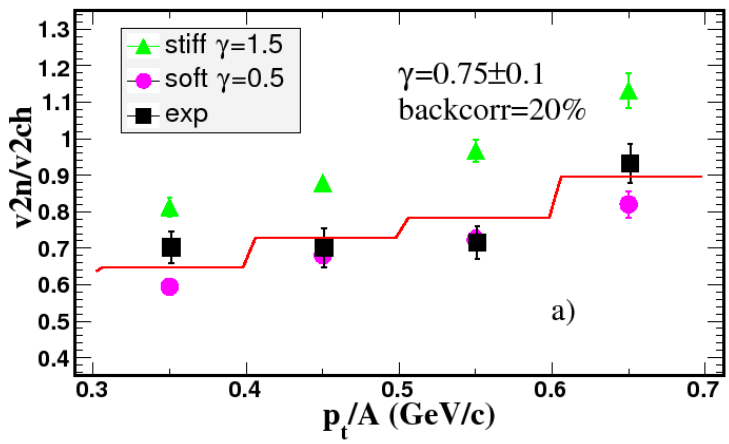

Fig. 7: Elliptic flow ratio of neutrons and charged particles for moderately central ($b < 7.5$ fm) collisions as a function of the transverse momentum per nucleon p_t/A, evaluated for a given analysis condition. The full squares represent the experimental data, the triangles and dots represent the UrQMD predictions for stiff (γ=1.5) and soft (γ=0.5) power-law exponent of the potential term. The full line is the result of a linear interpolation between the predictions, leading to the indicated γ=0.75±0.10.

CONCLUSIONS

Comparisons of the experimental data with other theoretical transport models will be useful in order to pursue the route towards a model-independent constraint of the high-density symmetry energy initiated in Ref. [6]. The promising preliminary results of the present experiment may also be seen as an encouragement for extending the measurement of neutron and charged particle flows to other reaction systems and energies. Future experiments may thereby benefit from the unique possibilities offered by the NeuLAND detector presently constructed as part of the R^3B experimental set-up [17] and from the availability of radioactive ion beams for reaction studies at FAIR.

ACKNOWLEDGMENT:
This work has been supported by the European Union under contract No. FP7-25431 (Hadron-Physics2).

REFERENCES

[1] P. Russotto et al., Phys. Lett. B **697**, 471 (2011).
[2] M.D. Cozma, Phys. Lett. B **700**, 139 (2011).
[3] P. Russotto et al., Eur. Phys. J. A **50**, 38 (2014), and refs. therein.
[4] Y. Leifels et al., Phys. Rev. Lett. **71**, 963 (1993).
[5] Q. Li et al., J. Phys. G **31**, 1359 (2005).
[6] M.D. Cozma et al., Phys. Rev. C **88**, 044912 (2013).
[7] Th. Blaich et al., Nucl. Instrum. Methods A **314**, 136 (1992).
[8] J. Łukasik et al., Nucl. Instrum. Methods A **709**, 120 (2013).
[9] J. Łukasik et al., EPJ Web Conf. **88**, 01017 (2015); S. Kupny et al., ibidem 01010.
[10] A. Schüttauf et al., Nucl. Phys. A **607**, 457 (1996).
[11] D.G. Sarantites et al., Nucl. Instrum. Methods A **381**, 418 (1996).
[12] A. Pagano et al., Nucl. Phys. A **734**, 504 (2004).
[13] P. Danielewicz and G. Odyniec, Phys. Lett. B **157**, 146 (1985).
[14] A. Andronic et al., Eur. Phys. J. A **30**, 31 (2006).
[15] J.-Y. Ollitrault, preprint nucl-ex/9711003.
[16] J.-Y. Ollitrault, Nucl. Phys. A **638**, 195c (1998).
[17] https://www.gsi.de/r3b

Dynamical microscopic calculations of low and intermediate energy fission within the CoMD (Constrained Molecular Dynamics) model

G.A. Souliotis[1,*], N. Vonta[1,†], M. Veselský[2,‡] and A. Bonasera[3,4,§]

[1]Laboratory of Physical Chemistry, Department of Chemistry, National and Kapodistrian University of Athens, Athens 15771, Greece
[2]Institute of Physics, Slovak Academy of Sciences, Dúbravská cesta 9, 845 11 Bratislava, Slovakia
[3]Cyclotron Institute, Texas A&M University, College Station, Texas 77843, USA
[4]Laboratori Nazionali del Sud, INFN, via Santa Sofia 62, I-95123 Catania, Italy

Abstract

The microscopic description of nuclear fission is a topic of current experimental and theoretical interest. In this work, we performed a systematic study of low and intermediate energy fission calculations using the Constrained Molecular Dynamics (CoMD) code. The code implements an effective interaction with a soft isoscalar part and with several forms of the density dependence of the nucleon symmetry potential. In addition, CoMD imposes a constraint in the phase space occupation for each nucleon, restoring the Pauli principle at each time step of the evolution of the nuclear system. Proper choice of the surface parameter of the effective interaction has been made to describe fission. In this work, we present CoMD calculations for several proton-induced fission reactions at low and intermediate energy and compare them with recent experimental data. We found that CoMD is able to describe the many-body dynamics of the fission process especially for intermediate and higher-energy fission reactions.

INTRODUCTION

Understanding of the mechanism of nuclear fission, apart from the theoretical many-body point of view, is of practical importance for energy generation, isotope production, as well as for the transmutation of nuclear waste. Moreover, nuclear fission is the process that defines the upper limit of the periodic table of the elements and plays a vital role in the production of heavy elements via the astrophysical r-process [1]. Motivated by the present state of affairs regarding fission, we performed a systematic study of low and intermediate energy fission using the Constrained Molecular Dynamics (CoMD) code [2, 3].

THEORETICAL FRAMEWORK

The Constrained Molecular Dynamics (CoMD) code is based on the approach of molecular dynamics as applied to nuclear systems [4, 5]. The nucleons are assumed to be localized gaussian wavepackets in coordinate and momentum space. A simplified effective nucleon-nucleon interaction is implemented with a nuclear-matter compressibility of K=200 (soft EOS) with several forms of the density dependence of the nucleon-nucleon symmetry potential. In addition, a constraint is imposed in the phase space occupation for each nucleon, restoring the Pauli principle at each time step of the collision. Proper choice of the surface parameter of the effective interaction was made to describe fission.

In the calculations of the present work, the CoMD code was used essentially with its standard parameters. The soft density-dependent isoscalar potential was chosen (K=200). For the isovector part, several forms of the density dependence of the nucleon-nucleon symmetry potential are implemented. Two of them were used in the present work: the "standard" symmetry potential [red (solid) lines] and the "soft" symmetry potential [blue (dotted) lines] in the figures that follow. These forms correspond to a dependence of the symmetry potential on the 1 and the 1/2 power of the density, respectively. The surface term of the potential was set to zero to describe fission. For a given reaction, a total of approximately 5000 events were collected. For each event, the impact parameter of the collision was chosen in the range b = 0–6 fm, following a triangular distribution. Each event was followed up to 15000 fm/c and the phase space coordinates were registered every 50 fm/c. At each time step, fragments were recognized with the minimum spanning tree method [2, 3], and their properties were reported. Thus, information on the evolution of the fissioning system and

*Corresponding author. E-mail: souliotis@chem.uoa.gr
†E-mail: nikolettav@chem.uoa.gr
‡E-mail: Martin.Veselsky@savba.sk
§E-mail: abonasera@comp.tamu.edu

the properties of the resulting fission fragments were obtained. In this way, the moment of scission of the deformed heavy nucleus could be determined. We allowed 2000 fm/c after scission for the nascent fission fragments to deexcite and we reported and analyzed their properties.

RESULTS AND COMPARISONS

Guided by the present literature concerning the nuclear fission of uranium isotopes, we performed calculations of proton induced fission of ^{235}U, at 10 MeV, 30 MeV, 60 MeV and 100 MeV. Moreover, calculations have been performed for the proton induced fission of ^{238}U, at 100 MeV and 660 MeV energies.

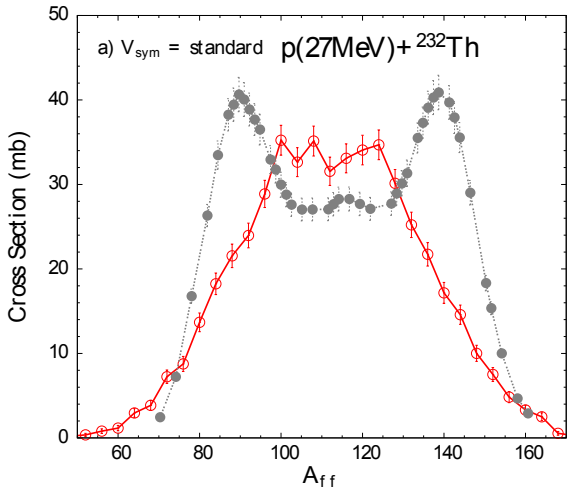

Fig. 1: Normalized mass distributions (cross sections) of fission fragments from p (27 MeV) + ^{232}Th. Full points (grey): experimental data [6]. Open points: CoMD calculations with the standard symmetry potential.

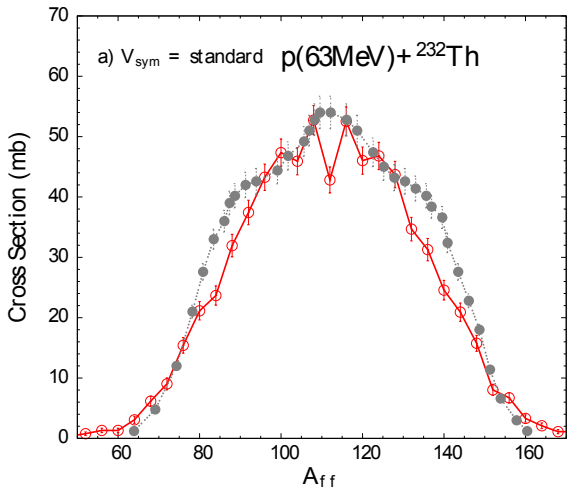

Fig. 2: (Color online) Normalized mass distributions (cross sections) of fission fragments from p (63 MeV) + ^{232}Th. Full points (grey): experimental data [6]. Open points: CoMD calculations with the standard symmetry potential.

In Fig. 1, in the experimental data of the reaction p (27 MeV) + ^{232}Th, we observe the asymmetric nature of the fission of ^{232}Th. In contrast, the CoMD calculations result in a symmetric distribution with a flat top. The main reason is that the nucleon-nucleon interaction in the CoMD model does not include spin dependence, and thus the resulting mean field potential has no spin-orbit contribution. Consequently, the model cannot reproduce the shell effects necessary to describe the asymmetric low-energy fission of ^{232}Th.

When the proton energy increases (Fig. 2), it is expected that the shell effects will fade and the fissioning

system will preferentially undergo symmetric fission. The mass yields for the same reaction at proton energy 63 MeV is presented. The experimental mass yield becomes more symmetric at this energy and the calculated yield curve is in better agreement with the data.

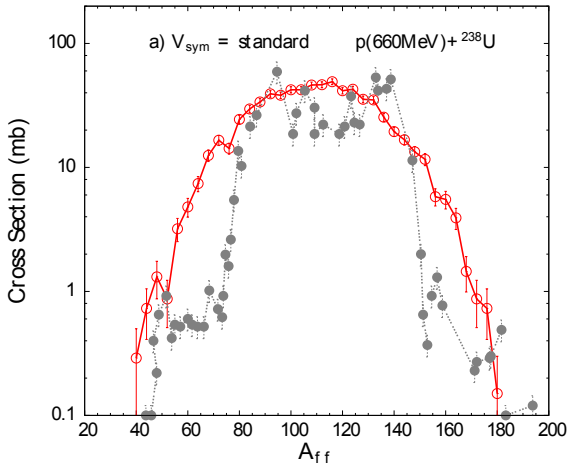

Fig. 3: (Color online) Normalized mass distributions (cross sections) of fission fragments from p (660 MeV) + ^{238}U. Full points (grey): experimental data [7, 8, 9]. Open points: CoMD calculations with the standard symmetry potential.

In Fig. 3, the mass distribution of proton induced fission of ^{238}U at 660 MeV is presented and it is in good agreement with the experimental data [7, 8, 9]. We observe mostly the symmetric fission mode, due to washing-out of the shell effects. Moreover, the calculations describe satisfactorily the superasymmetric fission, which has been experimentally seen at fission fragment masses ∼40–80 and ∼140–180.

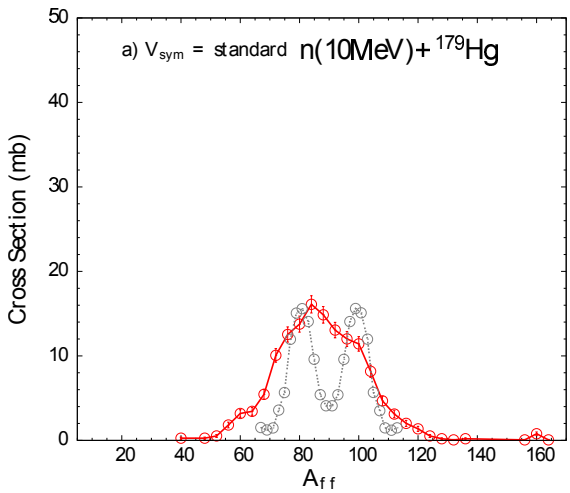

Fig. 4: (Color online) a) Normalized mass distributions (cross sections) of fission fragments from n (10 MeV) + ^{179}Hg. Full points (grey): experimental data [10, 11]. Open points: CoMD calculations with the standard symmetry potential.

In Fig. 4, we present the mass distribution for the neutron induced fission of ^{180}Hg at 10 MeV. The experimental data [10, 11] are compared with the calculations. The work of [11] introduces a new type of asymmetric fission in proton-rich nuclei. It is related to the exotic process of β-delayed fission of ^{180}Tl. The experimental data represent the fission fragment mass distribution of the β-decay daughter nucleus ^{180}Hg, which is asymmetric. The asymmetric nature is surprising due to the fact that the nucleus ^{180}Tl is expected to be divided into two fragments of ^{90}Zr, with magic number of neutrons N=50 and semi-magic of protons Z=40, which are supposed to be more stable. In the experimental data, the asymmetric nature of the fission is obvious. On the contrary, the CoMD calculations cannot describe correctly the shell effects and for this reason, the distribution is symmetric.

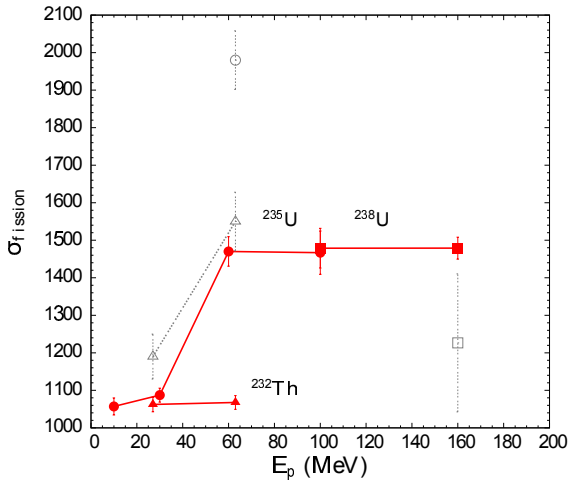

Fig. 5: (Color online) Calculated total fission cross section with respect to proton energy E_p. The CoMD calculations are carried out with the standard symmetry potential and are shown with full (red) symbols connected with full (red) lines. The reactions are indicated as follows: triangles: p (27, 63 MeV) + ^{232}Th, circles: p (10, 30, 60, 100 MeV) + ^{235}U, squares: p (100, 660 MeV) + ^{238}U. Some experimental data are shown with open symbols as follows: triangles: p (27, 63 MeV) + ^{232}Th [6], circles: p (60 MeV) + ^{235}U [12], square: p (660 MeV) + ^{238}U [8, 9]. The point at E_p=660 MeV is displayed at E_p=160 MeV.

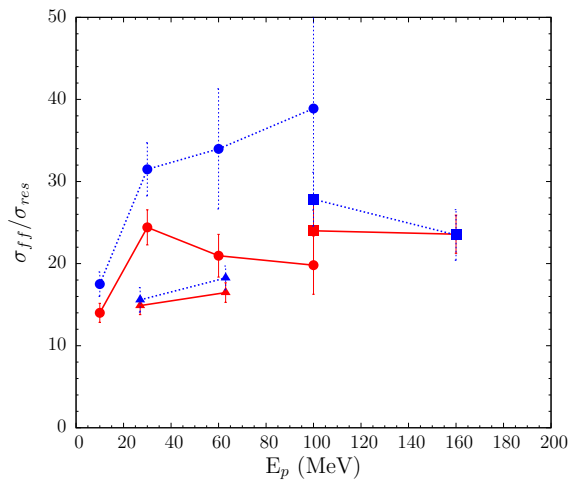

Fig. 6: (Color online) Calculated ratio of the fission cross section over residue cross section with respect to proton energy. CoMD calculations with the standard symmetry potential are with full (red) symbols connected with full (red) lines. Calculations with the soft symmetry potential are with full (blue) symbols connected with dotted (blue) lines. The reactions are indicated as follows: triangles: p (27, 63 MeV) + ^{232}Th, circles: p (10, 30, 60, 100 MeV) + ^{235}U, squares: p (100, 660 MeV) + ^{238}U. The points at E_p=660 MeV are displayed at E_p=160 MeV.

Apart from the fission fragment mass distributions, we investigated other fission fragment properties. The results are mostly with the standard symmetry potential. For the following figures, the red closed circles represent the proton induced fission of ^{235}U at 10 MeV, 30 MeV, 60 MeV, 100 MeV. Moreover, the red closed squares represent the proton induced fission of ^{238}U at 100 MeV and 660 MeV, whilst the red closed triangles represent the proton induced fission of ^{232}Th at 27 MeV and 63 MeV. The blue points are with the soft symmetry potential. The experimental data are the open grey symbols (circles, squares and triangles) and they follow the same structure which has been adopted for the calculations.

The total fission cross section is presented in Fig. 5 in reference to the various proton energies for the proton induced fission of ^{232}Th, ^{235}U and ^{238}U. Concerning the fission of thorium, we observe that increasing the excitation energy there is only a slight increase. However, the experimental data show a jump of approximately 30%.

In Fig. 6, we present the correlation between the excitation energy and the ratio of the fission cross section over the residue cross section. For the fission of ^{232}Th we observe an increase in this ratio towards higher excitation energy. Hence, at 63 MeV beam energy, our calculations show higher probability for fission, in reference to the energy 27 MeV. Moreover, for the fission of the ^{235}U and ^{238}U, the probability of getting fission decreases at excitation energies, starting from 30 MeV to 100 MeV and from 100 MeV to 660 MeV respectively. Furthermore, a sensitivity of the calculations concerning the symmetry potential choice is depicted. For the soft potential choice, the aforementioned ratio increases and this means that this choice leads to an increasing probability of getting fission, especially for the proton induced fission of ^{235}U at various proton energies.

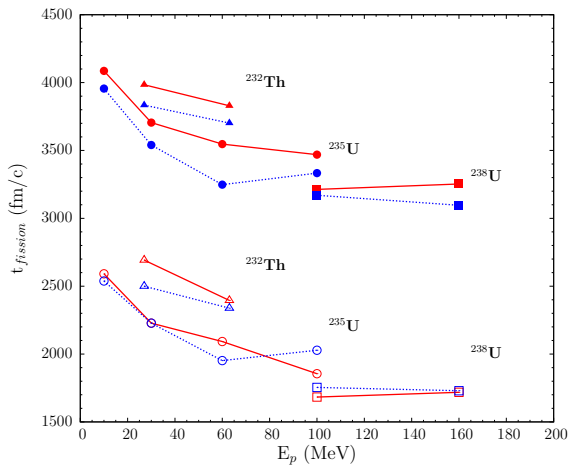

Fig. 7: (Color online) Calculated fission time with respect to incident proton energy. CoMD calculations with the standard symmetry potential are with (red) symbols connected with full (red) lines. Calculations with the soft symmetry potential are with (blue) symbols connected with dotted (blue) lines. The full symbols (upper half of the figure) are with the full ensemble of the fissioning nuclei, whereas the open symbols (lower half) are with the selection of the fissioning system not to emit any pre-scission protons (see text). The reactions are as follows: triangles: p (27, 63 MeV) + ^{232}Th, circles: p (10, 30, 60, 100 MeV) + ^{235}U, squares: p (100, 660 MeV) + ^{238}U. The points at E_p=660 MeV are displayed at E_p=160 MeV.

It is very difficult to estimate the fission time from experimental data. Because of the fact that the CoMD is a dynamical microscopic code, we can naturally obtain the dynamical path of the process and therefore determine the fission time. In Fig. 7, the fission time is plotted versus the proton energy of the indicated reactions. We performed the calculations under the restrictions that the fissioning system be a) Z=91, for ^{232}Th b) Z=93, for ^{235}U and ^{238}U, which are represented by the open circles, squares and triangles (open symbols). Moreover, the closed symbols refer to the CoMD calculations where the full ensemble of the fissioning nuclei is taken into account. For this ensemble, we noticed that the code emits on average two pre-scission protons. The general trend is that the fission time decreases with the increase of the excitation energy. We observe that the open symbols are lower than the closed ones. The general trend shows that the fission time decreases when the proton energy increases. Additionally, the choice of Z for the fissioning system leads to a decrease of the fission time. When this choice is made, the total Coulomb energy is larger (since no pre-scission protons are emitted) and thus, the fissioning system is more fissionable.

After the above detailed discussion of CoMD observables, we conclude our presentation by examining the evolution of the interaction and kinetic energies of fissioning nuclei in their course toward scission.

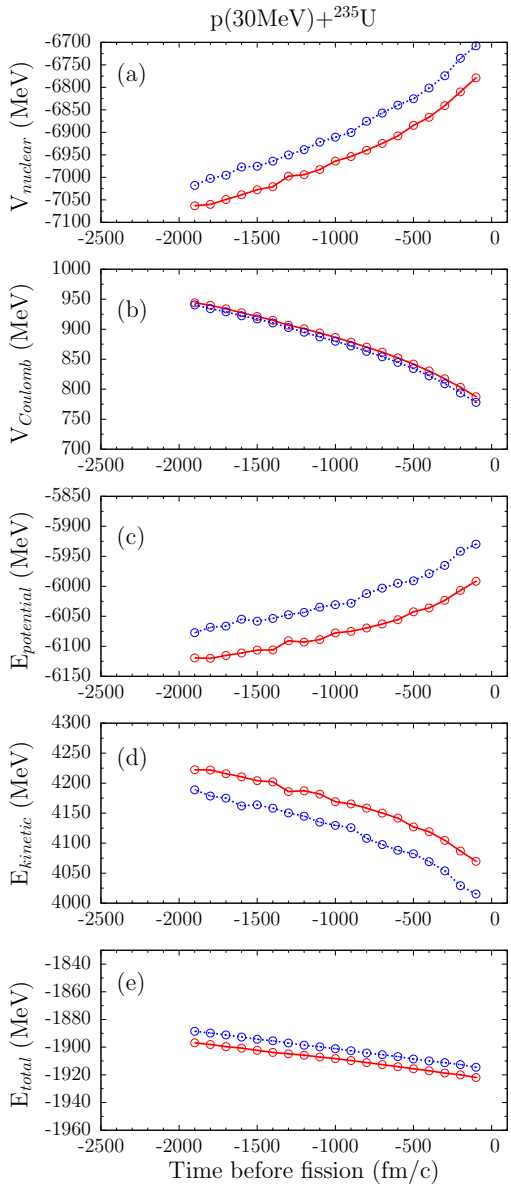

Fig. 8: (Color online) Evolution of ensemble average CoMD energies of fissioning nuclei in the interaction of p(30 MeV) with ^{235}U. The moment of scission is taken as t=0 fm/c. (Red) points connected with solid lines are with the standard symmetry potential. (Blue) points connected with dotted lines are with the soft symmetry potential. The energies are: a) Nuclear potential energy (the sum of the two-body interaction energy, the three-body interaction energy, the surface energy and the symmetry energy). b) Coulomb potential energy. c) Total potential energy [sum of energies of (a) and (b)]. d) Kinetic energy. e) Total energy [sum of (c) and (d)].

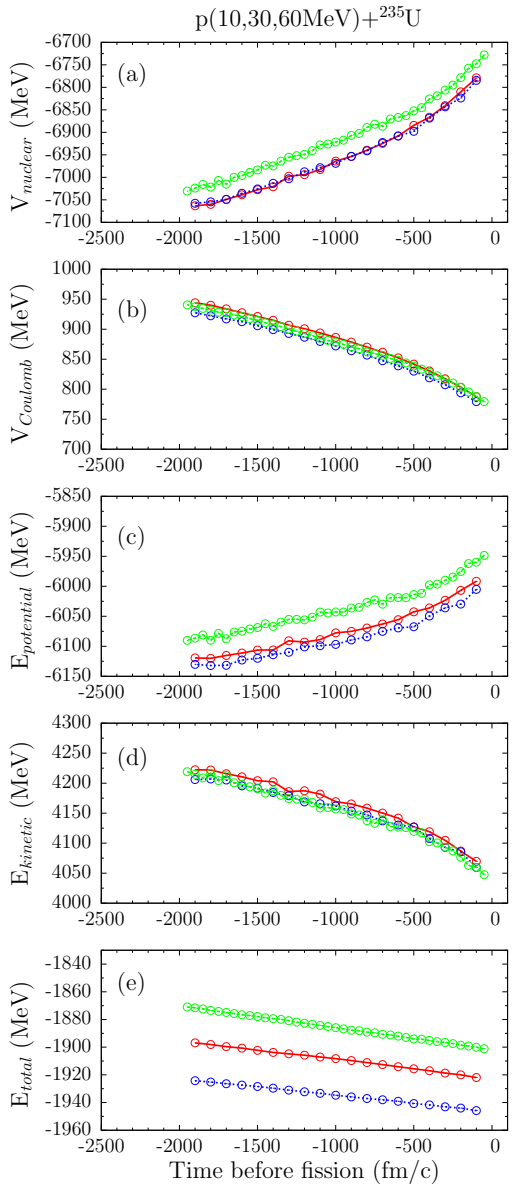

Fig. 9: (Color online) Evolution of ensemble average CoMD energies of fissioning nuclei in the interaction of p with ^{235}U. The reactions are with: 10 MeV protons: (blue) points connected with dotted line, 30 MeV protons: (red) points connected with solid line, 60 MeV protons: (green) points connected with dashed line. The moment of scission is taken as t=0 fm/c. The calculations are with the standard symmetry potential. The energies are: a) Nuclear potential energy (the sum of the two-body interaction energy, the three-body interaction energy, the surface energy and the symmetry energy). b) Coulomb potential energy. c) Total potential energy [sum of energies of (a) and (b)]. d) Kinetic energy. e) Total energy [sum of (c) and (d)].

As a representative example, we show in Fig. 8 the results for the reaction p(30MeV)+^{235}U for the standard symmetry potential [(red) points connected with solid line] and the soft symmetry potential [(blue) points connected with dotted line]. In order to examine the evolution of the average energies in the course to scission, and given the broad distribution of fission times (as seen in Fig. 7), in Fig. 8 the time is referenced with respect to the moment of scission, taken to be at t=0 fm/c.

In Fig. 8a, the event-average nuclear interaction energy is presented, taken to be the sum of the two-body, three-body, surface and symmetry energy terms. An overall increase of the interaction energy is observed as the fissioning system approaches the moment of scission, for both the standard and the soft symmetry potentials. Interestingly, the calculation with the soft symmetry potential results in higher interaction energy of the fissioning system, as can be understood by the overall larger nuclear symmetry energy in the low-density neck region, and the overall more repulsive dynamics implied. In Fig. 8b, the total Coulomb energy is presented, being nearly the same for the two choices of the symmetry potential (only slightly lower for the soft symmetry potential, since as we discussed, it results in more elongated configurations). A monotonic decrease of the Coulomb energy is observed as the fissioning system evolves toward scission, this decrease being essentially the main driving force of the nuclear system to fission.

In Fig. 8c, the total potential energy of the fissioning system, namely the sum of the nuclear interaction energy and the Coulomb energy, is shown. In Fig. 8d, the kinetic energy of the fissioning system is shown, being lower for the soft symmetry potential, that also results in higher potential energy (Figs. 8a, 8c) involving more elongated configurations and more repulsive dynamics in the low-density neck region. Finally, in Fig. 8e, the total energy of the fissioning system is shown, being slightly higher for the soft symmetry potential. The decrease with time is due to the prescission emission of neutrons and protons.

In Fig. 9, we show the variation of the energies of the fissioning system p+^{235}U with respect to the change of the incident proton energy from 10 MeV [(blue) points connected with dotted line] to 30 MeV [(red) points connected with solid line] to 60 MeV [(green) points connected with dashed line]. The calculations are with the standard symmetry potential. In Fig. 9a, we observe that with proton energies of 10 and 30 MeV, the average nuclear interaction energy of the fissioning systems is nearly similar. The Coulomb energy (Fig. 9c) and the kinetic energy (Fig. 9d) increase in going from 10 to 30 MeV proton energy. It appears that the additional proton energy brought in the fissioning system is stored as kinetic energy (Fermi motion) and Coulomb energy. This increase is reflected in the total energy (Fig. 9e).

Interestingly, in going from 30 to 60 MeV proton energy, we observe that the nuclear interaction energy is increased by nearly this amount of energy (about 30 MeV), whereas the Coulomb energy is nearly the same. The kinetic energy decreases slightly, which is rather counterintuitive: we would expect an increase in the kinetic energy as we saw in going from 10 to 30 MeV proton energy. Thus, for the case of 60 MeV protons, the additional amount of energy brought in by the proton is stored as nuclear potential energy, indicating that essentially above the Fermi energy, the nuclear (mean-field) potential energy is effectively momentum depend. The origin of this momentum dependence is in the Pauli correlations imposed by the CoMD procedure, i.e. the phase-space constraint imposed by CoMD to ensure the Fermionic behavior of the classically evolving system of Gaussian wave packets. The total energy for the case of 60 MeV protons (Fig. 9e) is consistently above that of the previous two energies and has a diminishing behavior with time toward scission due to the emission of prescission particles, as in the other two energies.

The above examination of the CoMD energy variations of the fissioning system provides a good check of the consistency and accuracy of the code, as applied to the description of a deforming system as it evolves toward scission. We wish to point out that from the present calculations we cannot obtain information regarding the fission barriers of the involved fissioning nuclei. The reason is that the calculations are performed at high enough energy, so that the fissioning systems are above the fission barrier expected to be near 6–8 MeV. In order to obtain average fission barriers with CoMD, a different methodology has to be followed: the total energy of a fissioning nucleus has to be obtained as a function of deformation, placing the nucleus into a deformed harmonic potential. This interesting project, however, requires further computational effort that we plan to undertake in the future.

DISCUSSION AND CONCLUSIONS

In the present study, we employed the semi-classical microscopic code CoMD to describe mostly proton induced fission, in a variety of energies on ^{232}Th, ^{235}U and ^{238}U nuclei. We chose these nuclei because of the availability of recent literature data and because of their significance in various applications of fission. We found that the CoMD code in its present implementation is able to describe fission at higher energies where the shell effects are of little significance. We note that the effective nucleon-nucleon interaction employed in the code has no spin dependence and thus the resulting mean field has no spin-orbit contribution. We are exploring possibilities of adding such a dependence on the potential to give us the ability to describe the

characteristics of low energy fission.

We found that the total fission cross sections were rather well reproduced and the ratio of total fission cross sections over residue cross sections appears satisfactory. Interestingly, this ratio shows a sensitivity on the choice of the symmetry potential. Concerning the mean total energies and the neutron multiplicities, we mention that they are rather adequately reproduced [13]. Finally, information on the fission time scale is obtained from the present calculations. The obtained fission times show a dependence on the excitation energy of the fissioning nucleus, as well as on the choice of the symmetry potential.

In closing, the CoMD code gives results that are not dependent on the specific dynamics being explored and, thus, offers valuable predictive power for the different modes of fission without adjustable parameters. As such, the code can be used for the study of fission of either very neutron-rich or very neutron-deficient nuclei, which have not been studied experimentally to date. Furthermore, this possibility can be exploited to study the fission of very exotic nuclei related to the end point of the r-process, namely the process of fission recycling.

ACKNOWLEDGMENT:
We are thankful to M. Papa for his version of the CoMD code, and to Hua Zheng for his rewritten version of the CoMD. We wish to acknowledge the motivation and recent discussions on experimental aspects of fission with Y.K. Kwon and K. Tshoo of the KOBRA team of RISP. Financial support for this work was provided, in part, by ELKE Research Account No 70/4/11395 of the National and Kapodistrian University of Athens. M.V. was supported by the Slovak Scientific Grant Agency under contracts 2/0105/11 and 2/0121/14 and by the Slovak Research and Development Agency under contract APVV-0177-11.

REFERENCES

[1] J. Erler et al., Nature **486**, 509 (2012).
[2] M. Papa et al., Phys. Rev. C **64**, 024612 (2001).
[3] M. Papa et al, J. Comput. Phys. **208**, 403 (2005).
[4] A. Bonasera, F. Gulminelli, J. Molitoris, Phys. Rep. **243**, 1 (1994).
[5] J. Aichelin, Phys. Rep. **202**, 233 (1991).
[6] P. Demetriou et al., Phys. Rev. C **82**, 054606 (2010).
[7] A. Deppman et al., Phys. Rev. C **88**, 064609 (2013).
[8] G.S. Karapetyan et al., Phys. Atom. Nuclei **72**, 911 (2009).
[9] A.R. Balabekyan et al., Phys. Atom. Nuclei **73**, 1814 (2010).
[10] A.V. Andreev et al., Phys. Rev. C **88**, 047604 (2013).
[11] A.N. Andreyev et al., Phys. Rev. Lett. **105**, 252502 (2010).
[12] M.C. Duijvestijn et al., Phys. Rev. C **64**, 014607 (2001).
[13] N. Vonta, G.A. Souliotis, M. Veselsky, A. Bonasera, Phys. Rev. C **92**, 024616 (2015).

Opportunities for nuclear reaction studies at future facilities

Martin Veselský[1,*], Jozef Klimo[1], Nikoleta Vujisicová[2], and Georgios A. Souliotis[3,†]

[1]Institute of Physics, Slovak Academy of Sciences, Dúbravská cesta 9, 845 11 Bratislava, Slovakia
[2]Faculty of Electronics and Informatics, Slovak Technical University, Bratislava, Slovakia
[3]Laboratory of Physical Chemistry, Department of Chemistry, National and Kapodistrian University of Athens, and Hellenic Institute of Nuclear Physics, Athens 15771, Greece

Abstract

Opportunities for investigations of nuclear reactions at the future nuclear physics facilities such as radioactive ion beam facilities and high-power laser facilities are considered. Post-accelerated radioactive ion beams offer possibilities for study of the role of isospin asymmetry in the reaction mechanisms at various beam energies. Fission barrier heights of neutron-deficient nuclei can be directly determined at low energies. Post-accelerated radioactive ion beams, specifically at the future facilities such as HIE-ISOLDE, SPIRAL-2 or RAON-RISP can be also considered as a candidate for production of very neutron-rich nuclei via mechanism of multi-nucleon transfer. High-power laser facilities such as ELI-NP offer possibilities for nuclear reaction studies with beams of unprecedented properties. Specific cases such as ternary reactions or even production of super-heavy elements are considered.

INTRODUCTION

Progress in construction of advanced scientific infrastructure is a main driving force for progress in many fields of science, and this applies in particular to nuclear physics. Construction of still more powerful radioactive beam facilities allows to make spectacular progress in understanding of nuclear structure, and post-acceleration of radioactive beams allows also to perform nuclear reaction studies using unstable beams. Besides radioactive beam facilities, high-power lasers emerge as another driving force of the progress in nuclear physics. While many concepts still need to be verified in order to perform detailed nuclear physics studies, use of high-power lasers may allow various types of experiments of interest for production of exotic nuclei and for nuclear astrophysics. In this proceeding we consider several possible experiments and extensions of capabilities at both radioactive beam and high-power laser facilities.

(d,p)-transfer induced fission of heavy radioactive beams

Nuclear fission was discovered 70 years ago and represents one of the most dramatic examples of nuclear metamorphosis, whereby the nucleus splits into two fragments releasing a large amount of energy. Fission is not only important for applications such as the generation of energy and the production of radio-isotopes, but also has direct consequences on the synthesis of the heaviest elements in the astrophysical r-process, which is terminated by fission, and on the abundance of medium-mass elements in the universe through so-called "fission recycling" [1]. Furthermore, the fission process itself enables the study of nuclear-structure effects in the heaviest nuclei. Until recently the low energy fission was studied in the region from thorium to fermium using spontaneous fission, fission induced by neutrons and light stable beams or using beta-delayed fission. Recently, the probability of the electron-capture delayed fission of ^{178,180}Tl was measured at ISOLDE and a new asymmetric mode of fission was observed [2]. One of the open questions in fission is the height of the fission barriers of neutron-deficient nuclei. The region between lead and uranium is of special interest since around the closed neutron shell N=126 the fission barrier height is strongly influenced by shell structure, with direct implications to predictions of production of super-heavy nuclei, where fission barriers exist purely due to shell structure. Statistical model calculations, used to reproduce experimental evaporation residue cross sections in this region between lead and uranium, typically lead to extracted values of fission barrier heights in disagreement with theory, since available theoretical values [3, 4] need to be scaled down by 15–40 %. The measured beta-delayed fission probability was also used to deduce fission barrier height of the daughter isotope ^{180}Hg [5], and deduced fission barriers were again 10–40 % smaller than theoretical estimates. However, since ^{180}Hg (and other nuclei accessible in beta-delayed fission) is even-even nucleus, uncertainty remains concerning the magnitude of the pairing gap in saddle configuration and also concerning the extracted fission barrier height.

*E-mail: martin.veselsky@savba.sk
†E-mail: soulioti@chem.uoa.gr

The radioactive beams at the HIE-ISOLDE can be used to determine fission barrier heights of exotic heavy fissile nuclei. Possibilities to observe fission following the transfer reactions are investigated using the Talys code [6]. The estimates in the region between lead and uranium show that energy upgrade of the REX-ISOLDE post-accelerator to 4–5 AMeV will allow this type of low energy fission studies. Specifically, it is of interest to observe transfer-induced fission of odd elements such as Tl, Bi, At or Fr, since in this case the estimated fission barriers will not be influenced by uncertainty in estimation of the pairing gap in the saddle configuration, which is the case in beta-delayed fission. Due to this circumstance, use of odd-Z beams is preferential, allowing to observe fission of odd-odd nuclei, while use of even-Z beams may still allow to determine fission barriers of even-odd nuclei, still more preferential than in beta-delayed fission. It is possible to identify candidates for this type of measurement for each of considered isotopic chains. Figure 1 shows that fission cross sections for the ^{193}Tl radioactive beam increase dramatically when the fission barrier height is scaled down by 20 % (solid line) compared to standard values of fission barriers [3] (dashed line). The isotope ^{193}Tl appears especially suitable to determine the fission barrier due to steep increase of the excitation function and eventual availability of sufficient yield from the ISOL target. In similar way, the beams of nuclei ^{199}Bi, ^{201}At and ^{209}Fr can be identified in analogous systematic estimates of fission cross sections of corresponding odd elements. The observed fission rates of these beams can be used to determine values of the fission barrier heights.

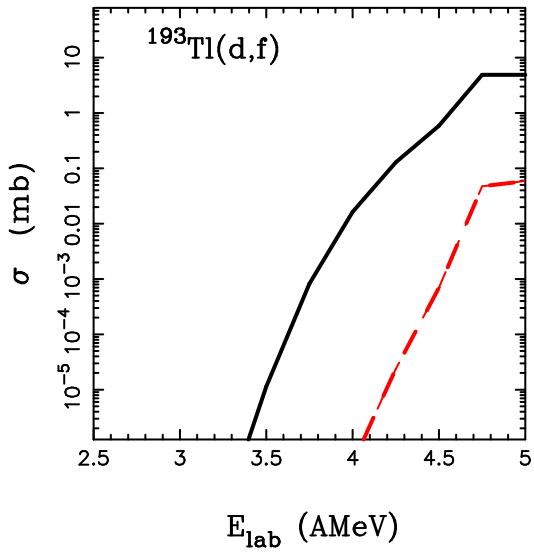

Fig. 1: Fission cross sections for the radioactive beam ^{193}Tl, calculated with and without reduction of fission barrier [3] by 20 % (solid and dashed line, respectively). Strong sensitivity to fission barrier height offers possibility to determine it experimentally.

Measurement at HIE-ISOLDE will be performed using the active target ACTAR TPC [7], a time-projection chamber (TPC) filled with the target (deuterium) gas. The use of ACTAR TPC offers several advantages, namely higher observed fission rates and the possibility of obtaining the fission cross sections for a range of beam energies in one measurement. As an example, using deuterium gas with pressure 250 mbar, one obtains an effective target thickness 1.6 mg/cm^2 of deuterium. Assuming a target chamber length parallel to beam axis of about 20 cm (corresponding to the dimensions of ACTAR TPC demonstrator), the beam would slow down from the initial energy of 5 AMeV to about 4.1 AMeV. This interval essentially covers the range of interest in the case of transfer-induced fission of ^{193}Tl. In ACTAR TPC the reaction vertex can be reconstructed with a resolution better than 3 mm, allowing to measure more than 60 points of the excitation function over the energy range of interest. For these points, a rate ranging from about two events/minute at highest beam energy down to one event per hour for the lowest energy can be calculated from the amount of target material in the corresponding slice, the beam intensity (10^6 pps) and a calculated cross section, with the fission barrier reduced by 20 %. Integrated over the whole chamber, with average cross section around 2 mb over the entire energy range, the fission rate can be estimated to twenty per minute. Without reduction of the fission barrier, the expected fission rate can be still estimated to some tens of fissions per hour. Thus the use of active target ACTAR TPC provides the needed sensitivity, allowing to resolve the long-standing question concerning the observed fission barriers of proton-rich nuclei by way of their direct measurement. Observed fission rates will determine how detailed the investigations of the low energy fission

will be. Understandably, favorable will be lower values of observed fission barrier heights, what appears quite probable for neutron-deficient nuclei in the region around the shell closures Z=82 and N=126. In such case, using the ACTAR TPC, it will be possible to determine the mass distribution of the fission fragments and thus asymmetry of the dominant fission mode. The experiment was accepted as a part of the physics program of the HIE-ISOLDE and will be performed during the year 2016. While the proposed experiment considers measurement of proton-rich nuclei, there is also principal possibility to study low-energy fission of the neutron-rich nuclei. Good candidates for this type of study at the HIE-ISOLDE are the neutron-rich radioactive beams such as ^{228}Rn, of high interest for nuclear astrophysics (study of r-process).

Production of exotic nuclei in peripheral nucleus-nucleus collisions below 10 AMeV

The fragmentation reactions offer a successful approach to produce exotic nuclei at beam energies above 100 AMeV, nevertheless they are restricted by the fact that neutron excess is achieved by stripping the maximum possible number of protons (and a minimum possible number of neutrons). To reach an even higher neutron excess, it is necessary to capture additional neutrons from the target. Such an effect is observed in reactions of nucleon exchange [8] which dominate at beam energies around the Fermi-energy (15–50 AMeV) [9, 10, 11, 12, 13].

In the Fermi-energy domain, peripheral nucleus-nucleus collisions are described theoretically using the model of deep-inelastic transfer, in combination with an appropriate model of de-excitation. Deep-inelastic transfer (DIT) occurs when the interaction of the projectile and the target leads to formation of a di-nuclear configuration which exists long enough to allow intense exchange of nucleons through a "window" formed by the superposition of the nuclear mean-fields in the neck region. Transfer of nucleons leads to gradual dissipation of the kinetic energy of relative motion into internal degrees of freedom such as intrinsic (thermal) excitation and/or angular momentum. After re-separation, the hot projectile-like and target-like primary fragments share approximately equal excitation energy and undergo de-excitation via a cascade of particle emissions or via simultaneous multifragmentation.

A very good description of experimental data from peripheral collisions in the Fermi-energy domain was obtained [9] using the Monte Carlo deep-inelastic transfer (DIT) model of Tassan-Got [14, 15] for peripheral collisions, combined with an appropriate choice of model description for central collisions. In the central collisions at Fermi energies, pre-equilibrium emission (PE) and incomplete fusion (ICF) contribute to production of the projectile-like fragments. The combined model framework is referred to as the PE+DIT/ICF+SMM model [10]. Consistent good results can be obtained using the de-excitation code SMM [16], implementing the statistical model of multifragmentation (SMM) supplemented with particle evaporation and/or fission models for the secondary emission stage.

In this context it is also of interest to investigate reactions at energies around and below 10 AMeV and to establish to what extent the production rates can be described using the model of nucleon exchange. Knowledge of the reaction mechanism at these low energies will allow us to select the optimum projectile and target combinations, the appropriate target thickness, as well as the optimum experimental setup for efficient production and collection of very neutron-rich exotic nuclei. The use of the thicker target, decelerating the beam particle to energies close to the Coulomb barrier, will, on one hand, further enhance the estimated intensities of secondary beams, as provided e.g. in refs. [11, 17], on the other hand it can simplify the set-up of the gas-cell necessary to stop the reaction products.

The available experimental data from damped peripheral nucleus-nucleus collisions at beam energies below 10 AMeV, specifically in reactions of ^{58,64}Ni beams with Pb and U targets at beam energies around 6 AMeV [18, 19, 20] and in reactions of ^{22}Ne beam with Zr, Th targets [21], show that deep-inelastic transfer is the dominant reaction mechanism leading to the production of projectile-like nuclei [22]. As it was also demonstrated in the work [22], specific to this energy domain is a possible evolution of the extended nuclear profile in the window (neck) region, primarily in reactions with very heavy target nuclei. The effect seems to weaken with increasing beam energy, at 8 AMeV necessary extension of nuclear profile constitutes only 75 % of the same at 6 AMeV and at 15 AMeV the effect disappears at all. Presence of this effect was further verified using the recently published data from reaction of ^{136}Xe beam with ^{198}Pt target at 8 AMeV [23]. Again, using the same extension of nuclear profile as in [22] for Ne + Th reaction at 8 AMeV, the experimental yields were reproduced rather well, as can be seen in Fig. 2 (due to presence of experimental yields rather than cross sections a single normalization factor was employed). Thus the predictive power of the model simulations appears verified and it can be used for predictions of achievable rates of very neutron-rich nuclei at the facilities with post-accelerated beams such as HIE-ISOLDE.

As a first example, possibilities for production of the doubly magic nucleus ^{78}Ni can be investigated. Figure 3 shows results for the reaction of unstable nucleus ^{74}Zn with uranium target at 8 AMeV (solid line), using the same extended profile as above. One can see that the production cross section for ^{78}Ni exceeds

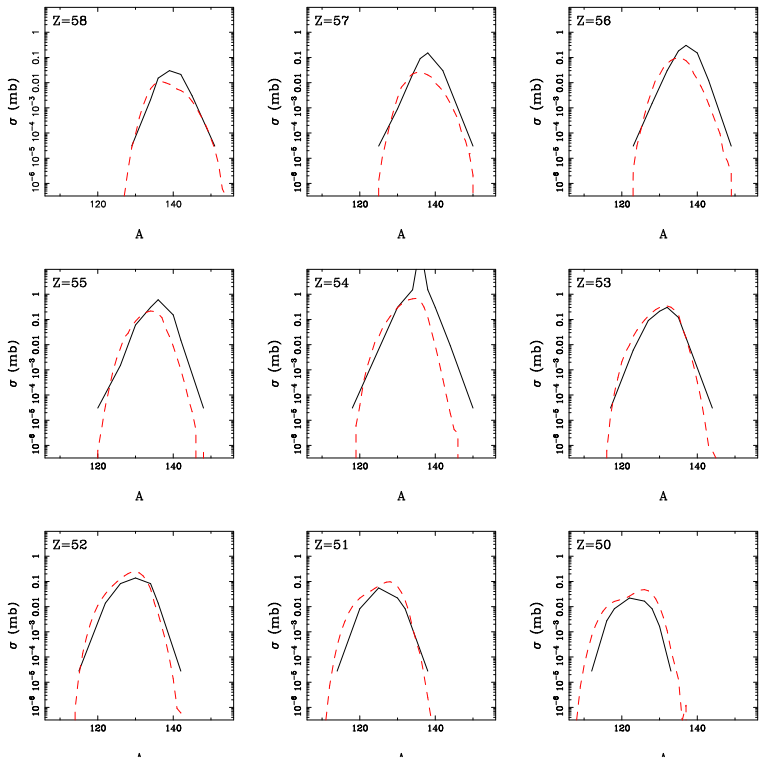

Fig. 2: Simulations performed using model of deep-inelastic transfer, with modifications described in [22] (dashed line) and compared to recent data in reaction of ^{136}Xe+^{198}Pt at 8 AMeV [23] (solid line).

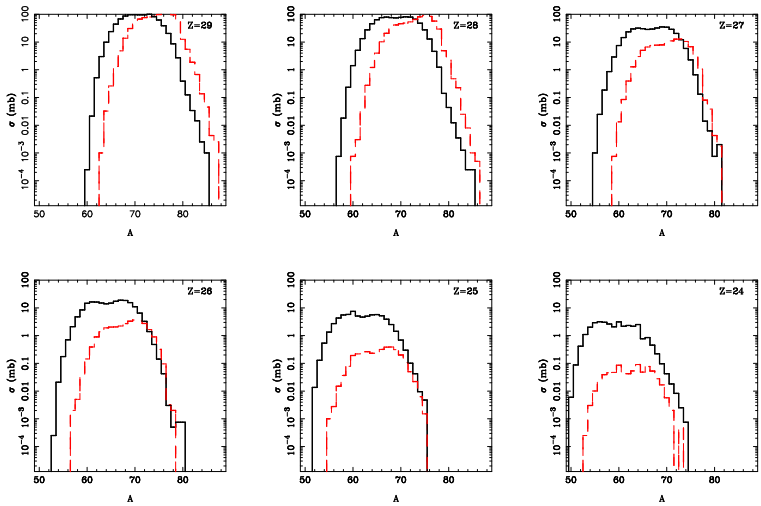

Fig. 3: Simulations performed using model of deep-inelastic transfer, with modifications described in [22] for reactions ^{74,78}Zn+^{238}U at 8 AMeV (solid and dashed line, respectively).

1 mb, what assuming the presently achievable rate of low-energy RIB from primary spallation target of the order of 10^8/s, efficiency of post-acceleration process at the level of 5 % and secondary target thickness of up to 10 mg/cm^2 leads to in-target production of one ^{78}Ni nucleus in about five seconds. This rate can be further improved by upgrade to newly built proton linac and by further optimization of the yield from the spallation target. From the experimental point of view, a sensitive method allowing to collect all the products over wide angular range will be necessary, what favors the use of a gas-cell, where total efficiency of the order of 10 % or more should be achievable. For the more neutron-rich RIB ^{78}Zn (dashed line) the drop of the yields from the spallation target by about factor of 20 is practically compensated by increase of production cross section of ^{78}Ni in secondary reaction and thus similar resulting yields of ^{78}Ni can be expected.

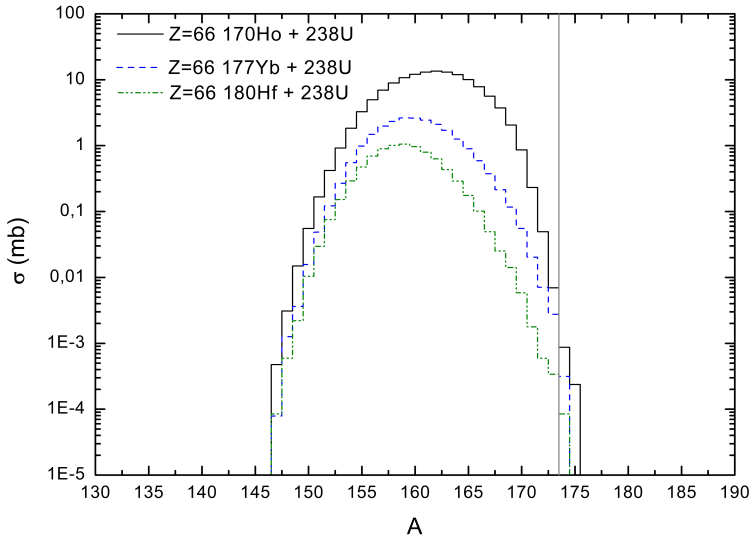

Fig. 4: Lines show production cross sections of Dy isotopes from simulations performed using model of deep-inelastic transfer, with modifications described in [22] for reactions ^{170}Ho,^{177}Yb,^{180}Hf+^{238}U at 8 AMeV [23] (solid, dashed and dotted line, respectively). Vertical line marks heaviest known isotope.

Besides the region of ^{78}Ni, it is also interesting to know what can be achieved for heavier neutron-rich nuclei above heavier than fission fragments produced in fission of uranium. Figure 4 shows situation for production of isotopes of Dy in reactions of radioactive beams of ^{170}Ho and ^{177}Yb (with yields of low-energy beams of 10^8/s) with uranium at 8 AMeV (solid and dashed lines, respectively). The vertical line shows the heaviest known isotope. It appears that many neutron-rich isotopes can be produced with reasonable rates and even the presently unknown isotopes appear reachable. For comparison also stable beam ^{180}Hf is considered, where in principle higher primary beam rates can be considered, however it might require rotating target and also the use of stable beam would result in much higher background from scattered beam in the gas-cell, from which the products of interest need to be separated. For even heavier nuclei, the secondary beam of ^{226}Fr appears as good candidate for production of wide range of neutron-rich isotopes down to Z=80.

Based on the above examples, it appears that the use of post-accelerated neutron-rich beams at HIE-ISOLDE for production of even more neutron-rich nuclei needs to be considered as an option for further upgrade.

High-power laser as a tool for nuclear reaction studies

Basic reason for the implementation of high-power laser in nuclear physics is the eventual possibility to generate extremely high gradients of electric field, which can be used for acceleration of nuclei. As of now, electrons and nuclear particles with energy reaching several hundreds of MeV can be generated using the table-top laser with ultrashort pulses focused to energy densities 10^{20} W/cm^2. Such kinetic energies are sufficient to initiate nuclear reactions and processes like photo-fission initiated by the laser were first observed at Rutherford Appleton Laboratory and Lawrence Livermore National Laboratory [24, 25], and more recently even using the table-top laser system [26]. This field of nuclear physics thus can be considered as established.

At the present, the most powerful laser is the BELLA Petawatt laser at Lawrence Berkeley National Laboratory, with the peak power of 1 PW (10^{22} W/cm^2) and repetition rate of 1 Hz. At present time a major European research center ELI-NP is being constructed in Bucharest, as a nuclear physics branch of the ESFRI project ELI, focusing on the use of high-power lasers in material and nuclear physics. A laser system with peak power of 2 times 10 PW, worth 60 MEUR, will be installed in the nuclear physics branch. Among the proposed experiments there is an experiment proposed by the Habs et al. [27], aiming to observe fusion of two unstable light fission fragments. Both fission fragments will be produced by intense laser pulses, one impinging on thorium foil, thus producing projectile-like fission fragments, and the other one impinging on CD_2 foil, thus producing protons and deuterons, which will initiate fission of thorium in the target and thus production of target-like fission fragment. Scheme of this experiment is shown in Figure 5a.

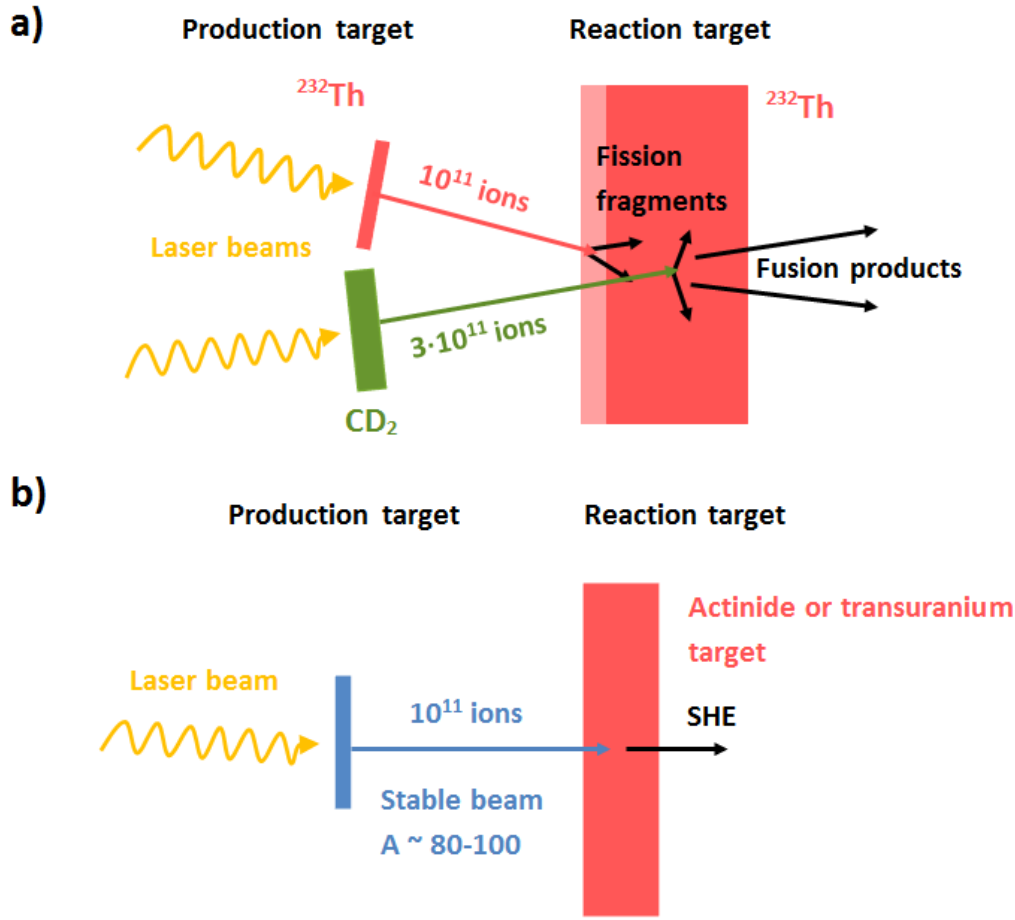

Fig. 5: Scheme of the experiment (a) proposed by Habs et al. [27] and (b) considered here for SHE production.

The proposal plans to use the so-called hole-boring variant of the Radiation Pressure Acceleration mechanism, allowing to accelerate the projectile-like light fission fragment to 7 AMeV, while the protons and deuteron are accelerated to the same energy per nucleon by another laser in order to initiate fission in Th target. Around 10^{11} of Th projectile-like and 3 times more of light ions will be generated per laser burst. At an estimated purely geometric fusion cross section and for normal stopping in the target material, the proposal arrives to a rate of 1.5 fusion products per laser bunch, which is experimentally observable.

The proposal further considers an effect of reduced stopping power for dense ion bunches in solid target and in this estimates production of more than 10^{10} of projectile-like and target-like fission fragments per laser burst. At an estimated purely geometric fusion cross section the expected rate of fusion products rises to 4×10^4 per laser burst. Due to uncertainty concerning the possible reduction of stopping the expected value is lowered to 10^3 per laser burst. The fusion products will be separated from the background using recoil separator and brought into its focal plane in order to identify them and study their properties. As a result of such experiment, properties of neutron-rich exotic nuclei in the vicinity of neutron shell N=126 can be explored, gaining valuable information for nuclear theory and nuclear astrophysics.

Due to emerging limitations for production of further super-heavy elements using the contemporary accelerator technology such as cyclotrons and linacs, it is interesting to understand whether high-power laser can provide an alternative. Already in the above mentioned experiment, in principle also reactions of e.g. fission fragments with Th target nuclei can be imagined, however its observation will be disfavored by many orders of magnitude due to drop in the fusion cross sections. Also the possibility to produce heavy nuclei with Z=100 by fusion of two heavy fission fragments in a similar way as described above will be influenced by dramatic drop in cross sections.

More conventional option would be to fuse the lighter stable beam with heavier Th-like (actinide or transuranium) target nucleus. In the scenario with the stable beam-like nuclei and normal stopping (see Fig. 5b) the thorium production foil will be replaced with lighter material and irradiated by the high-power laser. Similar number of accelerated nuclei should be obtained as in the case of thorium (thus gaining a factor of about $\times 10^3$ when compared to beam-like light fission fragments) and the difference in yield of evaporation residues will be determined by the production cross section of SHE and by the fact that target-like nucleus does not need to fission (so another factor 4×10^4 will be gained!). This means that e.g. for ER cross section of 1 pb the expected rate appears to be 4×10^{-5} per laser burst, with the expected repetition rate of 0.1 Hz (which is foreseen at ELI-NP) it will be one nucleus in about 100 hours! Such rate would not be too far from the existing best facilities. However, it is known that excitation functions of production of super-heavy nuclei are quite narrow what may limit the expected rate. Typical thickness of heavy targets used for production of SHE is 0.5 mg/cm^2, corresponding to about 2000 layers of material. Main reason for such thin targets is the low velocity of evaporation residues and thus a relatively small range in the material. Use of thicker targets typically does not increase the observed rate of SHE and saturation is observed, thus demonstrating that only a limited thickness of about 0.5 mg/cm^2 contributes. As a result, an additional factor of 10^{-2} might be expected, thus reducing the expected rate in the case of normal stopping to 4×10^{-7} per laser burst or one nucleus in 10000 hours (more than one year) at production cross sections of 1 pb. As mentioned above, for the production of SHE by the beam of light fission fragments (at normal stopping) the rate will be 10^3 times lower.

In the case of reduced stopping the total Th target thickness is expected to grow by a factor of 100, and assuming that the "active" part of the target will grow also by factor of 100 (to 50 mg/cm^2) for stable beam particle one arrives to the above mentioned rate 4×10^{-5}, or one nucleus per 100 hours at production cross section of 1 pb, which is quite encouraging. For reduced stopping, the beam rate of the light fission fragment rate will be equal to the initial Th beam (and thus only by a factor of 3 lower than for stable beam) and one can expect one nucleus per 300 hours. Furthermore, one can expect an increase of fusion cross section for neutron-rich fission fragments which can make this option preferential to the use of stable beam. Of course these considerations depend on existence of the reduced stopping, so one can adopt more modest estimate by taking geometric mean of the options with and without reduced stopping. In that case the rates would be one nucleus per 1000 hours for stable beam particle and 55000 hours (more than 6 years) for light fission fragment.

Thus one can conclude that the production of SHE using high-power laser is not excluded, however it strongly depends on the expected reduction of stopping in the dense ion bunches, which was not proved yet, and for practical application also increase of laser power by several orders of magnitude would be necessary, in order to compensate also separation and detection efficiency. Still, the dynamical evolution of still more powerful lasers leaves much room for optimism.

Besides other possible applications, it appears that high-power laser technique with ultra-dense beams might open pathway to ternary reactions of unstable nuclei e.g. ternary fusion of three light fission fragments. In the case of the above experiment, any of the 10^3 fusion products might fuse again and using similar considerations it appears that about 10^{-4} of such ternary fusions can occurs per one laser bunch, about once per day at the ELI-NP setup. While it is still hardly observable, due to additional reduction of rate due to fission, laser facilities appear to provide environment to facilitate studies of ternary reaction in principle, due to high density of accelerated nuclei. This concept can be in principle tested e.g. using the accelerated Al nuclei hitting the Al target. If the high-density bunch of Al hits the target, fusion will occur and the fusion products will be able to fuse again. Assuming that the number of accelerated ions per laser bunch will be again of the order of 10^{11} and taking into account that each atom of the target will be again Al, the probability of the ternary fusion will rise to the order of 10^3 per laser burst. This number was obtained assuming normal stopping, thickness of Al-target of 50 μm (as in the case of Th), and considering first two thirds of the Al-target as producing the fusion products which fuse again with Al-nucleus in the remaining third of the target. That should be obviously possible to observe. Of course the initial energy of the Al beam should be set so that the fusion products will be still fast enough to undergo fusion so some fine tuning of the above assumptions will be needed. Such experiment appears quite feasible and the ternary fusion may open pathway e.g. for simulation of astrophysical processes on Earth.

CONCLUSIONS

Future nuclear physics facilities such as radioactive ion beam facilities and high-power laser facilities offer many opportunities for investigations of nuclear reactions. Post-accelerated radioactive ion beams offer possibilities for study of the role of isospin asymmetry in the reaction mechanisms at various beam energies. Fission barrier heights of neutron-deficient nuclei can be directly determined at low energies. Post-accelerated radioactive ion beams, specifically at the future facilities such as HIE-ISOLDE, SPIRAL-2 or RAON-RISP can be also considered as a viable candidate for production of very neutron-rich nuclei via mechanism of multi-nucleon transfer. High-power laser facilities such as ELI-NP, using the beams of unprecedented properties, offer possibilities for nuclear reaction studies such as ternary reactions and high power lasers with even higher intensities, which will be available in foreseeable future, can be even considered for production of super-heavy elements.

ACKNOWLEDGMENT:

This work is supported by the Slovak Scientific Grant Agency under contracts 2/0121/14, by the Slovak Research and Development Agency under contract APVV-0177-11 (M.V.), by the NSFC of China under contract Nos. 11035009, 10979074, and by ELKE account No 70/4/11395 of the National and Kapodistrian University of Athens (G.S.).

REFERENCES

[1] I.V. Panov et al., "Calculations of fission rates for r-process nucleosynthesis", Nucl. Phys. A **747**, 633 (2005).
[2] A.N. Andreyev et al., Phys. Rev. Lett. **105**, 252502 (2010).
[3] A.J. Sierk, Phys. Rev. C **33**, 2039 (1986).
[4] P. Möller et al., Phys. Rev. C **79**, 064304 (2009).
[5] M. Veselsky, A.N. Andreyev, S. Antalic, M. Huyse, P. Möller, K. Nishio, A.J. Sierk, P. Van Duppen, M. Venhart, "Fission barrier heights of neutron-deficient mercury nuclei", Phys. Rev. C **86**, 024308 (2012).
[6] A.J. Koning, S. Hilaire and M.C. Duijvestijn, "TALYS: Comprehensive nuclear reaction modeling", AIP Conf. Proc. **769**, 1154 (2005).
[7] R. Raabe and ACTAR coll., "ACTAR: the New Generation of Active Targets", AIP Conf. Proc. **1165**, 339 (2009).
[8] V.V. Volkov, Phys. Rep. **44**, 93 (1978).
[9] M. Veselsky et al., Phys. Rev. C **62**, 064613 (2000).
[10] M. Veselsky, Nucl. Phys. A **705**, 193 (2002).
[11] G.A. Souliotis et al., Phys. Lett. B **543**, 163 (2002).
[12] G.A. Souliotis et al., Phys. Rev. Lett. **91**, 022701 (2003).
[13] G.A. Souliotis et al., Phys. Rev. C **84**, 064607 (2011).
[14] L. Tassan-Got, PhD Thesis, 1988, Orsay, France, IPNO-T-89-02.
[15] L. Tassan-Got and C. Stéphan, Nucl. Phys. A **524**, 121 (1991).
[16] J.P. Bondorf et al., Phys. Rep. **257**, 133 (1995).
[17] G.A. Souliotis et al., Nucl. Instrum. Methods B **204**, 166 (2003).
[18] L. Corradi et al., Nucl. Phys. A **734**, 237 (2004).
[19] W. Królas et al., Nucl. Phys. A **724**, 289 (2003).
[20] L. Corradi et al., Nucl. Phys. A **701**, 109c (2002).
[21] A.G. Artukh et al., Nucl. Phys. A **283**, 350 (1977).
[22] M. Veselsky and G.A. Souliotis, Nucl. Phys. A **872**, 1 (2011).
[23] Y.X. Watanabe et al, Nucl. Instrum. Methods B **317**, 752 (2013).
[24] K.W.D. Ledingham et al., Phys. Rev. Lett. **84**, 899 (2000).
[25] T.E. Cowan et al., Phys. Rev. Lett. **84**, 903 (2000).
[26] H. Schwoerer et al., Europhys. Lett. **61**, 47 (2003).
[27] D. Habs et al., Appl. Phys. B **103**, 471 (2011).

On the Density and Momentum Dependent Symmetry Energy in a Boltzmann-Langevin Approach

Pei-Wei Wen[1,2], Chen-Chen Guo[1,2,3], Wen-Jie Xie[1,2,4] and Feng-Shou Zhang[1,2,5*]

[1]The Key Laboratory of Beam Technology and Material Modification of Ministry of Education, College of Nuclear Science and Technology, Beijing Normal University, Beijing 100875, China
[2]Beijing Radiation Center, Beijing 100875, China
[3]Shanghai Institute of Applied Physics, Chinese Academy of Sciences, Shanghai 201800, China
[4]Department of physics, Yuncheng University, Yuncheng 044000, China
[5]Center of Theoretical Nuclear Physics, National Laboratory of Heavy Ion Accelerator of Lanzhou, Lanzhou 730000, China

Abstract

Based on the improved isospin-dependent Boltzmann-Langevin model, incorporating the dynamical fluctuations, we study the density and momentum dependence of symmetry energy. It is found that a supersoft symmetry energy can reproduce the FOPI experimental data quite well. The double neutron and proton ratio data from central ^{124}Sn + ^{124}Sn and ^{112}Sn + ^{112}Sn collisions at 50 MeV/nucleon is compared to model simulations, and the result shows that calculations with $m_n^\star < m_p^\star$ agree with the double ratio data better.

INTRODUCTION

Study of the density dependence of the nuclear symmetry energy is the main challenge of the intermediate-energy heavy-ion physics nowadays [1]. Knowledge of nuclear symmetry energy is of great importance for both nuclear physics and astrophysics. As an important counterbalance of Coulomb force in nuclei, symmetry energy is crucial for drip line nuclei to keep stability against β decay [2], the stability of superheavy nuclei against α decay [3], and the neutron skin thickness of nuclei [4]. In astrophysics, the composition and thickness, stability of phases, cooling processes and crustal vibrations of neutron stars are all strongly influenced by symmetry energy and its density dependence [5, 6, 7].

However, there is still no consensus on the trend of symmetry energy $E_{sym}(\rho)$ with respect to density. Near the nuclear saturation density, symmetry energy and its slope have been relatively well constrained by various nuclear structure observations and nuclear reactions within experimental uncertainties [4, 8]. At sub-saturation density, compared with properties of nuclei and nuclear response to electroweak and hadronic probes, the trend is almost confirmed by different theoretical models, but quantitatively to be determined [9, 10, 11].

The major uncertainties of density-dependent symmetry energy exist at supra-saturation density region, even the trend of which with increasing density is not constrained. For example, a very soft symmetry energy was obtained with isospin and momentum dependent Boltzmann-Uehling-Uhlenbeck (IBUU04) transport model through calculating the excitation function of pion ratio [12]. Within the framework of improved isospin dependent quantum molecular dynamics (ImIQMD) model, systematical investigations provided circumstantial evidence suggesting a hard symmetry energy from pion emission in heavy-ion collisions [13]. A moderately soft to linear symmetry energy was obtained by newly updated version of ultra-relativistic quantum molecular dynamics (UrQMD) model calculations [14].

The emission of pion has been proposed for many years to investigate the nuclear equation of state (EoS) [15, 16, 17, 18] and the $E_{sym}(\rho)$ [12, 13, 19] under extreme conditions. Using the relativistic Vlasov-Uehling-Uhlenbeck (RVUU) equation, the in-medium threshold effect could enhance both the total pion yields and the π^-/π^+ ratio [20]. However, no significant sensitivity relative to symmetry energy was found by calculations with pBUU model by incorporating pion optical potential in a recent research [21]. All these studies complicate the survey of density dependence of symmetry energy.

According to the general Hugenholtz-Van Hove theorem, nuclear symmetry energy and its slope at an arbitrary density are determined by the nucleon isovector (symmetry) potential and its momentum dependence [22, 23]. After examining the effect of Symmetry potentials corresponding to the same symmetry energy but with different kind of momentum dependence, significantly different predictions were obtained on several symmetry energy sensitive experimental observables [24]. Different kind of momentum dependence

*E-mail: fszhang@bnu.edu.cn

potential also leads to completely different nuclear collective flow [25, 26], various N/Z ratio [27], isospin equilibrium [28, 24], meson production [29].

Besides, momentum dependent potential also determines uniquely the neutron-proton effective mass splitting (NPEMS) in neutron-rich nuclear matter. Constraints on the NPEMS are important for constraining the symmetry energy. However, whether neutron effective mass is larger than proton effective mass or otherwise is still controversial. Publications show contradictory results. Firstly, from the view of microscopic theory, investigation on the single particle properties and EoS of isospin asymmetric nuclear matter, employing the Brueckner theory including a microscopic three body force, resulted in a smaller proton effective mass than that of neutron [30]. After coupling to a δ-isovector-scalar meson in a phenomenological hadronic field theory, another group arrived at a conclusion that proton effective mass is larger than that of neutron [31]. Within a relativistic Hartree-Fock approach with density-dependent σ, ω, ρ and π meson-nucleon couplings for finite nuclei and nuclear matter, the effective mass was predicted to be varying with respect to energy, which means that proton effective mass is smaller than that of neutron in lower energy region and the situation is opposite in higher energy region [32]. Besides, the results obtained by transport theory comparing with experimental data are also disputed. The calculation with improved quantum molecular dynamics (ImQMD) model including standard Skyrme interactions favored a smaller effective mass for neutrons than for protons [27]. Constraining the NPEMS using empirical constraints on the density dependence of nuclear symmetry energy around normal density, inferred that proton effective mass is smaller than that of neutron [23], which is also consistent with a global nucleon optical potentials analysis [33]. Therefore, it is imperative to pin down NPEMS with heavy ion collision experiments and theories.

The paper is arranged as follows: In the next section, we will discuss the theoretical framework of improved isospin-dependent Boltzmann-Langevin Equation. The density dependence and momentum dependence of symmetry energy are illustrated afterwards, respectively. After that, conclusions are drawn in the last section.

Boltzmann-Langevin Equation

As a kind of ensemble-averaged theory, the Boltzmann-Uehling-Uhlenbeck (BUU) model cannot describe the fluctuation phenomena in the nuclear collisions, which are responsible for the multifragmentation processes, correlations in light-particle emission and fluctuations of one-body observables [34]. To describe the fluctuation phenomena in the nuclear collisions, according to the fluctuation-dissipation theorem, a Boltzmann-Langevin (BL) model which incorporates fluctuations, which are initially produced during the early, most dissipative stage of the reaction, into the BUU equation was proposed. The equation is expressed as [35, 36, 37]

$$\Big(\frac{\partial}{\partial t}+\frac{\mathbf{P}}{m}\cdot\nabla_r-\nabla_r U(\hat{f})\cdot\nabla_p\Big)\hat{f}(\mathbf{r},\mathbf{p},t)=K(\hat{f})+\delta K(\mathbf{r},\mathbf{p},t). \tag{1}$$

The left-hand side describes the Vlasov propagation determined by the fluctuating nuclear mean-field $U(\hat{f})$. $K(\hat{f})$ is the collision term of the usual BUU form but expressed in terms of the fluctuating density. The fluctuating collision term $\delta K(\mathbf{r},\mathbf{p},t)$ arises from higher-order correlations, which can be explained as a stochastic force acting on $\hat{f}$ and characterized by a correlation function [37, 38],

$$\langle\delta K(\mathbf{r}_1,\mathbf{p}_1,t_1)\delta K(\mathbf{r}_2,\mathbf{p}_2,t_2)\rangle=C(\mathbf{p}_1,\mathbf{p}_2)\delta(\mathbf{r}_1-\mathbf{r}_2)\delta(t_1-t_2), \tag{2}$$

where the angle brackets stand for a local average, performed over fluctuating densities generated during a short time interval δt. The reduced correlation function $C(\mathbf{p}_1,\mathbf{p}_2)$ can be expressed in the weak-coupling limit and determined by the one-body properties of the locally averaged distribution as indicated in Ref. [37]. The method of numerical simulations of Eq.(2) employed here is the projection method [34, 36, 37]. The fluctuations are projected on the momentum space, which provides the initial seed for density fluctuations in coordinate space. A transient behavior of the momentum distributions is found by the numerical simulations of the BL model, which is consistent with the expectations from the fluctuation-dissipation theorem. It is worth noting that another method implementing fluctuations in the mean-field dynamics has been proposed in the framework of the SMF, in which the fluctuations are projected on the coordinate space [39]. Based on the SMF, the properties of fragmentation have been discussed by the Catania group [40].

The BL model has been successfully applied to describe the nuclear collisions at low energies [36]. Moreover, this model is successful in describing the multifragmentation [37] and, the extended BL model by incorporating the isospin effect which is called the isospin-dependent Boltzmann-Langevin model can reproduce the fragmentation cross sections [41]. Furthermore, the calculations of K^+ production cross sections at subthreshold energies in the $^{12}\mathrm{C}+{}^{12}\mathrm{C}$ collisions indicated that the yields obtained in the BL model are

much larger than those obtained in the BUU model [42]. The calculations of Ref. [15] indicated that the momentum dependent nuclear interactions (MDI) have a large effect on the pion production. Therefore, it is very interesting and imperative to improve the isospin-dependent Boltzmann-Langevin model [41] and to investigate meson production in the heavy ion collisions, especially near the meson threshold energy. The inelastic channels which mainly produce the pion meson and the MDI are incorporated in the isospin-dependent Boltzmann-Langevin model [41] (the improved isospin-dependent Boltzmann-Langevin model, named the ImIBL model). We investigate the pion emission in the framework of the ImIBL model.

The isospin and momentum dependent single nucleon potential used in the ImIBL model reads

$$U_\tau(\rho,\delta,\mathbf{p}) = \alpha\frac{\rho}{\rho_0} + \beta\Big(\frac{\rho}{\rho_0}\Big)^\gamma + E^{loc}_{sym}(\rho)\delta^2 + \frac{\partial E^{loc}_{sym}(\rho)}{\partial\rho}\rho\delta^2 + E^{loc}_{sym}(\rho)\rho\frac{\partial\delta^2}{\partial\rho_\tau} + U_{MDI}, \tag{3}$$

where $\delta = (\rho_n - \rho_p)/\rho$ is the isospin asymmetry, and ρ, ρ_n and ρ_p are the total, neutron and proton densities, respectively. The values of bulk parameters α, β, and γ taken here are 390 MeV, 320 MeV and 1.14 for the soft EOS plus MDI as SM; and 130 MeV, 59 MeV and 2.09 for the hard EOS plus MDI as HM [43]. The compressibilities K are 200 and 380 MeV for the SM and HM, respectively.

Density Dependency of Symmetry Energy

The pion emission as a probe of the $E_{sym}(\rho)$ is motivated by the $\Delta(1232)$ resonance model [44] which predicts a primordial relation between π^-/π^+ ratio and N/Z, that is

$$\pi^-/\pi^+ = (5N^2 + NZ)/(5Z^2 + NZ) \approx (N/Z)^2 \tag{4}$$

where the N and Z are the neutron and proton numbers in the participant region of the reaction. The N/Z is determined by the $E_{sym}(\rho)$ through the dynamical isospin fractionation [19]. Therefore, one can use the π^-/π^+ ratio to measure the isospin asymmetry N/Z of the dense nuclear matter and then constrain the $E_{sym}(\rho)$.

The E^{loc}_{sym} in Eq.(3) is the local part of the symmetry energy, which mimics the predictions by microscopical or phenomenological many-body theories. To investigate the density dependence, we take two forms at here. The first one is as follows

$$E^{loc}_{sym}(\rho) = \frac{1}{2}C_{sym}\Big(\frac{\rho}{\rho_0}\Big)^{\gamma_s}, \tag{5}$$

where γ_s=0.5, 1.0, and 2.0 correspond to the soft, linear and hard symmetry energy, respectively. The second one reads

$$E^{loc}_{sym}(\rho) = a\Big(\frac{\rho}{\rho_0}\Big) + b\Big(\frac{\rho}{\rho_0}\Big)^2 + \Big(\frac{\rho}{\rho_0}\Big)^{5/3}. \tag{6}$$

The coefficient values of C_{sym}, a, b and c in above two equations are 29.4, 38.9, -18.4 and -3.8 MeV, respectively. Eq. (6) is directly deduced from Skyrme energy density functional and gives a supersoft symmetry energy. The parameters in Eq. (6) are related to the Skyrme parameters t_0, t_1, t_2, t_3 and x_0, x_1, x_2, x_3 [13].

The excitation functions of the π^-/π^+ ratio calculated with the ImIBL model and measured by the FOPI Collaboration for most central ^{197}Au + ^{197}Au collisions are shown in Fig. 1. The calculations show that the π^-/π^+ ratios decrease with increasing incident energies as reported in Refs. [12, 13, 45]. Moreover, from the left panel of Fig. 1, it is found that the ImIBL calculations with a supersoft symmetry energy describe rather well the FOPI data [45]. Most interestingly, a larger π^-/π^+ value is obtained at incident energy smaller than π threshold and the calculated results, shown in the right panel of Fig. 1, of the usual BUU model are slightly different to those with the ImIBL model. That the fluctuations and the symmetry energy act together would be responsible for this phenomenon. In the early stage of the collisions, there will have abundant neutron-neutron scatterings when the two neutron skins start overlapping [19] and at the same time, the fluctuations are also strong. Therefore, for the incident energies near the π threshold, the π^- is more easy to produce than the π^+ in the early stage of the collisions. For the higher incident energies, the π^-/π^+ values are only affected by the symmetry energy because the effects of the fluctuations are negligible.

We would like to point out that the threshold effects are not included in the present work. According to the Ref. [46, 47], the threshold effects increase the π^- yield through enhancing the production of the Δ resonances. The in-medium threshold values of producing $\pi^\pm$ and π^0 production are different because of the different effective Dirac masses of the four isospin states of the Δ resonance. In the framework of the relativistic Boltzmann-Uehling-Uhlenbeck (RBUU) model, the symmetry energy is related to the ρ- and

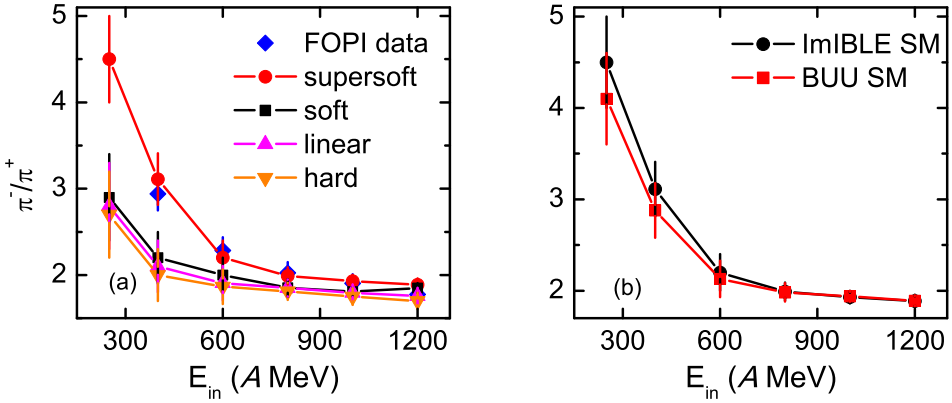

Fig. 1: (Color online.) Excitation functions of the π^-/π^+ ratio in central ^{197}Au + ^{197}Au collisions for different stiffness of the symmetry energy using the ImIBL model with the SM (left panel) and different transport theories (right panel). Calculations are compared with experimental FOPI data from Ref. [45]. Taken from Ref. [29]

δ-meson couplings [46]. Because of the inconsistent treatment of the mean-field potentials in the RBUU and ImIBL approaches, the predicted dependence of π^-/π^+ ratio on the symmetry energy is opposite. From the left panel of Fig. 1 we can see that the π^-/π^+ yield at lower incident energies is more sensitive to the symmetry energy and can provide more information of the symmetry energy, especially at beam energies smaller than the π threshold. Further experimental works are very necessary to constrain the symmetry energy and test our findings here.

Momentum Dependency of Symmetry Energy

The effective mass of a nucleon will deviate from its vacuum value when it propagates in the nuclear medium [48, 49]. In nonrelativistic transport model, the nucleon effective mass measures the momentum-dependent nucleon single-particle potential. It can be defined via the following expression [50]:

$$\frac{m_\tau^\star}{m_\tau} = \Big[1 + \frac{m_\tau}{|\mathbf{P}|}\frac{dU_\tau}{d|\mathbf{P}|}\Big]^{-1}_{\mathbf{P}=\mathbf{P}_F^\tau}, \tag{7}$$

where $\mathbf{P}$ is the momentum of a nucleon and τ denotes the neutron or proton. According to Eq. (7), the effective masses $m_n^\star$ for neutrons and $m_p^\star$ for protons and the effective mass splitting $m_n^\star - m_p^\star$ are determined by the momentum-dependent mean-field potential and Fermi momenta of neutrons and protons.

To probe the momentum dependent term further, we engaged a simple form of symmetry energy as Eq.(5) shows and a more sophisticated isospin- and momentum-dependent potential, which reads [51]

$$U_{\rm MDI} = \frac{C_{\tau,\tau}}{\rho_0}\int d\mathbf{p}' f_\tau(\mathbf{r},\mathbf{p})\ln^2[0.0005(\mathbf{p}-\mathbf{p}')+1] + \frac{C_{\tau,\tau'}}{\rho_0}\int d\mathbf{p}' f'_\tau(\mathbf{r},\mathbf{p})\ln^2[0.0005(\mathbf{p}-\mathbf{p}')+1], \tag{8}$$

where the parameters $C_{\tau,\tau} = 1.57(1-x)$ and $C_{\tau,\tau'} = 1.57(1+x)$. The two sets of coefficient values of C_{sym} and x are 52.5 MeV, -0.65 and 23.52 MeV, 0.65, corresponding to the mass splittings $m_n^\star > m_p^\star$ and $m_n^\star < m_p^\star$, respectively, which gives opposite mass splitting but quite similar density dependencies of the symmetry energy. From Eq. (8) one can get the symmetry energy contribution from the nonlocal potential part.

The theoretical results will be more significative and useful when they can be compared with the experimental data. We show in Fig.2 the kinetic energy dependence of double ratio, which is defined via the following expression [9]:

$$DR(N/Z) = \frac{R^A_{N/Z}}{R^B_{N/Z}} = \frac{dM_n^A/dE_k}{dM_p^A/dE_k}\cdot\frac{dM_p^B/dE_k}{dM_n^B/dE_k} \tag{9}$$

where A and B refer to as the reaction systems of ^{124}Sn + ^{124}Sn and ^{112}Sn + ^{112}Sn, respectively. The incident energy for the systems A and B is 50 MeV/nucleon and the impact parameter is b=2 fm. It has been found that, for the DR(N/Z), impact parameter dependence is rather weak [9, 54]. Therefore, the impact parameter used in the present work is reasonable. We also perform the calculations by taking the

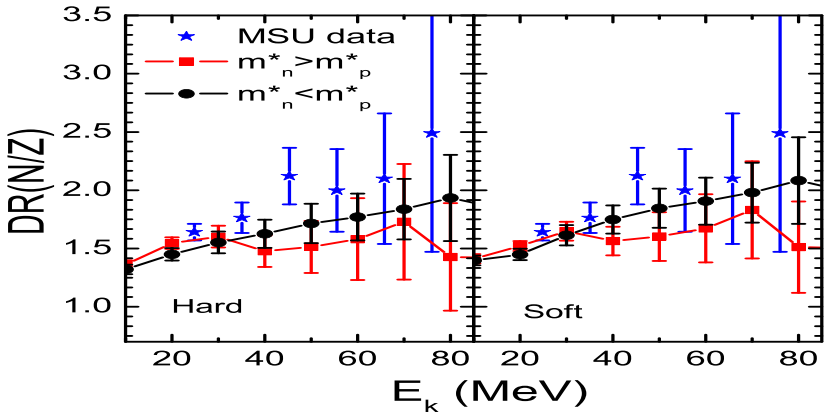

Fig. 2: (Color online) Comparison of the double neutron-proton ratio at 50 MeV/nucleon and impact parameter b=2 fm with the NSCL-MSU data [52]. The calculations are done by using hard and soft symmetry energies for two opposite mass splitting choices. Taken from Ref. [53]

hard and soft symmetry energies for two opposite mass splitting choices. It seems to require more repulsive force for neutrons in the higher kinetic energy region, as seen by comparison with the experimental data of NSCL-MSU (National Superconducting Cyclotron Laboratory at Michigan State University) [52]. Thus the calculations favor the choice of the soft symmetry energy plus the $m_n^\star < m_p^\star$.

It is worth noting that the cluster production and secondary decay may highly influence the values of DR(N/Z), especially in lower energy region [55]. By coupling the transport model with the statistical decay model, it is found that the sequential decay effects will be largely suppressed for the double ratios DR(n/p) [56]. It is difficult for the present model to describe accurately the cluster production in heavy ion collisions. Further improvements to the model are needed.

CONCLUSIONS

In summary, we have studied the density and momentum dependence of symmetry energy within the framework of improved isospin-dependent Boltzmann-Langevin model. The π production in central heavy ion collisions at incident energies from 250 to 1200 AMeV is employed to probe the density dependent part of symmetry energy. It is found that the π multiplicity is very sensitive to the fluctuations at energies smaller than the π threshold. The excitation functions of π^-/π^+ ratios for central ^{197}Au + ^{197}Au collisions are compared with calculations employing different stiffness of symmetry energy and different transport theories. Our results support the view of the BUU model that the calculations with the supersoft symmetry energy approach the FOPI data.

In addition, the $m_n^\star - m_p^\star$ in central reactions using Sn isotopes at 50 MeV/nucleon is investigated to pin down the momentum dependent part of symmetry energy. It is found that the isospin content of fast nucleon emission as well as the free nucleons in the late stages of reaction can be a good probe to constrain the $m_n^\star - m_p^\star$. The nucleons with smaller effective mass will suffer more repulsive force at higher momenta and larger rapidities. Our calculations show that the results with a soft density dependence of symmetry energy plus the $m_n^\star < m_p^\star$ approach the experimental data.

ACKNOWLEDGMENT:
This work was supported by the National Natural Science Foundation of China under Grants No. 11025524 and No. 11161130520 and the National Basic Research Program of China under Grant No. 2010CB832903, the European Commission's 7th Framework Programme (Fp7-PEOPLE-2010-IRSES) under Grant Agreement Project No. 269131, and the National Natural Science Foundation of China Projects (Nos 11175218 and U1332207).

REFERENCES

[1] M. Di Toro, V. Baran, M. Colonna, G. Ferini et al., Prog. Part. Nucl. Phys. **62**, 389 (2009).
[2] P. Danielewicz and J. Lee, Nucl. Phys. A **818**, 36 (2009).
[3] J. Dong, W. Zuo and W. Scheid, Phys. Rev. Lett. **107**, 012501 (2011).
[4] M.B. Tsang, J.R. Stone, F. Camera, P. Danielewicz et al., Phys. Rev. C **86**, 015803 (2012).

[5] J.M. Lattimer and M. Prakash, Science **304**, 536 (2004).
[6] B.G. Todd-Rutel and J. Piekarewicz, Phys. Rev. Lett. **95**, 122501 (2005).
[7] A.W. Steiner, Phys. Rev. C **77**, 035805 (2008).
[8] J.M. Lattimer and Y. Lim, Astrophys. J. **771**, 51 (2013).
[9] M.B. Tsang, Y. Zhang, P. Danielewicz, M. Famiano et al., Phys. Rev. Lett. **102**, 122701 (2009).
[10] S. Kumar, Y.G. Ma, G.Q. Zhang and C.L. Zhou, Phys. Rev. C **84**, 044620 (2011).
[11] Y. Wang, C. Guo, Q. Li and H. Zhang, Eur. Phys. J. A **51**, 37 (2015).
[12] Z. Xiao, B.-A. Li, L.-W. Chen, G.-C. Yong and M. Zhang, Phys. Rev. Lett. **102**, 062502 (2009).
[13] Z.-Q. Feng and G.-M. Jin, Phys. Lett. B **683**, 140 (2010).
[14] Y. Wang, C. Guo, Q. Li, H. Zhang et al., Phys. Rev. C **89**, 044603 (2014).
[15] J. Aichelin, A. Rosenhauer, G. Peilert, H. Stoecker and W. Greiner, Phys. Rev. Lett. **58**, 1926 (1987).
[16] Q. Li, Z. Li, S. Soff, M. Bleicher and H. Stöcker, J. Phys. G **32**, 151 (2006).
[17] H. Stöcker and W. Greiner, Phys. Rep. **137**, 277 (1986).
[18] G.F. Bertsch, H. Kruse and S. Das Gupta, Phys. Rev. C **29**, 673 (1984).
[19] B.-A. Li, G.-C. Yong and W. Zuo, Phys. Rev. C **71**, 014608 (2005).
[20] T. Song and C.M. Ko, Phys. Rev. C **91**, 014901 (2015).
[21] J. Hong and P. Danielewicz, Phys. Rev. C **90**, 024605 (2014).
[22] N.M. Hugenholtz and L. van Hove, Physica **24**, 363 (1958).
[23] B.-A. Li and X. Han, Phys. Lett. B **727**, 276 (2013).
[24] B.-A. Li, C.B. Das, S. Das Gupta and C. Gale, Phys. Rev. C **69**, 011603 (2004).
[25] V. Giordano, M. Colonna, M. Di Toro, V. Greco and J. Rizzo, Phys. Rev. C **81**, 044611 (2010).
[26] C. Guo, Y. Wang, Q. Li, P. Wen and F.-S. Zhang, Phys. Rev. C **91**, 054615 (2015).
[27] Y. Zhang, M.B. Tsang, Z. Li and H. Liu, Phys. Lett. B **732**, 186 (2014).
[28] S. Kubis and M. Kutschera, Phys. Lett. B **399**, 191 (1997).
[29] W.-J. Xie, J. Su, L. Zhu and F.-S. Zhang, Phys. Lett. B **718**, 1510 (2013).
[30] W. Zuo, I. Bombaci and U. Lombardo, Eur. Phys. J. A **50**, 12 (2014).
[31] B. Liu, V. Greco, V. Baran, M. Colonna and M. Di Toro, Phys. Rev. C **65**, 045201 (2002).
[32] W.-H. Long, N. Van Giai and J. Meng, Phys. Lett. B **640**, 150 (2006).
[33] C. Xu, B.-A. Li and L.-W. Chen, Phys. Rev. C **82**, 054607 (2010).
[34] Y. Abe, S. Ayik, P.-G. Reinhard and E. Suraud, Phys. Rep. **275**, 49 (1996).
[35] S. Ayik and C. Gregoire, Phys. Lett. B **212**, 269 (1988).
[36] E. Suraud, S. Ayik, M. Belkacem and F.-S. Zhang, Nucl. Phys. A **580**, 323 (1994).
[37] F.S. Zhang and E. Suraud, Phys. Lett. B **319**, 35 (1993).
[38] S. Ayik, E. Suraud, M. Belkacem and D. Boilley, Nucl. Phys. A **545**, 35 (1992).
[39] M. Colonna, M. Di Toro, A. Guarnera, S. Maccarone et al., Nucl. Phys. A **642**, 449 (1998).
[40] V. Baran, M. Colonna, V. Greco and M. Di Toro, Phys. Rep. **410**, 335 (2005).
[41] B.-A. Bian, F.-S. Zhang and H.-Y. Zhou, Nucl. Phys. A **807**, 71 (2008).
[42] M. Belkacem, E. Suraud and S. Ayik, Phys. Rev. C **47**, R16 (1993).
[43] J. Aichelin, Phys. Rep. **202**, 233 (1991).
[44] R. Stock, Phys. Rep. **135**, 259 (1986).
[45] W. Reisdorf and FOPI Collaboration, Nucl. Phys. A **781**, 459 (2007).
[46] G. Ferini, T. Gaitanos, M. Colonna, M. Di Toro and H.H. Wolter, Phys. Rev. Lett. **97**, 202301 (2006).
[47] T. Gaitanos, M. Di Toro, S. Typel, V. Baran et al., Nucl. Phys. A **732**, 24 (2004).
[48] J.P. Jeukenne, A. Lejeune and C. Mahaux, Phys. Rep. **25**, 83 (1976).
[49] G.F. Bertsch and S. Das Gupta, Phys. Rep. **160**, 189 (1988).
[50] E.N.E. van Dalen, C. Fuchs and A. Faessler, Phys. Rev. Lett. **95**, 022302 (2005).
[51] Z.-Q. Feng, Phys. Rev. C **85**, 014604 (2012).
[52] M.A. Famiano, T. Liu, W.G. Lynch, M. Mocko et al., Phys. Rev. Lett. **97**, 052701 (2006).
[53] W.-J. Xie, J. Su, L. Zhu and F.-S. Zhang, Phys. Rev. C **88**, 061601 (2013).
[54] Y. Zhang, D.D.S. Coupland, P. Danielewicz, Z. Li et al., Phys. Rev. C **85**, 024602 (2012).
[55] T.X. Liu, W.G. Lynch, R.H. Showalter, M.B. Tsang et al., Phys. Rev. C **86**, 024605 (2012).
[56] Y. Zhang, P. Danielewicz, M. Famiano, Z. Li et al., Phys. Lett. B **664**, 145 (2008).

3 ABSTRACTS

Collinear laser spectroscopy at the COLLAPS setup

Mark Bissell
The University of Manchester, United Kingdom

E-mail: mark.bissell@cern.ch

Abstract

Collinear laser spectroscopy provides one of the most versatile tools for examining a large number of observables of the atomic nucleus. With the COLLAPS setup at CERN-ISOLDE wide ranging issues have been addressed using a number of collinear laser spectroscopy techniques. Recent measurements will be presented along with a critical evaluation of what we have learned.

Uncertainties, modelling and super-heavies

David Boilley
GANIL Caen, France

E-mail: boilley@ganil.fr

Abstract

Describing the complete reaction leading to the synthesis of superheavy elements is still a challenge. One of the reason is the so-called fusion hindrance phenomenon that is well understood qualitatively but not quantitatively. There are large discrepancies in the predictions of various models. Some differences come from the parameters and some from the models. Is it possible to disentangle the two contributions to assess the models? We have started to evaluate the uncertainties related to the parameters entering the model to see if they can explain alone the large differences observed between various models. In particular, we have focused our work on the last phase of the reaction that is supposed to be the best known part, i.e. the fission evaporation part.

Density dependence of the symmetry energy from systematics

Lie-Wen Chen
Jiao Tong University Shanghai, China

E-mail: lwchen@sjtu.edu.cn

Abstract

We explore the systematics of the density dependence of nuclear matter symmetry energy in the ambit of microscopic calculations with various energy density functionals, and find that the symmetry energy from subsaturation density to supra-saturation density can be well determined by three characteristic parameters of the symmetry energy at saturation density ρ_0, i.e., the magnitude $E_{\rm sym}(\rho_0)$, the density slope L and the density curvature $K_{\rm sym}$. This finding opens a new window to constrain the supra-saturation density behavior of the symmetry energy from its (sub-saturation density behavior. In particular, we obtain $L = 46.7 \pm 12.8$ MeV and $K_{\rm sym} = -166.9 \pm 168.3$ MeV as well as $E_{\rm sym}(2\rho_0) \approx 40.2 \pm 12.8$ MeV and $L(2\rho_0) \approx 8.9 \pm 108.7$ MeV based on the present knowledge of $E_{\rm sym}(\rho_0) = 32.5 \pm 0.5$ MeV, $E_{\rm sym}(\rho_0) = 26.65 \pm 0.2$ MeV and $L(\rho_0) = 46.0 \pm 4.5$ MeV at $\rho_0 = 0.11$ fm^3, extracted from nuclear mass and the neutron skin thickness of Sn isotopes. Our results indicate that the symmetry energy cannot be stiffer than a linear density dependence.

GEANT4 simulations and commissioning of ALBEGA

Antonio Di Nitto
GSI Darmstadt, Germany

E-mail: a.dinitto@gsi.de

Abstract

The present knowledge of the nuclear structure of superheavy nuclei (SHN) is still scarce, in spite of large efforts devoted to in the last decades [1]. This is mainly due to the low production rate [2]. The most successful method for producing the SHN nuclei is to use heavy-ion induced fusion-evaporation reactions performed with in-flight recoil separators in combination with a detection setup. An improvement of the background conditions was observed applying a chemical isolation system after separator [3]. In order to collect a more complete spectroscopic dataset in such experiments, a next generation detection system ALBEGA (for measurements of Alpha-Beta-Gamma decays after chemical isolation) was recently built at GSI. ALBEGA is dedicated to simultaneous measurements of alpha-particles, electrons, photons and fission fragments. The setup, which comprises of a gas channel, Si detectors and Ge detectors, has recently been commissioned. First experimental data in comparison with simulations, and an outlook on future applications will be present.

REFERENCES

[1] R.-D. Herzberg and P.T. Greenless, Prog. Part. Nucl. Phys. **61**, 674 (2008).
[2] J.H. Hamilton, S. Hofmann and Y.T. Oganessian, Annu. Rev. Nucl. Part. Sci. **63**, 383 (2013).
[3] J. Dvorak et al., Phys. Rev. Lett. **97**, 242501 (2006).

In-medium and isospin effects of strange particles in heavy-ion collisions

Zhaoqing Feng
IMP Lanzhou, China

E-mail: fengzhq@impcas.ac.cn

Abstract

Dynamics of strange particles produced in proton induced nuclear reactions and in heavy-ion collisions near threshold energies has been investigated within the Lanzhou quantum molecular dynamics (LQMD) transport model [1]. The in-medium modifications on particle production in dense nuclear matter are considered through corrections on the elementary cross sections via the effective mass and the mean-field potentials. A repulsive kaon-nucleon potential is implemented in the model through fitting the flow data and inclusive spectra in heavy-ion collisions, which enhances the energetic kaon emission squeezed out in the reaction zone and leads to a variation of the high-momentum spectrum of the K^0/K^+ yields. It is found that the stiffness of nuclear symmetry energy plays a significant role on the isospin ratio with decreasing the incident energy, and a hard symmetry energy has a larger value of the K^0/K^+ ratio in the domain of subthreshold energies. The attractive antikaon nucleon potential enhances the subthreshold K production and also influences the structure of inclusive spectra. The strangeness production is strongly suppressed in proton induced reactions in comparison to heavy-ion collisions. The kaon-nucleon and antikaon-nucleon potentials change the structures of rapidity and transverse momentum distributions, and also the inclusive spectra [2]. The measured data from KaoS collaboration have been well explained with inclusion of the in-medium potentials.

REFERENCES

[1] Z.-Q. Feng, Phys. Rev. C **83**, 067604 (2011); **84**, 024610 (2011); **85**, 014604 (2012); Nucl. Phys. A **878**, 3 (2012); Phys. Lett. B **707**, 83 (2012).
[2] Z.-Q. Feng, Phys. Rev. C **87**, 064605 (2013); Z.Q. Feng, Wen-Jie Xie, Gen-Ming Jin, **90**, 064604 (2014).

Studying shape coexistence at $Z > 82$ with Coulomb excitation at REX-ISOLDE

Liam Gaffney
UWS Paisley, United Kingdom

E-mail: liam.gaffney@uws.ac.uk

Abstract

The region of neutron-deficient nuclei close to $Z = 82$ is well known for its manifestation of shape coexistence, with competition between different spherical, oblate and prolate structures. A large programme of Coulomb-excitation experiments has been undertaken at REX-ISOLDE in order to provide precise and extensive measurements of electromagnetic matrix elements. In particular, low-lying E2 matrix elements hold the key to understanding the shape of, and the mixing between, competing structures in this region. While there are many complementary techniques to study nuclear structure, Coulomb excitation adds substantial information detailing shape-coexistence, such as spectroscopic quadrupole moments, in a model-independent manner. This talk will show results from the afore-mentioned campaign, with a focus on the radon and polonium isotopes. The data has been analysed using the least-squares search code, GOSIA, and will be presented in terms of the quadrupole collective parameters. One approach to the interpretation that will be detailed is that of the two-state-mixing model. This has proved to be a powerful, if not simplified, way of describing the mercury and polonium isotopes. Comparisons to state-of-the-art beyond-mean-field calculations will also be explored.

From the 8π to GRIFFIN – Gamma-ray spectroscopy following beta-decay at TRIUMF-ISAC

Paul Garrett

Department of Physics, University of Guelph, Guelph, Canada

E-mail: pgarrett@physics.uoguelph.ca

Abstract

The 8π spectrometer at TRIUMF-ISAC was the world's premier device for gamma-ray spectroscopy following beta-decay at the TRIUMF-ISAC radioactive beam facility. Its highly successful operation involved measurements of Fermi super-allowed β^+ emitters for fundamental symmetry tests, and a number of nuclear structure studies. While no longer a state-of-the-art device, through development of specialized auxiliary detectors and careful attention to the data acquisition system, it became the world's most sensitive spectrometer for beta-decay studies achieving unmatched precision in gamma-ray half-life measurements, routinely observed beta-decay branches at the parts-per-million level, and individual gamma-ray branches from excited states at the 0.01% level. While the 8π was a world-leading spectrometer, it represented 30-year-old technology in its Ge detectors. In January 2014 it was decommissioned and in September 2014 we commissioned a new device, GRIFFIN, composed of 16 large-volume clover HPGe detectors that represents a gain of more than two orders of magnitude in gamma-gamma coincidence efficiency at 1 MeV. This presentation will focus on highlights from the decade of research with the 8π spectrometer, some early results from GRIFFIN, and future developments.

Opportunities at the Super-FRS separator-spectrometer

Tuomas Grahn
University of Jyväskylä, Finland

E-mail: tuomas.grahn@jyu.fi

Abstract

Superconducting Fragment Separator (Super-FRS) is the central device of the NUSTAR collaboration of FAIR. The separator will provide beams of exotic nuclei ranging from H to U over a large energy range up to 1.5 AGeV. The exotic nuclei are produced via projectile fragmentation, fission and two-step reactions. The nuclides of interest will be separated in flight within several hundreds of nanoseconds. The Super-FRS Collaboration will support the development of Super-FRS. It will use the versatile separator-spectrometer performance of the Super-FRS and in particular high momentum resolution capabilities of the multiple-stage separator-spectrometer. The Scientific programme of the Super-FRS Collaboration is largely unique or complementary with the other experiments of the NUSTAR collaboration. The physics programme exploiting unique properties of Super-FRS, and its basics beam diagnostics instrumentation will be presented.

Isobar Analogue States (IAS), Double Isobar Analog States (DIAS), Configuration States (CS), and Double Configuration States (DCS) in halo nuclei. Halo isomers.

Igor Izosimov
JINR Dubna, Russia

E-mail: izosimov@jinr.ru

Abstract

The IAS of the halo nuclei may have a halolike structure [1]. IAS is the coherent superposition of the excitations like neutron hole-proton particle coupled to form the momentum $J = 0^+$ and has isospin $T = T_z + 1$. CS are not the coherent superposition of such excitations and have $T = T_z$. The DIAS has the isospin $T = T_z + 2$ and is formed as the coherent superposition of the excitations like two neutron hole-two proton particles with $J = 0^+$. For the IAS, CS, DIAS, and DCS the proton particles have the same spin and spatial characteristics as the corresponding neutron holes. For two-neutron halo nucleus (parent state), IAS, DIAS, CS, and DCS can simultaneously have nn, np, and pp halo components in their wave functions [2]. The isomers are able to be formed when excited and ground states have different halo structures (halo isomers). Structure of the excited states in halolike nuclei is discussed. Special attention is given to the nuclei for which ground state does not have a halo structure but excited states may have a halo structure. $B(M\lambda)$ and $B(E\lambda)$ values for γ-transitions in ^{6,7,8}Li, ^{8,9,10}Be, ^{8,10,11}B, ^{10,11,12,13,14}C, ^{13,14,15,16,17}N, ^{15,16,17,19}O, and ^{17}F are analyzed.

REFERENCES

[1] Y. Suzuki and K. Yabana, Phys. Lett. B **272**, 173 (1991).
[2] I.N. Izosimov, Proc. Int. Conf. EXON2012, Vladivostok, Russia, World Scientific, 129 (2013).

Evolution of collective structures in the heavy transitional nuclei above $N = 82$

David Joss
University of Liverpool, United Kingdom

E-mail: David.Joss@liverpool.ac.uk

Abstract

The development of correlated behavior in atomic nuclei, generated by the interactions between their constituent nucleons, is an issue of central importance in nuclear physics. Notably, the evolution of collectivity in nuclei as a function of the nucleon number is reflected in the spectrum of low-lying excited states, which vary according to the available valence space. The longest chains where excited states can be identified span the $82 < N < 126$ neutron shell. The advent of selective tagging techniques has allowed the excited states in many heavy neutron-deficient nuclei above the $N = 82$ shell gap to be measured for the first time. This paper surveys the results of recent experiments that reveal the interplay between collective behaviour and the underlying single-particle configurations in the transitional Ta, W and Re nuclides.

News from ISOLDE and HIE-ISOLDE

Magda Kowalska
CERN Geneva, Switzerland

E-mail: kowalska@cern.ch

Abstract

ISOLDE is the CERN laboratory for research with radioactive ions. Thanks to on-going target and ion source developments and upgrades and additions of new experimental techniques and setups, it has provided for physics close to 1000 isotopes of 70 chemical elements. The first part of the talk will cover the latest technical achievements which allowed providing new, more intense and more pure beams for research. The HIE-ISOLDE project for post-accelerating the radioactive beams and its status will be also briefly presented, as well as the MEDICIS project for producing radionuclides for medical studies. In the second part, new additions to ISOLDE experimental setups will be presented together with physics highlights which were achieved thanks to these upgrades. To these belong new beamlines IDS and VITO and the addition of an electrostatic trap to ISOLTRAP.

High-resolution CRIS and the secrets of ^{206}Fr

Kara Lynch
CERN Geneva, Switzerland

E-mail: kara.marie.lynch@cern.ch

Abstract

The Collinear Resonance Ionization Spectroscopy (CRIS) experiment at the ISOLDE facility, CERN, combines laser spectroscopy and nuclear-decay spectroscopy to provide nuclear-structure measurements of exotic isotopes. At CRIS, the high resolution innate to collinear laser spectroscopy is combined with the high efficiency of ion detection to provide a highly sensitive technique to probe an isotope hyperfine structure. In addition to hyperfine-structure studies, ionization of the isotope of interest allows the (ground state or isomeric) ion beam to be deflected to a decay-spectroscopy station for alpha-decay tagging of the hyperfine components. The first measurements of the neutron-deficient francium isotopes achieved a linewidth of 1.5 GHz, allowing the structure of isotopes down to ^{202}Fr to be studied [1,2]. Recently, high-resolution laser spectroscopy with linewidths as low as 20 MHz have been achieved, without a significant reduction in experimental efficiency [3]. This has allowed the measurements of electric quadrupole moments, in addition to magnetic moments and isotope shifts. Here we report on the latest results from the francium experimental campaign: the achievement of high-resolution laser spectroscopy and the nuclear structure insights this resolution provides in the case of the low-lying states of ^{206}Fr [4].

REFERENCES

[1] K.T. Flanagan et al., Phys. Rev. Lett. **111**, 212501 (2013).
[2] K.M. Lynch et al., Phys. Rev. X **4**, 011055 (2014).
[3] R.P. de Groote et al., Phys. Rev. Lett. **115**, 132501 (2015).
[4] K.M. Lynch et al., Phys. Rev. C **93**, 014319 (2016).

Giant dipole resonances of alpha-clustering nuclei

Yu-Gang Ma
Shanghai Institute of Applied Physics, Chinese Academy of Sciences, Shanghai, China

E-mail: ygma@sinap.ac.cn

Abstract

It is studied how the α cluster degrees of freedom, such as α clustering configurations close to the α decay threshold in ^{12}C and ^{16}O, including the linear chain, triangle, square, kite, and tetrahedron, affect nuclear collective vibrations with a microscopic dynamical approach, which can describe properties of nuclear ground states well across the nuclide chart and reproduce the standard giant dipole resonance (GDR) of ^{16}O quite nicely. It is found that the GDR spectrum is highly fragmented into several apparent peaks due to the α structure. The different α cluster configurations in ^{12}C and ^{16}O have corresponding characteristic spectra of GDR. The number and centroid energies of peaks in the GDR spectra can be reasonably explained by the geometrical and dynamical symmetries of α clustering configurations. Therefore, the GDR can be regarded as a very effective probe to diagnose the different α cluster configurations in light nuclei.

The new permanent decay experiment at ISOLDE: The ISOLDE decay station

Miguel Madurga
CERN Geneva, Switzerland

E-mail: miguel.madurga@cern.ch

Abstract

The ISOLDE Decay Station (IDS) is a newly commissioned permanent experiment at the ISOLDE facility, CERN. It is intended to provide the essential infrastructure needed to perform decay experiments with low energy radioactive beams. The IDS workhorses are 5 HPGe germanium detectors, four 4-leaf clovers and one miniball triple-cluster, providing 5% detection efficiency at 1 MeV. The IDS frame can accommodate different detectors and chambers complementing the germanium detectors, allowing for a variety of experiments to be performed. In this presentation I will show results from the first experimental campaign at the IDS in 2014. Several decay experiments were performed, from fast electronic timing of Indium isomers, to three proton emission in ^{31}Ar. The current 2015 experimental campaign will bring substantially augmented capabilities with the addition of the high efficiency neutron detector VANDLE. This will allow for the first measurement of the neutron emission following the decay of ^{130,132}Cd and ^{53}K isotopes. Future plans, including the construction of an ISOLDE decay neutron detector will be discussed.

Data acquisition, processing and visualization package for multidimensional experimental data in nuclear physics

Vladislav Matoušek

Institute of Physics, Slovak Academy of Sciences, Bratislava, Slovakia

E-mail: Vladislav.Matousek@savba.sk

Abstract

The quality of the analysis of spectrometric data consists in correct identification of the existence of peaks and subsequently in good estimation of their positions, areas and other parameters. In the talk we will present several sophisticated methods for background estimation, deconvolution, peak searching and visualization of multidimensional γ-ray spectra, which are implemented in our data acquisition, processing and visualization system. The presented algorithms include the sophisticated methods for background elimination, for separation of peak containing regions from peak-free regions, deconvolution and identification of information carrier objects.

The deconvolution methods are very efficient and widely used tools to improve the resolution in the spectrometric data. They are of great importance mainly in the tasks connected with decomposition of low amplitude overlapped peaks (multiplets) in the presence of noise. Several visualization techniques suitable for multidimensional experimental data presentation will be presented also.

Experimental study for multi-nucleon transfer induced fission

Katsuhisa Nishio
ASRC JAEA Tokai, Japan

E-mail: nishio.katsuhisa@jaea.go.jp

Abstract

We will present experimental results on multi-nucleon transfer induced fission. The reaction would open access to neutron-rich heavy nuclei for the fission study. We are obtaining data of fission fragment mass distributions for nuclei produced in the reactions in ^{18}O + ^{232}Th, ^{238}U, and ^{248}Cm. The data will be discussed in the framework of fluctuation-dissipation model.

Study of two-proton pairing via the (^{3}He,n) reaction

Paul Papka
University of Stellenbosch, South Africa

E-mail: papka@sun.ac.za

Abstract

High-resolution measurement using (^{3}He,n) reactions is achieved by detecting the γ-ray decay of populated excited states in an array of escape suppressed HPGe detectors in coincidence with fast neutrons. The detection of neutrons at and close to zero degree offers very selective conditions to identify states populated with $L = 0$ relative angular momentum. This is demonstrated with the two-proton stripping to $7/2^-$ 2p-1h levels using the ^{59}Co(^{3}He,nγ)^{61}Cu reaction at $E_{\mathrm{Lab}} = 22.5$ MeV. Discrepancies with large basis shell model calculations indicate a possible wrong treatement of proton pairing in nuclei.

Nuclear matter properties in a density dependent mean-field model with the 2-parametric class of density functions

Kristian Petrík

Institute of Physics, Slovak Academy of Sciences, Bratislava, Slovakia

E-mail: kristian.petrik@savba.sk

Abstract

A density dependent mean-field model of dense nuclear matter, which employs a novel 2-parametric class of density functions, is presented. Since it is an effective model in the Hartree approximation, it is not parameter-free and does not take into account a direct momentum dependence in self-energies. Two distinct mean-field parametrizations have been thus extracted from the microscopic Dirac-Brueckner-Hartree-Fock (DBHF) nucleon-meson vertices. In order to achieve a successful reproduction of the underlying equation of state, momentum corrected data were used. The first parametrization is focused on the best possible description of the DBHF calculations, however, it is well known that DBHF calculations slightly overestimate some saturation properties. Because of this, we prepared the second parametrization that improves the saturation properties of symmetric nuclear matter and at the same time retains a good reproduction of the DBHF data. In this way, we provide a model description of dense nuclear matter with very low number of free parameters that can be used for calculations of properties of finite nuclei and compact stars as well.

New insights on nuclear structure around ^{68}Ni from reaction and decay measurements

Riccardo Raabe
Instituut voor Kern- en Stralingsfysica, KU Leuven, Belgium

E-mail: raabe@kuleuven.be

Abstract

The region around the nucleus ^{68}Ni, with a shell closure at $Z = 28$ and a sub-shell closure at $N = 40$, is the source of considerable interest in nuclear-structure studies. Despite a significant set of experimental and theoretical information available on ^{68}Ni [1–5], the origin of its structure is still being questioned. A recent clarification of the energy and spin assignment of several low-lying 0^+ and 2^+ states [6–9] and state-of-the-art shell model calculations [5,10] hinted to the possibility of triple shape coexistence and highlighted the need of additional experimental investigation. To better understand the structure of ^{68}Ni, two complementary experiments: the two-neutron transfer reactions on ^{66}Ni at 2.85 MeV/u and the beta-decay of ^{68}Co were performed at ISOLDE. On one hand, the ^{66}Ni(t,p)^{68}Ni reaction represents a unique tool to probe the nature of 0^+ states in ^{68}Ni. Coincidences between the outgoing light charged particles and gamma-rays were detected using the combined MINIBALL [11] gamma-ray spectrometer and the T-REX particle detection array [12]. Results of such coincidence analysis together with the reconstruction of angular distributions of the reaction products, revealing the most populated states, will be presented. An interpretation based on calculations within the Distorted-Wave Born Approximation (DWBA) and shell model two-nucleon amplitudes will be discussed. On the other hand, the measurement of the beta-decay of the low spin isomer in ^{68}Co selectively produced in the decay chain of ^{68}Mn allowed us to build a revised decay scheme to ^{68}Ni based on the clear identification of beta-gamma-E0 delayed coincidences. A strong emphasis will be put on the connections between the three lowest lying 0^+ and 2^+ determined from observed transitions and upper limits.

REFERENCES

[1] M. Bernas et al., Phys. Lett. B **113**, 279 (1982).
[2] R. Broda et al., Phys. Rev. Lett. **74**, 868 (1995).
[3] W.F. Mueller et al., Phys. Rev. C **61**, 054308 (2000).
[4] O. Sorlin et al., Phys. Rev. Lett. **88**, 092501 (2002).
[5] S.M. Lenzi et al., Phys. Rev. C **82**, 054301 (2010).
[6] S. Suchyta et al., Phys. Rev. C **89**, 021301(R) (2014).
[7] F. Recchia et al., Phys. Rev. C **88**, 041302(R) (2013).
[8] C.J. Chiara et al., Phys. Rev. C **86**, 041304(R) (2012).
[9] R. Broda et al., Phys. Rev. C **86**, 064312 (2012).
[10] Y. Tsunoda et al., Phys. Rev. C **89**, 031301(R) (2014).
[11] N. Warr et al., Eur. Phys. J. A **49**, 40 (2013).
[12] V. Bildstein et al., Eur. Phys. J. A **48**, 85 (2012).

Charge radii of superheavy nuclei and exotic nuclei from decay data

Zhongzhou Ren
Nanjing University, Nanjing, China

E-mail: zren@nju.edu.cn

Abstract

One of fundamental properties of a nucleus is its radius [1, 2]. Experimental information on nuclear charge radii can be obtained by different sources such as electron scattering, muonic atom spectra, isotope shifts, and so on [2, 3]. These methods are successful for the nuclei near the β-stability line. However, it is difficult for them to obtain charge radii of exotic nuclei and superheavy nuclei, because these nuclei are produced by experiments and exhibit short lifetimes so that they are not available as target nuclei. In view of this, we propose a method to determine nuclear charge radii from the decay data [4–7]. As we all know, α-decay is the main decay mode of heavy and superheavy nuclei [4, 5]. We extract their charge radii from the experimental α-decay data by the aid of the well-established α-decay model [8]. The charge distribution of daughter nuclei is determined in the double-folding model to reproduce the experimental α-decay half-lives. The root-mean-square (rms) charge radius is then calculated using the resulting charge distribution. Nuclear radii of heavy and superheavy nuclei with $Z = 98$–116 are extracted from the α-decay data [6], for which α-decay is an unique tool to probe nuclear sizes at present. This is the first result on nuclear charge radii of superheavy nuclei based on the experimental α-decay data. Moreover, the rms charge radii of some medium-mass proton-rich nuclei and light neutron-rich nuclei are separately extracted from the experimental data of proton emission and cluster radioactivity in a similar manner [7].

REFERENCES

[1] R. Hofstadter, Rev. Mod. Phys. **28**, 214 (1956).
[2] I. Angeli and K.P. Marinova, At. Data Nucl. Data Tables **99**, 69 (2013).
[3] Z. Wang and Z. Ren, Phys. Rev. C **70**, 034303 (2004).
[4] Yu.Ts. Oganessian, J. Phys. G: Nucl. Part. Phys. **34**, R165 (2007).
[5] R.G. Lovas, R.J. Liotta, A. Insolia, K. Varga, and D.S. Delion, Phys. Rep. **294**, 265 (1998).
[6] D. Ni, Z. Ren, T. Dong, and Y. Qian, Phys. Rev. C **87**, 024310 (2013).
[7] Y. Qian, Z. Ren, and D. Ni, Phys. Rev. C **87**, 054323 (2013).
[8] D. Ni and Z. Ren, Phys. Rev. C **80**, 051303(R) (2009); Phys. Rev. C **81**, 024315 (2010).

Tape transport of the decay spectrometer TATRA

Matúš Sedlák
Institute of Physics, Slovak Academy of Sciences, Bratislava, Slovakia

E-mail: sedlak.matt@gmail.com

Abstract

For the purpose of the dedicated program of beta-decay studies of odd-mass Au performed at the CERN-ISOLDE facility, the TATRA tape transportation system was constructed at the Institute of Physics, Slovak Academy of Sciences. In the talk, technical details of the system will be presented. System is using the tape made of rapidly quenched alloy of metals. Rapid quenching causes the amorphous character of the material, that gives excellent mechanical properties to the tape. The tape was welded into endless loop and operated in the mode similar to historical 8-track tapes used for video and sound recording. Only one reel is used, which makes whole system simple and compact. Tape is controlled by single stepper motor located outside of the vacuum chamber and is completely insulated from the rest of the chamber giving the opportunity to employ it as a Faraday cup for beam tuning.

The system was successfully used in August 2014 for the study of ^{181,183,185,187,189}Hg beta decays.

Nuclear physics for astrophysics with old and new methods and facilities

Livius Trache
IFIN-HH Bucharest, Romania

E-mail: livius.trache@nipne.ro

Abstract

There are two main difficulties we encounter in nuclear astrophysics: very low cross sections because "the stars are cold" and the involvement of unstable nuclei in so many reactions in stars. To bypass them we need to use indirect methods and radioactive beams. In this talk I will review some of the indirect methods used in nuclear astrophysics with emphasis on reactions with radioactive nuclear beams: use of reactions at tens or hundreds MeV/nucleon to extract cross sections at tens or hundreds of keV and reaction rates in stellar conditions. I will stop also at examples of using exotic spectroscopy for NA and sketch how new facilities can contribute to the advancement of the field.

Nuclear structure of odd-mass gold isotopes

Martin Venhart
Institute of Physics, Slovak Academy of Sciences, Bratislava, Slovakia

E-mail: mvenhart@cern.ch

Abstract

Odd-Au isotopes show very vividly the effect of nearly degenerate, low-energy shape coexistence. Many coexisting configurations appear at low excitation energy resulting in very complex spectra of gamma rays. In the presentation, results of recent in-beam gamma-ray and beta-decay studies of $^{177-189}$Au isotopes, performed at ISOLDE, University of Jyväskylä and iThemba Labs will discussed. The states associated with the $h_{11/2}$ unique-parity orbital were studied in great detail with important implications on even-Hg cores. The IS521 experiment employed novel Broad Energy germanium detector to detect gamma rays following the beta decay odd-Hg isotopes. Excellent properties, e.g., very good resolution and smooth background suggest this type of detector as the future most promising one for studies of odd-mass isotopes. Spectra obtained with the BE2020 type of detector will be presented.

Self-consistent descriptions of fission barriers in super-heavy nuclei

Michał Warda
UMCS Lublin, Poland

E-mail: warda@kft.umcs.lublin.pl

Abstract

Super-heavy nuclei with $Z > 100$ decay mainly through emission of an alpha particle or spontaneous fission. The life-times in these processes have to be determined to check stability of the heavies isotopes. Alpha decay depends mainly on the difference between ground state masses of parent and daughter nuclei [1]. Stability against spontaneous fission is governed by the size of the fission barrier and inertia parameter along the fission path. The crucial problem is determination of the fission path on the potential energy surface that minimize action integral. In the region of super-heavy nuclei a variety of types of fission paths can be found: reflection-symmetric, reflection-asymmetric, triaxial, one- or two-humped. Results of constraint self-consistent calculations with Gogny HFB model will be presented. Details of calculations with allowed octupole deformation [2] and triaxial shape of a nucleus will be discussed [3].

REFERENCES

[1] M. Warda, J.L. Egido, L.M. Robledo, Int. J. Mod. Phys. E **15**, 504 (2006).
[2] M. Warda, J.L. Egido, Phys. Rev. C **86**, 014322 (2012).
[3] A. Baran, M. Kowal, P.-G. Reinhard, L.M. Robledo, A. Staszczak, M. Warda, Nucl. Phys. A **944**, 442 (2015).

Pattern recognition in nuclear structure

John L. Wood
School of Physics, Georgia Tech, Atlanta, USA

E-mail: jw20@prism.gatech.edu

Abstract

Nuclear structure study relies on recognizing patterns in excited states of nuclei. A simple example is the energy of the first-excited state with spin-parity 2^+ in doubly even nuclei: depending on whether this is low or high, inference is made regarding the presence or absence of a closed shell or of deformation. This is usually done "locally", i.e., relative to neighboring nuclei. A major factor in "discovery" in nuclear structure is sudden changes, especially unexpected, in local patterns of behavior.

Even at the basic level of first-excited 2^+ states, discoveries of interesting structure are being reported; and probable errors are being made because of lack of information on other excited states, the patterns of which would lead to different interpretations. For example, a low-lying excited 0^+ state often results in the "depression", through state mixing, of the 0^+ ground state in a doubly even nucleus, which leads to the appearance of an anomalously high first-excited 2^+ state.

Recent perspectives on pattern recognition in nuclei, pertaining to shell, seniority, collective and shape coexisting structure, will be described. Ideas for theoretical needs and development will be addressed.

Probing nuclear structure with various experimental techniques at Heavy Ion Laboratory in Warsaw

Kasia Wrzosek-Lipska

Heavy Ion Laboratory University of Warsaw, Poland

E-mail: wrzosek@slcj.uw.edu.pl

Abstract

Heavy Ion Laboratory (HIL) in Warsaw, operating a K=160 heavy-ion cyclotron, provides stable beams ranging from ^{10}B to ^{40}Ar with energies from 2 to 10 MeV/u and intensities up to few hundred *e*nA. Research at HIL are pursued within fields like nuclear structure studies and biological or medical applications. One of the extensively used techniques is the gamma spectroscopy. The most important instrument to study nuclear structure at HIL is the EAGLE array which has been designed as a multi-configuration detector set-up for in-beam nuclear spectroscopy measurements. The array can accommodate up to 30 Compton suppressed HPGe detectors coupled with various ancillary devices such as conversion-electron spectrometer, the Koeln-Bucharest plunger, an array of PIN diode detectors, 4π inner ball consisting of 60 BaF_2 crystals and an array of 4π epitaxial silicon detectors. This versatility allows to perform a detailed and comprehensive measurements of electromagnetic transitions and moments involving a wide spectrum of experimental probes. Selected results obtained with various experimental techniques will be presented. This includes Coulomb excitation, lifetime measurements, the gamma-gamma and conversion-electron spectroscopy. The role of small-scale facilities in providing complementary and essential data for the exotic nuclei studies will be shown.

Spin dynamics in intermediate-energy heavy-ion collisions

Jun Xu
SINAP Shanghai, China

E-mail: xujun@sinap.ac.cn

Abstract

We have introduced the nuclear spin-orbit coupling to the isospin-dependent Boltzmann-Uehling-Uhlenbeck transport model for intermediate-energy heavy-ion collisions. Similar to the spin hall effect, we found that the spin-orbit coupling can lead to the splitting of collective flows for spin-up and spin-down nucleons. The detailed properties of the spin-orbit coupling such as its strength, density dependence, and isospin dependence can be studied via spin-related observables in intermediate-energy heavy-ion collisions. We have also improved the coalescence algorithm for cluster formation by explicitly including spin degree of freedom. Further studies of introducing tensor force as well as other interesting spin-related phenomena will be discussed.

Deformation of neutron-rich nuclei around ^{100}Zr studied using Coulomb excitation and lifetime

Magda Zielińska
CEA Saclay, France

E-mail: magda.zielinska@cea.fr

Abstract

The well-known sudden onset of deformation in neutron-rich Zr and Sr isotopes at $N = 60$ results from crossing of structures of different deformation that are observed to coexist at low excitation energy for $N = 58$ and $N = 60$ nuclei in this mass region. I will discuss recent results from Coulomb excitation experiments performed at the ISOLDE facility concerning the collectivity of ^{96}Sr, coexistence of well deformed and weakly deformed configurations in ^{98}Sr, as well as the first observation of rotational bands in ^{97,99}Rb. I will also present some results of the experiment performed at GANIL in 2011 in order to measure picosecond lifetimes in $A \sim 100$ nuclei populated in a fusion-fission reaction.

ISBN 978-80-971975-1-3